



UNIVERSITY OF
BIRMINGHAM

AUTOMATIC TARGET DETECTION AND SPEED ESTIMATION USING
FORWARD SCATTER RADAR SENSOR

By

Xu Chunyang

A thesis submitted to School of Electronic, Electrical and Computer Engineering of
the University of Birmingham

for the degree of

DOCTOR OF PHILOSOPHY

2015

UNIVERSITY OF
BIRMINGHAM

University of Birmingham Research Archive

e-theses repository

This unpublished thesis/dissertation is copyright of the author and/or third parties. The intellectual property rights of the author or third parties in respect of this work are as defined by The Copyright Designs and Patents Act 1988 or as modified by any successor legislation.

Any use made of information contained in this thesis/dissertation must be in accordance with that legislation and must be properly acknowledged. Further distribution or reproduction in any format is prohibited without the permission of the copyright holder.

To my parents

Abstract

Forward Scatter Radar (FSR) is a subclass of the bistatic radar, where the received target signal occurs mainly due to the direct path signal shadowing by the target body. Employing a separate deployed transmitter and receiver at considerable distance, the FSR can achieve a number of advantages, such as enhanced radar cross section, inherent detection ability of stealth target, reasonably low complexity design of system, more than the conventional monostatic radar. All of these features are attractive to the modern remote sensing systems.

This thesis presents the research results of the detection and speed estimation of the ground target in FSR, which is a vital procedure for automatic targets classification. The hardware was designed and assembled by the Microwave Integrated Systems Laboratory (MISL), University of Birmingham. The experimental data used in this thesis have been collected from real field environments at multiple locations and from various targets. The complex automatic target detection and speed estimation algorithm were integrated to achieve higher accuracy.

The main problem investigated in this research and the appropriate results are dedicated to automatic target speed estimation in complex FSR operational scenario. The improved and originally proposed algorithms are discussed and shown throughout the chapters in great detail. The measurements are implemented in large load of work and the database is created for the validation of these algorithms.

Acknowledgements

First of all, I would like to present my grateful thanks to my supervisors, Prof. Mike Cherniakov and Dr. Peter Jančovič who kindly provided me not only guidance on the research methodology, but also taught me how to be a good researcher.

Secondly, I would also like to thank all of my colleagues; Dr. Vladimir Sizov, Dr. Emileen Rashid, Dr. Zeng Zhangfan, Dr. Zuo Rui, Dr. Liu Feifeng, Dr. Zhang Qilei, Dr. Zhou Hong, Alan Yates, Liam Daniel, Nor Ayu and Kalin, for their kind help and constructive suggestions.

Finally, I would like to give my greatest gratitude to my family, my mother Liu Cuifeng, my father Xu Fuying, my wife Qin Beibei and my son Xu Yisen, who have always supported me.

Table of Contents

Chapter 1	Introduction	1
1.1	Monostatic radar	1
1.2	Bistatic radar	2
1.3	Forward scatter radar	7
1.4	Problem statement and contribution	10
1.5	Thesis outline	11
Chapter 2	Forward scatter radar overview	13
2.1	Introduction.....	13
2.2	Forward Scatter Radar Layout	13
2.3	Bistatic range	14
2.4	Radar Cross Section.....	16
2.5	Specific ground targets RCS analysis	19
2.6	Target signature in FSR	25
2.7	Conclusion	29
Chapter 3	Ground FSRsystem.....	30
3.1	Introduction.....	30
3.2	Ground FSR system topology and vehicle target	30
3.3	GFSR hardware description.....	31
3.3.1	Operating Frequency and Power budget	32
3.3.2	Transmitter.....	34
3.3.3	Receiver	36

3.3.4	Antenna.....	38
3.4	GFSR software description	41
3.4.1	Data structure.....	42
3.5	Conclusion	43
Chapter 4	Automatic target detection.....	44
4.1	Introduction.....	44
4.2	Automatic target detection	45
4.2.1	Modelling signature	53
4.2.2	Coherent detection	61
4.2.3	Non-coherent detection.....	69
4.2.4	Investigation on LPF1's cut off frequency.....	72
4.3	Short-time Fourier transform of the recorded target signature	74
4.4	Mathematical approach to Principal Component Analysis.....	79
4.5	Conclusion	80
Chapter 5	Experimental evaluation and test result.....	82
5.1	GFSR experiment description.....	82
5.2	Tilesford airfield trail	83
5.2.1	Location effect.....	83
5.2.2	Target shape effect.....	86
5.2.3	Multiple speed effect	90
5.3	Senneleys Park trial.....	92

5.4	Pritchatts car park trial	98
5.5	Conclusion	102
Chapter 6	Speed estimation for the ground vehicle target	103
6.1	Introduction.....	103
6.2	Target signal pre-processing	103
6.2.1	Signal processing diagram.....	104
6.2.2	Demonstration of the signal pre-processing procedure	106
6.3	Conventional SE algorithm.....	112
6.4	Speed normalization using modelling signal	115
6.5	Improvement of the SE algorithm.....	117
6.5.1	Multiple 90 degree phase shift reference functions.....	117
6.5.2	Experimental evaluation of the improved SE algorithm	120
6.6	Empirical Improvement to the SE algorithm	122
6.6.1	Introduction to the slope algorithm	122
6.6.2	Fusion algorithm of slope and amplitude of cross correlation	129
6.6.3	Pritchatts car park database evaluation.....	133
6.7	Conclusion	136
Chapter 7	Summaries and future work.....	138
7.1	Summaries.....	138
7.2	Future work.....	139
Chapter 8	Reference	141

Chapter 9	Appendix	146
	Appendix A RCS simulation result.....	146
	Appendix B Some result of STFT	148
	Appendix C Speed normalization result	152
	Appendix D Sample Matlab code	157
	Appendix E Publications.....	169

List of figures	
Figure 1.1 Monostatic radar block diagram	2
Figure 1.2 Bistatic radar configuration	3
Figure 1.3 The Bistatic radar coordinate system in three dimensions	4
Figure 1.4 British Chain Home and German Klein Heidelberg bistatic radar locations (image captured from Google Map)	5
Figure 1.5 The DEW line.....	6
Figure 1.6 FSR configuration	8
Figure 2.1 3D coordinating system for the FSR	14
Figure 2.2 Cassini ellipse for bistatic radar with SNR index.....	15
Figure 2.3 The Babinet's model for forward scatter radar at $\beta = 180^\circ$	17
Figure 2.4 Shadowing field effect.....	17
Figure 2.5 The Normalized backscattered RCS of a sphere in semi-log scale	19
Figure 2.7 Modelling target of ground vehicle in perspective view	21
Figure 2.8 Plane wave illumination from the right hand side of the vehicle at 434MHz..	22
Figure 2.9 The 3D RCS of the vehicle target.....	23
Figure 2.10 RCS farfield as a function of theta for 434MHz	23
Figure 2.11 Bistatic scatter RCS comparison in multi frequencies (a) Simulation FS CS for the multi frequency (b) The zoomed in details	25
Figure 2.13 Bistatic doppler geomery.....	27
Figure 3.1 Ground FSR sensor topology	31
Figure 3.3 Receivers detection range.....	33
Figure 3.4 Transmitter block diagram	34
Figure 3.5 The RadioMetrix (RM) transmitter inner block diagram	35
Figure 3.6 Transmitter with antennas	36

Figure 3.7 The receiver block diagram	36
Figure 3.8 Receiver without antennas.....	37
Figure 3.9 Mutual orientation of Tx and Rx devices	38
Figure 3.10 (a) The helical antenna surface current distribution (b) The radiation intensity distribution of the helical antenna	39
Figure 3.11 The radiation pattern of the centre fed 10 turn normal mode helical antenna at 64MHz	39
Figure 3.13 Antenna (a) Omni directional helical (b) 9dB Directional Yagi	41
Figure 4.1 Envelope of the radar signal and threshold	46
Figure 4.2 Gaussian PDF	48
Figure 4.3 Signal Processing block diagram (a) Ideal coherent detector with matched filter (MF) (b) Non-coherent detector	49
Figure 4.4 Additive White Gaussian noise $N(t)$	49
Figure 4.5 The PSD of the white Gaussian noise	50
Figure 4.6 Comparison of the modelling and analytical result	51
Figure 4.7 The P_D versus SNR	52
Figure 4.8 Comparison of the P_d vs SNR at $P_{fa}=10^{-3}$	53
Figure 4.9 Input modelling signal $U(t)$ -truncated sine waveform (a) Total signal truncated signal: $U(t)$ (b) Time period from 120 to 130 seconds	54
Figure 4.10 Power Spectral Density (PSD) of modelling signal (a) Total frequency range to 2Hz (b) Magnification of main lobe	55
Figure 4.11 Output of first low pass filter - S_1	56
Figure 4.12 Signal wave form received from the RX	57
Figure 4.13 Truncated target signature	57
Figure 4.14 Modelling signature with target signal and white Gauss noise	58

Figure 4.15 PSD of the modelling signature(a) PSD within full frequency range	
(b) Magnification in details.....	59
Figure 4.16 The frequency response of the first LPF with cut off frequency 2Hz (a) Full frequency range (b) Magnification in details within 2Hz.....	60
Figure 4.18 Rectangular shape cosine reference function	63
Figure 4.19 The output of the matched filter	63
Figure 4.20 The output of Hilbert Transform	64
Figure 4.21 The relationship between the P_{fa} and threshold (a) Full range of threshold to 470.....	65
Figure 4.22 The relationship between the P_d and SNR(dB) at $P_{fa}=10^{-3}$	66
Figure 4.23 Reference signal for recorded signal	66
Figure 4.24 The output of the matched filter S2.....	67
Figure 4.25 The output of Hilbert Transform S3.....	67
Figure 4.26 The P_{fa} versus threshold K level.....	68
Figure 4.27 The relationship between the P_d and SNR at $P_{fa}=10^{-3}$	68
Figure 4.28 The comparison of P_d versus SNR for the modelling signal and recorded signal.....	69
Figure 4.29 Wave form of S_3	70
Figure 4.30 The relationship between the P_{fa} and Threshold	70
Figure 4.31 The relationship between the P_{fa} and SNR at $P_{fa}=10^{-3}$	71
Figure 4.32 Comparison of coherent and non-coherent detection for the modelling and recorded signal.....	71
Figure 4.33 The output of the LPF2 after passing through the filter banks.....	72
Figure 4.34 The relationship between the P_{fa} and threshold at varies LPF1	73
Figure 4.35 Relationship between the P_d and SNR at $P_{fa}=10^{-3}$	73

Figure 4.36 The relationship between the P_{fa} and LPF1's cut off frequency at different SNR.....	74
Figure 4.38 DFT segments overlapping (a) without overlap (b) With R-L overlap.....	76
Figure 4.39 Rectangular window added in the recorded signal	76
Figure 4.40 STFT of the recorded signal	77
Figure 4.41 After setting the threshold power equal to -10dB	77
Figure 4.42 The time domain signature with low SNR	78
Figure 5.1 Tilesford airfield experiment description	84
Figure 5.2 Tileford field trial with Tx/Rx deployment (a) First three positions 1-3 on concrete (b) Another three positions (4-6) are on the grass.....	84
Figure 5.3 PSD signatures for the 64MHz frequency channel after speed normalization	85
Figure 5.4 PSD signatures for 434MHz frequency channel after speed normalization...	86
Figure 5.5 (a) GFSR deployment view along the baseline (b) Ground target Landrover passing through baseline (c) Ground target Ford Fiesta passing through baseline.....	88
Figure 5.6 PSD signatures comparison for two targets, Land rover and ford fiesta.....	90
Figure 5.7 PSD signatures comparison for three different velocities using 434MHz directional antenna	91
Figure 5.8 PSD signatures for 434MHz at multi speed in the same position (Tilesford airfield).....	91
Figure 5.9 Top view of the Senneleys Park trial.....	93
Figure 5.10 SenneleysPark trial top view on google map	93
Figure 5.11 SenneleysPark trial at position 2	94
Figure 5.12 PSD plot of the 64MHz Doppler channel at 3 positions after speed normalization	95

Figure 5.13 PSD of the 135MHz Doppler channel in 3 positions after speed normalization	96
Figure 5.14 PSD of the 173MHz Doppler channel in 3 positions after speed normalization	96
Figure 5.15 PSD of the 434MHz Doppler channel in 3 positions after speed normalization	97
Figure 5.16 PCA plot (a) two principal components (b) three principal components	98
Figure 5.17 Top view of Pritchatts car park test site	99
Figure 5.18 (a) position 1 (b)position 2 (c)position3	100
Figure 5.19 PSD for the 64MHz frequency channel.....	100
Figure 5.20 PSD for the 434MHz frequency channel (separate into two plots po1(spe1-4) and sp3(po1-3)).....	101
Figure 6.1 Signal processing block diagram.....	104
Figure 6.2 Signal pre-processing block diagram	107
Figure 6.3 Raw RSSI 144MHz time domain signature S1	108
Figure 6.4 Time domain signature of S2	110
Figure 6.5 Truncated target signature S3.....	110
Figure 6.6 Comparison of the signature with and without truncation (a)Time domain signature of signal S1 and target S3(b)Spectrum of the S1 and S3	111
Figure 6.8SE RMSE results for Tilesford airfield by using cosine wave reference function	114
Figure 6.9 Time domain signatures of modelling target signal	115
Figure 6.10 PSD of the time domain target signatures	116
Figure 6.11 PSD of target after speed normalization.....	116

Figure 6.13 Comparison of signatures for all the frequency channels at Tilesford airfield	118
Figure 6.14 Time domain signal comparison of three frequencies.....	118
Figure 6.15 173MHz (a) recorded signature and (b) reference function	119
Figure 6.16 151MHz(a) recorded signature and (b) reference function	120
Figure 6.17 Max of Xcorr versus speed.....	120
Figure 6.18 Least RMSE chart for varies frequencies	122
Figure 6.19 Simulated target signal using -sine function at 10m/s.....	123
Figure 6.20 Max of XCORR versus speed for the four reference functions	123
Figure 6.21 Simulated target signature and the Max of XCORR versus speed(a) Simulated target signal with 10m/s(red) and 11m/s(blue) in 50%:50% combination(b) XCORR versus speed of signature of (c) Simulated target signal with 10m/s(red) and 11m/s(blue) in 45%:55% combination(d) XCORR versus speed.....	124
Figure 6.22 The speed versus the time scale in simulation.....	125
Figure 6.23 Time domain simulated signature	125
Figure 6.24 Max of XCORR versus speed	126
Figure 6.25 Algorithm for SE using max of cross correlation versus speed	126
Figure 6.26 Upward slope calculation (a) Normal slope calculation (b) Upward region is less than the range (c) Without upward slope	127
Figure 6.27 Slope calculation procedure	127
Figure 6.28 Multi peak detection levels.....	129
Figure 6.29 PSD plot after speed normalization 434MHz channel (a) Max of cross correlation (b) Max of slope (c) Max of slope and then cross correlation.....	132
Figure 6.30 The optimum speed normalization result using 0.6 factor (a) 64MHz (b) 135MHz (c) 434MHz.....	136

Figure 9.1 Bistatic scatter RCS in 173MHz.....	146
Figure 9.2 Bistatic scatter RCS in 151MHz.....	147
Figure 9.3 Bistatic scatter RCS in 144MHz.....	147
Figure 9.4 Bistatic scatter RCS in 135MHz.....	148
Figure 9.5 Bistatic scatter RCS in 64MHz.....	148
Figure 9.6STFTsignature 434MHz.....	149
Figure 9.7 Time domain signature 434MHz.....	149
Figure 9.8 STFTsignature 434MHz.....	150
Figure 9.9 Time domain signature 434MHz.....	150
Figure 9.10 STFTsignature 434MHz.....	151
Figure 9.11 Time domain signature 434MHz.....	151
Figure 9.12 Signal processing for 11.bin 434MHz (a) Time domain signature (b) Truncated Time domain signal 11.bin 434MHz (c) Max of XCORR versus velocity (d)Max of XCORR versus velocity	154
Figure 9.13 Signal processing for 12.bin (a) Time domain signature (b) Truncated Time domain signal (c)Max of XCORR versus velocity (d) Max of XCORR versus velocity.....	155

List of tables

Table 2.1 RCS of the Simple objects which has larger dimension than the wave form..	18
Table 2.2 Landrover model component properties in CST Model	20
Table 3.1 The GFSR operational frequencies.....	32
Table 3.2Attenuators (att) used in the experiments	34
Table 3.3 Yagi antenna electrical specifications.....	40
Table 6.4 Frequency ratio comparison.....	119

Table 6.5 Comparison of RMSE between using the single cosine and maximum multiple reference functions.....	121
Table 6.6 Optimum reference functions portions in each frequency channels based on the least RMSE result.....	121
Table 6.9 SE RMSE values across the criteria and frequencies	130
Table 6.10 Tilesford airfield SE RMSE values	133
Table 6.11 PSD speed normalization result for Pritchatts car park	134
Table 6.12 SE RMSE values.....	134
Table 6.13 Pritchatts car park SE RMSE values.....	135
Table 9.1 Comparison of speed normalization result in frequency domain for the Tilesford airfield	152
Table 9.2 Speed estimation for PritchattsPritchattspark 434MHz.....	153
Table 9.4 Speed estimation result with the parameters factor A	155
Table 9.5 Maximum of cross correlation result with the parameters factor B	156
Table 9.6 Speed estimation result with the parameters factor B.....	156

Glossary of Abbreviations

3D	3 Dimension
AC	Alternation Current
ADC	Analogue to Digital Converter
ANN	Artificial Neural Networks
ATD	Automatic Target Detection
BR	Bistatic Radar
CFAR	Constant False Alarm Rate
CPU	Centre Processing Unit
CW	Continuous Wave
FA	False Alarm
FSR	Forward Scatter Radar
GFSR	Ground Forward Scatter Radar
K-NN	K-Nearest Neighbours
LPF	Low Pass Filter
PEC	Perfect Electric Conductor
PSD	Power Spectrum of Density
PCA	Principle Component Analysis

PDF	Probability Density Function
P_d	Probability of Detection
P_{fa}	Probability of false alarm
RADAR	Radio Detection and Ranging
RAM	Radar Absorb Materials
RCS	Radar Cross Section
RMS	Root Mean Square
RSSI	Received Signal Strength Indicator
SE	Speed Estimation
SNR	Signal-to-Noise Ratio
STD	Standard Deviation
STFT	Short-Time Wavelet Transform
SYN	Synchronization
TRP	Two Ray Path
VHF	Very High Frequency
XCORR	Cross Correlation

Chapter 1 Introduction

1.1 *Monostatic radar*

RADAR, Radio Detection and Ranging in abbreviation form, is the system, which applies the electromagnetic waves to estimate or predict the target motion of interest[1]. The targets include vehicle, land; airplane, atmosphere[2]; ships, sea surface; satellite, minor planet and so on. The information could be extracted from the feature of the reflected signals. Since the first invention of the radar system in the 1930s, the application has been developed in many remote sensing tasks, using the frequency ranges from 50MHz to 100GHz[1].

In general, the radar system is specified in the terms of monostatic radar whose transmitter and receiver are collocated. Figure 1.1 illustrates the principle of the monostatic radar system[3]. First, the radar signal, which is a short train of pulses, is generated by the wave generator and amplified by the power amplifier. Then the duplexer, which is the high-power rapid switch, can direct the signal to the antenna and radiates toward the detection space. Once there is a target present in the space, the signal is scattered back following the direction of transmission. The duplexer permits the reflection signal to go through the Rx amplifier. It should be stressed that the antenna is shared by the transmitter and receiver, at all times. In the Rx blocks, the echo signal is amplified and filtered by the hardware and software processing units, which is embedded in the system. In order to extract the desirable target information, the target detector and digital signal processor is employed. Finally, the information is fed back to the display and commander centre. This is the typical full operational link of the monostatic radar system. The monostatic scheme is widely used in many systems, such as warship, airborne and surveillance radar.

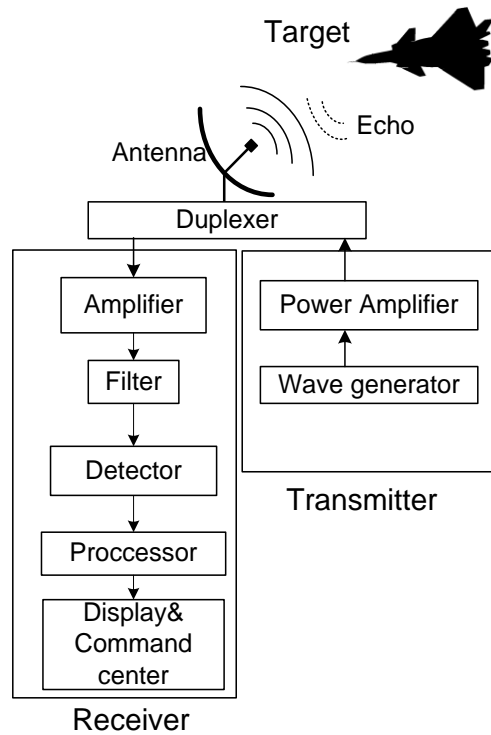


Figure 1.1 Monostatic radar block diagram

1.2 *Bistatic radar*

The first ever radar system was bistatic. The reason for that is before the invention of the duplexer, the transmitter and receiver were equipped with their own antennas to protect them from damage when the transmitter was generating a high power signal. The term 'bistatic radar' is used to distinguish it from the monostatic radar. Figure 1.2 illustrates the configuration of bistatic radar, which has deployment of wide separated transmitter and receiver which is comparable with the range to the target. The three objects, Tx, Rx and Target form the bistatic configuration[4]. And the angle β between line of target-receiver and target-transmitter is called the bistatic angle, which is from 0° to 180° . When the bistatic angle approaches 0 degrees, it is termed to be backscatter radar, while the angle moves towards 180 degrees; it is a forward scatter radar.

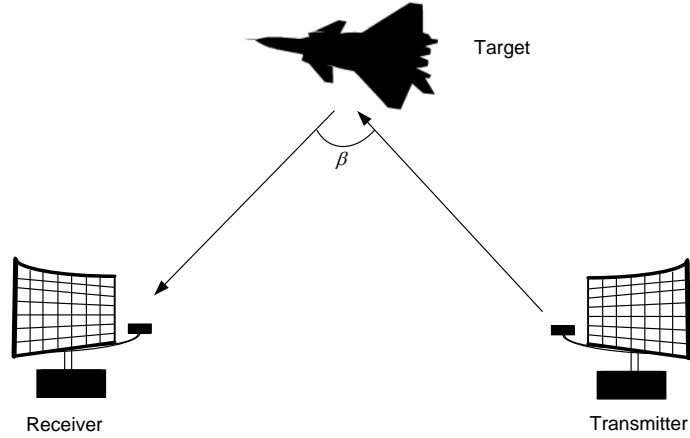


Figure 1.2 Bistatic radar configuration

Figure 1.3 illustrates the three dimension coordinate system of the bistatic radar[4]. The Tx, Rx and Target are organizing the bistatic detection plane. The range between Tx and Rx is defined as the baseline L . The range from target to Tx and Rx are R_T and R_R . The summation of R_T and R_R is calculated as the range summation and it is the contour of constant range value when the target moves within the ellipse. Assuming the parameters R_T , L and the angle θ_T are given, the R_R can be calculated by the triangular equation (1.1):

$$R_R^2 = R_T^2 + L^2 - 2R_T L \cos\left(\frac{\pi}{2} - \theta_T\right) \quad (1.1)$$

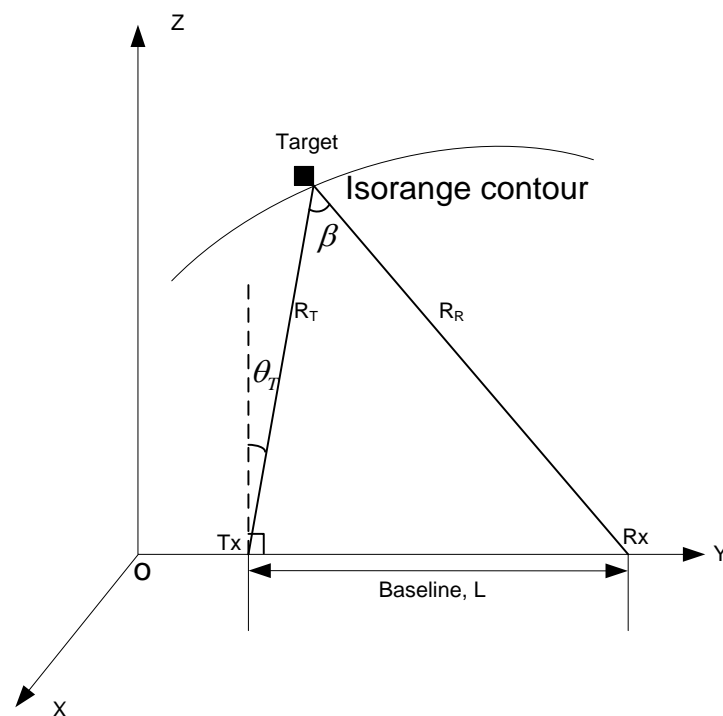


Figure 1.3 The Bistatic radar coordinate system in three dimensions

Many early radar systems utilized the bistatic radar configuration, and these projects are conducted simultaneously in the UK, Germany, US, Soviet Union, France and Japan. The initial systems are listed in Table 1.1[5]. These applications were fast developed between the 1930s and 1950s because of the demands of World War II (WWII).

Table 1.1 Bistatic radar systems

Time	Country	System	Frequency
1930s	United Kingdom	Chain Home (CH)	22-50MHz
1940s	Germany	Klein Heidelberg	120-130MHz
1960s	United States/Canada	DEW	475-525MHz
1930	Soviet Union	RUS-1,2	63MHz
1935	France	Electromagnetic barrier	75MHz
1940	Japan	Type-A /Type-B	40-80MHz

The Chain Home (UK, 1930) was the first practical bistatic radar system located at Bawdsey Manor, England, where the air defense exercise was conducted. At that time, the bistatic scatter fences were mainly applied for earlier aircraft alarming. The radio frequency applied in CH between 22 and 50MHz, the isolation antenna arrays are employed. The peak power of the transmission signal reaches 750kW[6]. Klein Heidelberg (KH) is the German WWII bistatic radar system designed to counter the CH[7]. The earlier KH receiver detected the Chain home transmitter signal and intercepted the receiver of CH[8]. It was not until the late 1990s that the information of KH was revealed by WWII British intelligence reports, stating six sites were deployed during WWII, along the coasts of the Netherlands, Belgium and France. They had a detection range from 300km to 400km[9].

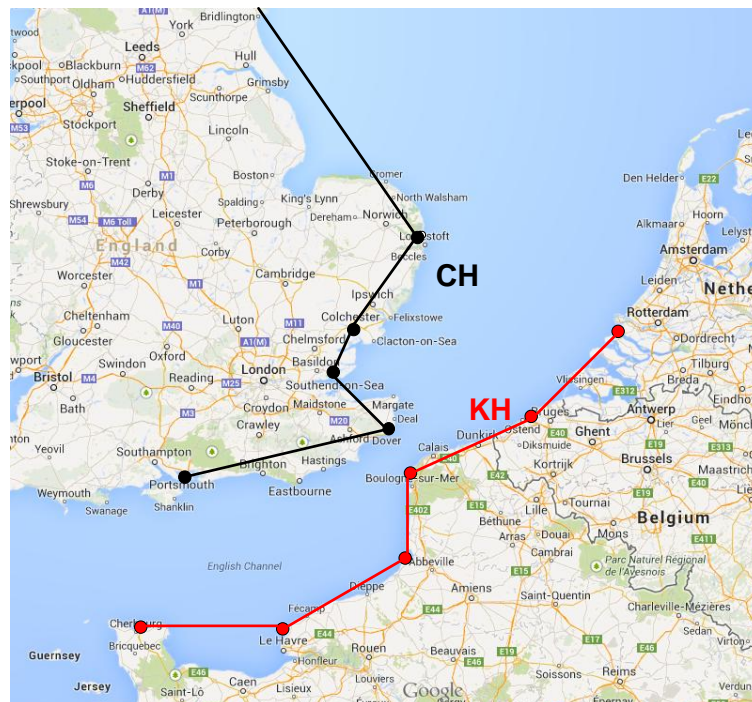


Figure 1.4 British Chain Home and German Klein Heidelberg bistatic radar locations (image captured from Google Map)

The AN/FPS-23 (US, 1960) is the most typical bistatic radar system deployed along the Distant Early Warning (DEW) line in the north Canada board and Alaska islands shown in

Figure 1.5[10]. During the Cold War, the DEW aimed to detect the missile and boomers flying across the arctic region. It was manufactured by Motorola. The operating frequency is from 475MHz to 525MHz. The transmitter utilized the AN/FPT-4 Fluttar which can generate 1kw output power signal and the receiver is using the AN/FPR-2 Fluttar[11]. The waveform is a continuous wave (CW) with the baseline length 50 miles. There were fifty seven radar stations comprised the whole DEW line system. Some of the radar stations are assigned as the main site, while the remainder sites are at the auxiliary stations. The automatic detection with audible alert signals was first proposed for less labour involving purpose. The Doppler effect could be detected by the system when the airplane or missile crossing the detection area[12]. The Mid-Canada Line or McGill Fence developed by the Canadians is also deployed[13].



Figure 1.5 The DEW line

Many other countries, Soviet Union(RUS-1,2)[14], France(Electromagnetic barrier)and Japan(Type-A /Type-B)[15] has also built their own bistatic radar systems for the border security reasons. Most of the systems were adapting the Continuous-Wave (CW) waveforms and separate location of Tx and Rx. The priority detection target is to predict the presence of aircraft, which is a major and emerging threat at that age. Although these systems were subsequently eliminated by the pulse monostatic radar in the later decades, the research interests on bistatic radar were still carried on. Recently, the broadcast and communications

signals have been used as the source of 'illuminators of opportunity' for passive coherent location system. In[16], it is investigated the feasibility study and practical experiment of utilizing the satellite as the Tx while the Rx is located on the ground. The bistatic SAR system can be applied in the moving target indication system. The TV[17] mobile signal[18] and FM radio[19]can also be employed as the source of Tx.

There is another type of radar configuration called the multi-static radar, which has more than one Rx and Tx. It is always referred to the netted sensors which is a combination system of monostatic and bistatic radar. The multi-static radar utilization for the target tracking can be found in[20]. In the communication systems, the Multiple Input Multiple Output (MIMO) also employs multi-static configuration. However, discussing this type of radar system is out of the scope of this thesis range and therefore could be considered as a further research topic.

1.3 Forward scatter radar

Historically, the FSR is the first type of bistatic radar(BR) [5]. It is one of the subclasses of the BR when the target is within the forward scatter radar region[21]. Instead of building the transmitter system themselves, some of the radar systems utilize the broadcasting signals as 'illuminators of opportunity' such as radio or TV signals[22].

The research interests were raised after the urgent need for the detection of the stealth target. The stealth targets are designed to be concealed from the conventional monostatic radar coverage and make themselves less observable. Furthermore, the technologies include reshaping the body to reduce the reflection of radar signal and waveform absorbent material coating. Compared to the monostatic radar, the bistatic radar - especially the forward scatter radar - can offer considerable advantages in regards to the higher probability of detection of the stealth target.

In the bistatic radar scheme, there is an important branch called Forward Scatter Radar (FSR), which is designed to detect and estimate the target motion parameters in the Forward Scattering (FS) region. The region is stretched along the connection line (Baseline) between the Tx and Rx, while the bistatic angle β is approaching 180 degrees. The FSR configuration is shown in Figure 1.6. The targets can be the low-altitude penetration helicopter or the ground vehicle, which has the dramatic reduced RCS feature to the traditional monostatic radar system[23]. Nevertheless, the FSR can fill the gap of the RCS enhancement requirement[24]. Also in[25], more than 15dB enhancement on RCS larger than the monostatic backscatter radar was found. One of the major differences of the monostatic radar is that the reception signature is formed from the interference of the direct signal and the reflection signal from target before it cross the baseline. The monostatic radar's receiver can only get the back scatter waveforms when the target is observed.

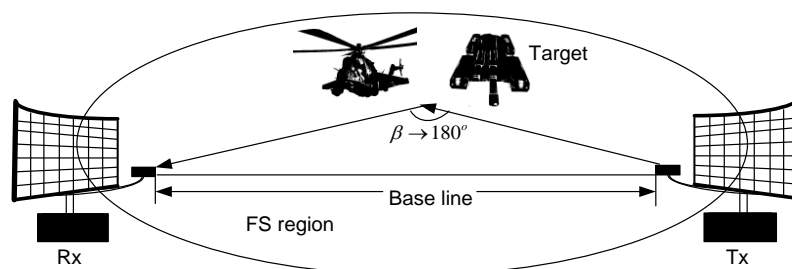


Figure 1.6 FSR configuration

At the beginning of the FSR research, the phenomenon of forward scatter was first explained using the optics theory[26], and from the optical perspective, the Mie region theory was utilized in the initial stage of the research. Then it was quantitatively evaluated for particles as well as the propagation theory in[26]. The rationale and architecture for FSR system was outlined in [22]. It was found that the FSR could be used as an effective tool for the detection of 'very low RCS' targets which were hard to detect. The modelling and FSR radar performance for the jet target were discussed. The target detection and tracking

algorithm were developed to adapt the unmanned situations. In addition, as a special case of bistatic radar operation, the basic bistatic and FSR system was explained in a systematic way, which covers the geometric topics of the system[24].

In the field of anti stealth technology, Ufimtsev [25] investigated the limitation in the stealth technology and concluded that the FSR could overcome the shortage of traditional monostatic radar. Target designs have been altered because the stealth technology utilized the radar cross section reduction methods on aircraft, ships and vehicles. Not only are the shapes of the objects designed in the orthogonal metal plates, F-117 US for instance, but also the Radar Absorb Materials (RAM) coatings are applied to the surface of the body to reduce the reflection of the electromagnetic waves. The monostatic radar can't detect very low or none echo signal strength from the stealth target. However, the FSR configuration can productively and effectively detect the above targets[27].

In recent years, the interest on FSR has been growing for the reason of border security requirement arising and the demand to detect the stealth targets (low size, low speed, etc.)[4].The majority of recently published papers on FSR for surface targets detection are associated with MISL at the University of Birmingham which has implemented a lot of theoretical and experimental research on FSR. In the initial stage, Prof Cherniakov introduced the ground target detection using FSR in[28]. The power budget was analyzed for the potential frequency channels[29], and the propagation loss was also considered in the free-space with Two Ray Path(TRP) model using the Very High Frequency(VHF). It is shown that the TRP model works well in the ground based FSR system.

When the group of targets are taken into consideration, a study on detection of the convey targets was investigated in [30]. The experiments were carried out in the condition involving a car and a human target, and the classification result shows that it can effectively

distinguish the multiple targets. Also, many research have applied the FSR system on the maritime surveillance to detect the sea target, such as ships or power boats[31]. The UWB technology was studied from theoretical and experimental angles [32]. The FSR detection in time and frequency domain on the marine targets can be found in [33]–[38] and the Constant False Alarm Rate(CFAR) detector was applied in the threshold estimation algorithm.

1.4 Problem statement and contribution

This thesis is dedicated to solving the problem for ground target detection and the speed estimation using the Ground FSR system. Investigations on the FSR system for the target detection and classification have been carried out[39], [40].It was shown that the proper speed estimation result will increase the recognition accuracy.

The latest speed estimation and normalization result have been studied at the open airfield environment, which is shown in [41]. It shows the speed normalization result after the speed is properly estimated. The test environment is an ideal case without the reflection objects nearby. Nevertheless, the main challenge of the detection and speed estimation in real systems is that the ground surface is a complex environment with typical surrounding objects and vegetation. Therefore, reception signals are a mixture of target signals with clutter and background noises.

The main contributions of this thesis are specified into the following facts:

First: The analysis of the FSR system in presence of clutter and complex environment has been provided. The estimation study has been conducted under the careful research modelling level.

Secondly: To prove the success of the system modelling, the large load of experiments were taken in the real world environment and the parameters of the surrounding and equipment were recorded for the further processing.

Thirdly: The Monte Carlo simulation result of the probability of detection figure for the modelling and real recorded signal were compared. Also, the possibility of using time-frequency analysis for target detection was proposed with real recorded target signal.

Finally and the most innovative part of the study: The speed estimation as the key step for the target classification and identification were conducted in a complex environment. The new algorithms have been proposed to improve the speed estimation performance. With the root mean square error sorting and comparison algorithm, the optimum parameters of the coherent reference function was found at the best speed estimation accuracy.

1.5 Thesis outline

The thesis structure is organized as follows:

Chapter 2 gives an overview of the FSR technology in the sequence of the monostatic radar, bistatic radar and the target Radar Cross Section (RCS) in the FSR system. In this chapter, the signature of the target is modeled in FSR. And the modeled signal is used as the reference function for the further coherent signal processing and detection.

Chapter 3 describes the FSR topology and the hardware system. The modelling of the ground vehicle as the major target of interest's RCS and signature are modeled and analyzed.

Chapter 4 introduces the detection processing of the ground target; the MonteCarlo simulation is performed for the analysis of the optimum target detection. The probability of

the false alarm and detection is reviewed as the standard of the procedure. The speed estimation and time domain normalization algorithms for the modelling target are introduced.

Chapter5 presents the Ground Forward Scatter Radar (GFSR) experimental configuration and initial result. The three test sites were classified as the ideal, medium complex and sophisticate environment by the numbers of vegetation surroundings.

Chapter 6 gives the speed estimation result by means of the proposed new algorithm and criterion. The comparison of the conventional speed estimation and the new speed estimation results are shown using the statistical proportions. The discussions of the improved automation multi-criterion fusion algorithm will be concluded.

Chapter 7 summarizes the main conclusion of the PhD work and followed with future research plan for the further development.

Chapter 2 Forward scatter radar overview

2.1 Introduction

In this chapter, the overview of FSR technology will be covered in detail. Section 2.2 starts with the forward scatter radar layout and coordinating system. Then, the bistatic range will be presented in section 2.3 using the Cassini ellipse and classic range functions. Section 2.4 explains the radar cross section by employing the Babinet's model and specified real target as example. Following section 2.5, specific ground targets RCS analysis with the Landrover modelling result will be provided. The target signature simulation results in the 2D Cassini plane will be displayed in section 2.6. The key parameters in the FSR system will be derived from the classic models. Finally, section 2.7 draws the conclusion of the whole chapter.

2.2 Forward Scatter Radar Layout

As the FSR configuration was briefly introduced in Chapter1, the simple geometry of the FSR is shown with potential targets. In this section, the more detailed coordination system will be provided together with the analysis.

First, the FSR coordinating system is shown in Figure 2.1. The target material is the perfect conducting metal, and the Tx and Rx are placed separately in a distance of D , the summation of d_R and d_T . The P is the cross point of the trajectory of object on the baseline. The target is moving at the speed of v and the direction to the point P while the intersection angle between the baseline is φ . The bistatic angle is β , α_h is the angle between the target to Tx and the baseline, β_h is the angle between the target to Rx and the baseline.

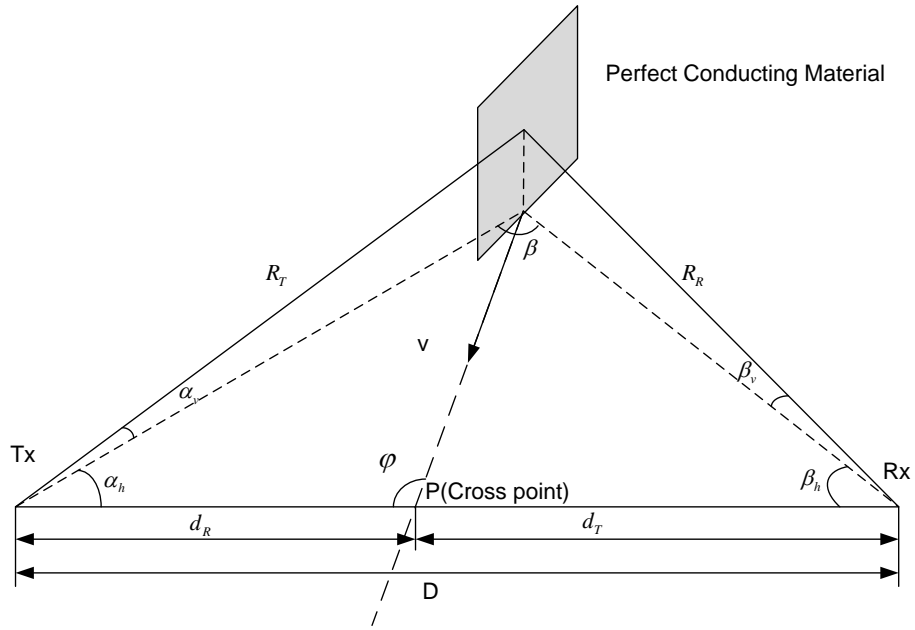


Figure 2.1 3D coordinating system for the FSR

Therefore, the target aspect angles can be calculated by the equation(2.1).

$$\alpha_h(t) = \tan^{-1} \left(\frac{vt \sin \varphi}{d_T + vt \cos \varphi} \right) \quad (2.1)$$

$$\beta_h(t) = \tan^{-1} \left(\frac{vt \sin \varphi}{d_R - vt \cos \varphi} \right)$$

2.3 Bistatic range

First of all, the bistatic range is given in the equation (2.2)[3],

$$(R_T R_R)_{\max}^2 = \left(\frac{P_T G_T G_R \lambda^2 \sigma_B F_T^2 F_R^2}{(4\pi)^3 K T_s B_n (S/N)_{\min} L_T L_R} \right) \quad (2.2)$$

where R_T is the range between Tx to target, R_R is the range between Rx to target, P_T is the transmitter power, G_T is the transmitter gain power of antenna, G_R is the receiver gaining

power of the antenna, λ is the wavelength, σ_B is bistatic radar target cross section, F_T is the factor of pattern propagation for Tx-antenna-to-target path, F_R is the factor of pattern propagation for target-to-Rx-antenna path, K is the Boltzmann's constant, T_S is the receiver noise temperature, B_n is the noise bandwidth, $\left(\frac{S}{N}\right)_{\min}$ is the signal to noise power ratio, L_T is transmit system losses, L_R is the receiver system losses. The signal to noise ratio is estimated by the equation (2.3) and given as followed.

$$\left(\frac{S}{N}\right)_{\min} = \left(\frac{P_T G_T G_R \lambda^2 \sigma_B F_T^2 F_R^2}{(4\pi)^3 K T_S B_n (R_T R_R)_{\max}^2 L_T L_R} \right) \quad (2.3)$$

In the bistatic radar range equation, since the system parameters are the same, the value $\left(\frac{P_T G_T G_R \lambda^2 \sigma_B F_T^2 F_R^2}{(4\pi)^3 K T_S B_n L_T L_R} \right)$ is a constant. Figure 2.2 shows the index of SNR curves which follows the Cassini ellipse. The SNR range is from 13dB to 27dB. As the target is moving across the baseline of the FSR, the SNR is increasing and reached the maximum when the target is located at the middle of the baseline.

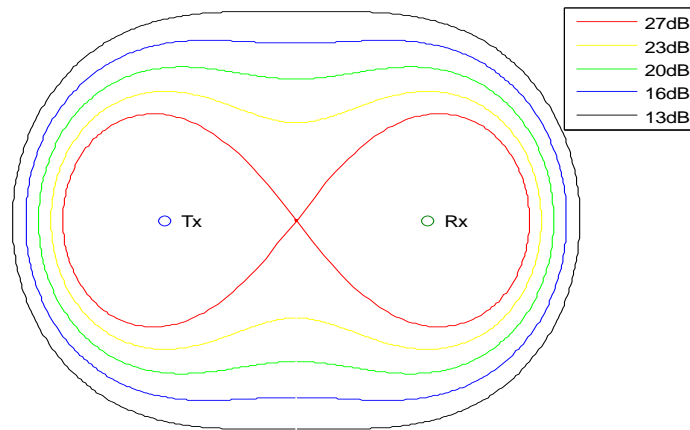


Figure 2.2 Cassini ellipse for bistatic radar with SNR index

2.4 *Radar Cross Section*

Due to the enhancement of the RCS, which the forward scatter radar can offer, more interest on the FSR than the monostatic radar systems has arisen. Mie [27] first solved the problem of calculating the turbid media optical properties which is concluded as Mie theory. There are three regions of interests when we investigate the RCS of bistatic radar target; they are forward scatter, bistatic and pseudo-monostatic region, which are classified by the bistatic angle. The forward scatter region is the main topic in this subsection.

The important issue of target detection is that the echo signal reflected by the body of target, in order to quantify the radar detection ability or target features, the RCS is introduced. The radar cross section of forward scatter radar is defined in the equation(2.4) [3].

$$\sigma = 4\pi r^2 \frac{P_s}{P_i} \quad (2.4)$$

Where P_s is the scattered power per unit solid angle and P_i is the power per unit in the wave plane incident, r is the distance from observation point to target.

Babinet's principle in radio frequency can be summarized as follows [42]: with two black thin diffraction screens, one is opaque object while the other one has the hole in the same shape and size to the first object. The diffraction pattern will be the same when the electromagnetic wave is generated by these two objects. These two object screens are called complementary screens. In this thesis, the theory is briefly explained and applied to the FSR configuration. The Babinet's model is shown in the Figure 2.3.

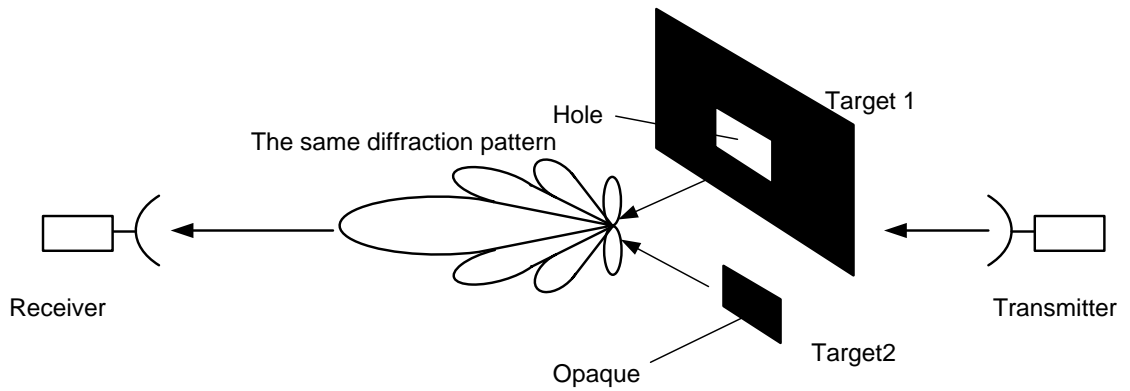


Figure 2.3 The Babinet's model for forward scatter radar at $\beta = 180^\circ$

In the forward scatter region, the target (black body) will not reflect the incident wave to the receiver when the dimension of the target is greater than the wavelength. The so called geometric optics or physical optics is applied under this condition shown in Figure 2.4.

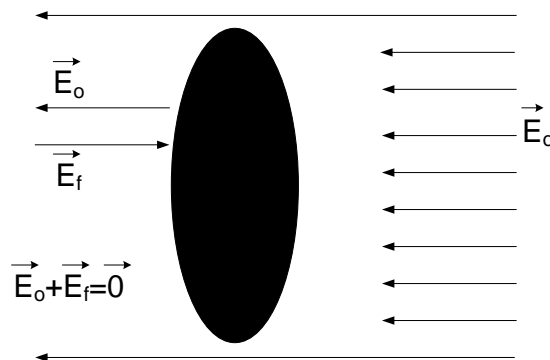


Figure 2.4 Shadowing field effect

Table 2.1 gives the RCS calculation of some typical shape objects, in the assumption that the dimension of the objects is larger than the incident wavelength and they are all made by the perfect conducting materials [43]. These basic calculations can assist the contracting process for the more complex multi-surface joint target, such as the vehicle target.

Table 2.1 RCS of the Simple objects which has larger dimension than the wave form

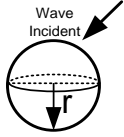
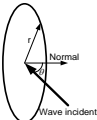
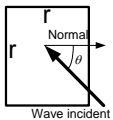
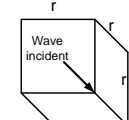
Object	Wave Aspect	Backscatter RCS	Forward scatter RCS
Sphere		πr^2	$\frac{4\pi^3 r^4}{\lambda^2}$
Circular flat plate		$\frac{16\pi^3 r^4}{\lambda^2} \cos^2 \theta \left(\frac{J_1(4\pi r \sin \theta / \lambda)}{4\pi r \sin \theta / \lambda} \right)^2$ $= \frac{16\pi^3 r^4}{\lambda^2}$ broadside	$\frac{4\pi^3 r^4}{\lambda^2}$
Square flat plate		$\frac{4\pi r^4}{\lambda^2} \cos^2 \theta \left(\frac{\sin(2\pi r \sin \theta / \lambda)}{2\pi r \sin \theta / \lambda} \right)^2$ $= \frac{4\pi r^4}{\lambda^2}$ broadside	$\frac{4\pi r^4}{\lambda^2}$
Trihedral corner reflector		$\frac{12\pi r^4}{\lambda^2}$	$\frac{27\pi r^4}{\lambda^2}$

Figure 2.5 shows the normalized RCS of perfect conduct sphere in dB and the signatures in three regions, the Rayleigh, Mie and Optical region. In the Rayleigh region, the dimension of the sphere is much smaller than the wavelength, while in the optical region, it is much larger than the wavelength, between the region of two, the Mie or resonance region represents that the radius of the sphere close to the wavelength.

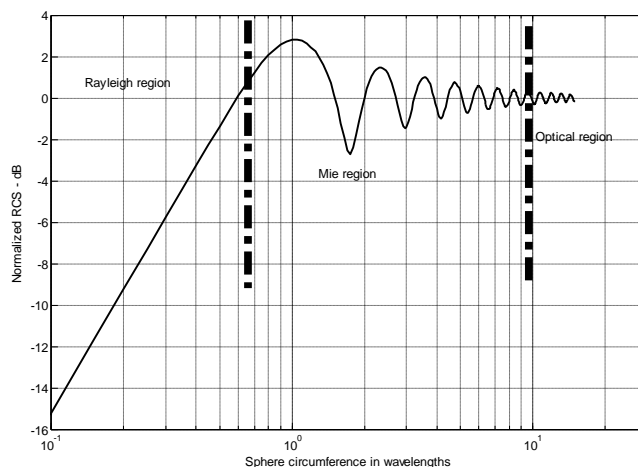


Figure 2.5 The Normalized backscattered RCS of a sphere in semi-log scale

It is sophisticated to get the RCS of the real objects in all conditions and range of wavelengths. However, some commercial simulation software, such as CST and Epsilon, are capable of getting rigorous and accurate RCS result of the complex objects. The RCS simulation result will be displayed in chapter 3.

2.5 Specific ground targets RCS analysis

In this section, the RCS of the same target is simulated in order to compare the target specifications under different frequencies. Due to the complex shape of the real vehicle, the accurate RCS cannot be obtained by the simple equations shown in the previous sections. In this case, the more powerful integral equation solver (I-solver) for the electrically large size target should be applied to obtain the RCS. The modelling of specific car model Landrover is constructed in the Computer Simulation Technology2014 software environment. The frequency of the emitting signal is set at 64MHz, 135MHz, 173MHz and 434MHz CW signals. They are the real FSR channel frequencies, and the simulated target main body materials are set to be aluminium loss metal, which is closer to the real target.

Figure 2.6 shows the FSR configuration with the vehicle target Landrover, the transmitter and the receiver. The vehicle target body is assigned to be the perfect electric conductor (PEC) with aluminum loss metal. In order to make the modelling structure more close to the real environment, all details are carefully designed and processed. The materials of the target are listed in Table 2.2.

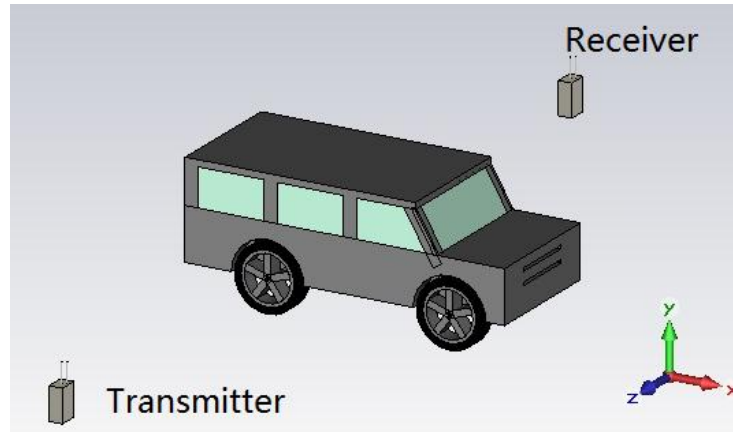


Figure 2.6 FSR target with the Tx and Rx

The modelling target contains more than 100 independent objects and the surface mesh is about 900,000 surface cells. In order to simulate the real experiments, there is a human driver and four seats inside of the car shown as the perspective view in Figure 2.7 . As we can see that the modelling configuration are very close to the real physical parameters. The human is assigned to be 70% water with vivid organ which can be found in the perspective view. The wheels are designed with aluminum loss metal hub and rubber tyres. The window is also modelled with glass material as the body unit part.

Table 2.2 Landrover model component properties in CST Model

Components	Material
Vehicle body	Aluminium loss metal
Tyres	Rubber
Window	Glass

Human Driver	70% water
Seats	Aluminium loss metal
steering wheel	Robber
Length	4.7m
Width	2.2m
Height	1.9m

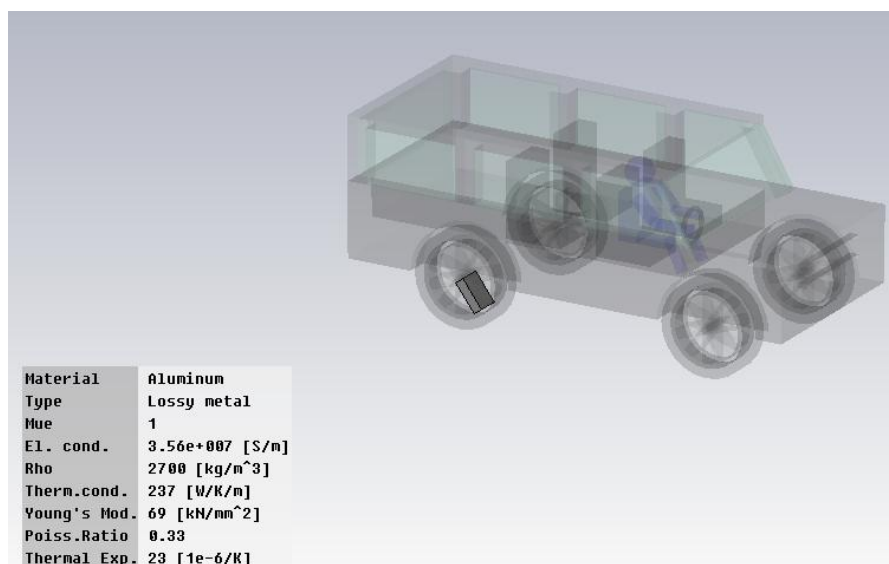


Figure 2.7 Modelling target of ground vehicle in perspective view

Figure 2.8 shows the plane wave illumination of modelling target at 434MHz on the right hand side. In the real experiment, the source of the plane is placed at the location of the Tx, and the target can cross the baseline at different direction, which means the plane source could be located on the left hand side.

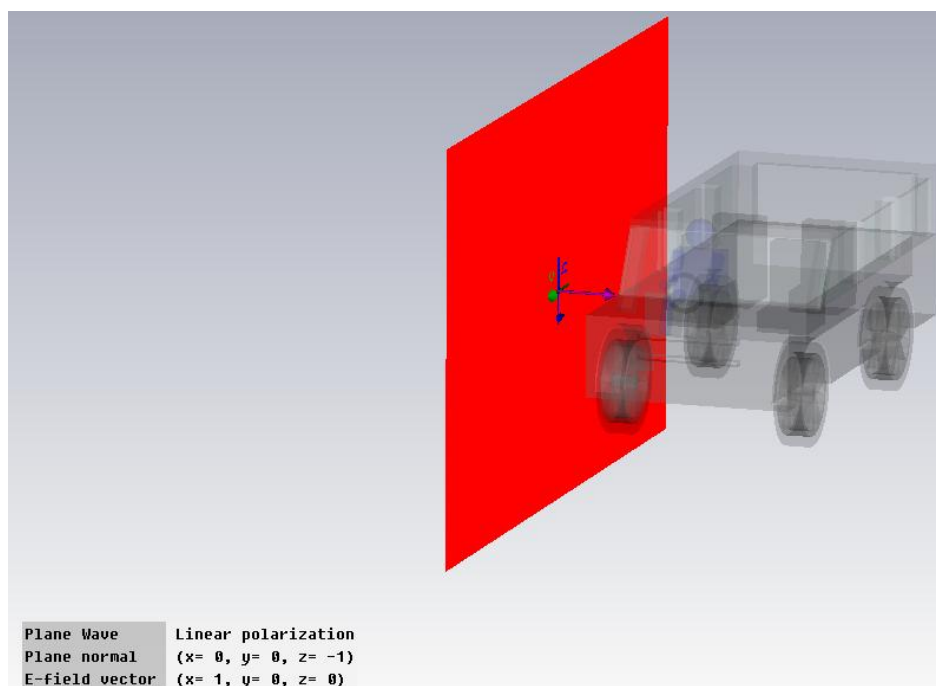


Figure 2.8 Plane wave illumination from the right hand side of the vehicle at 434MHz

Figure 2.9 displays the 3D RCS field calculated from the modelling target in the spherical polar coordinates with the maximal RCS of 34.04 dBm^2 at 434MHz. The integral equation solver is used. The wavelength of the 434MHz is 0.69m while the target length is 4meters and 2meters in height, respectively. The wavelength of the plane size ration is 0.345 to 0.17, so the wave diffraction around the target body is in the Mie region.

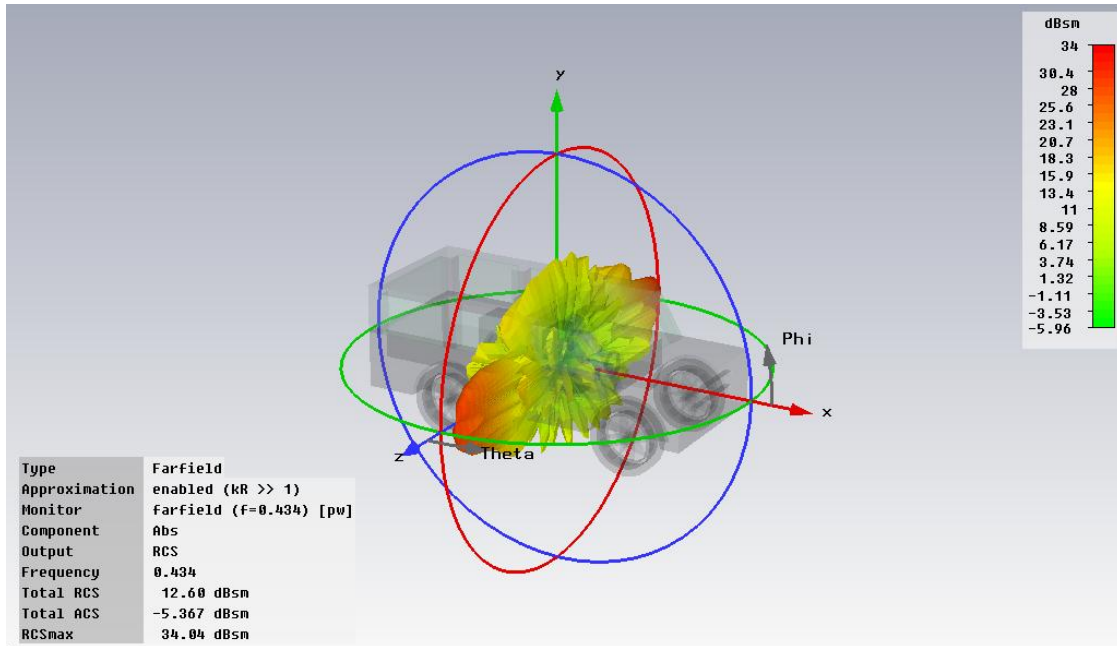


Figure 2.9 The 3D RCS of the vehicle target

Figure 2.11 shows the RCS field in polar coordinates as a function of the spherical angle theta. The far field forward scatter receiver is presented at a 180 degree angle and the polar diagram is displayed. The 0 degree angle indicates the backscatter RCS value.

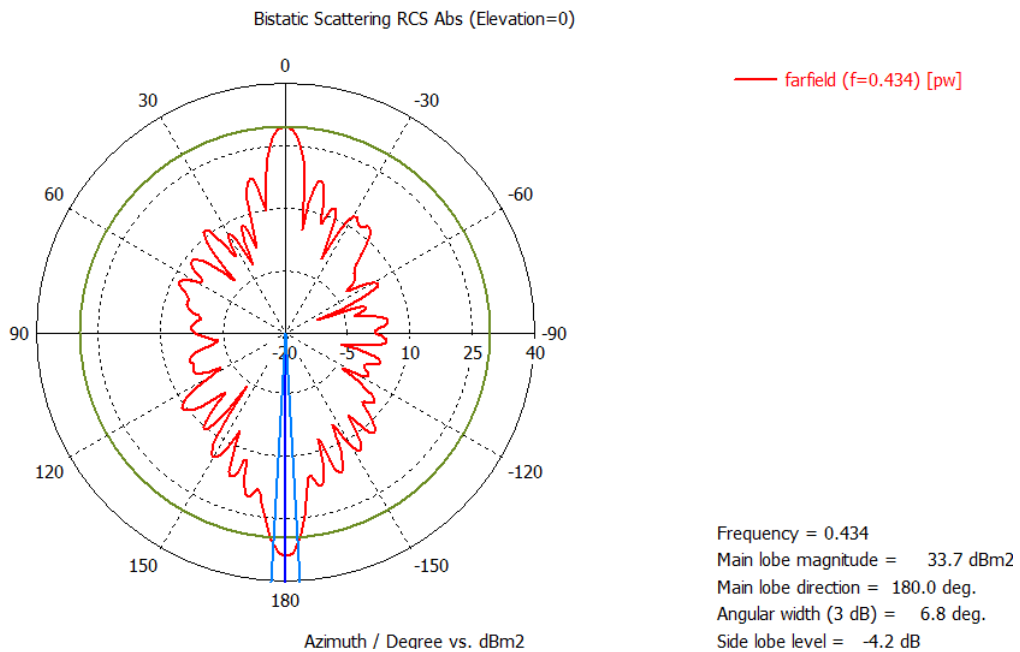
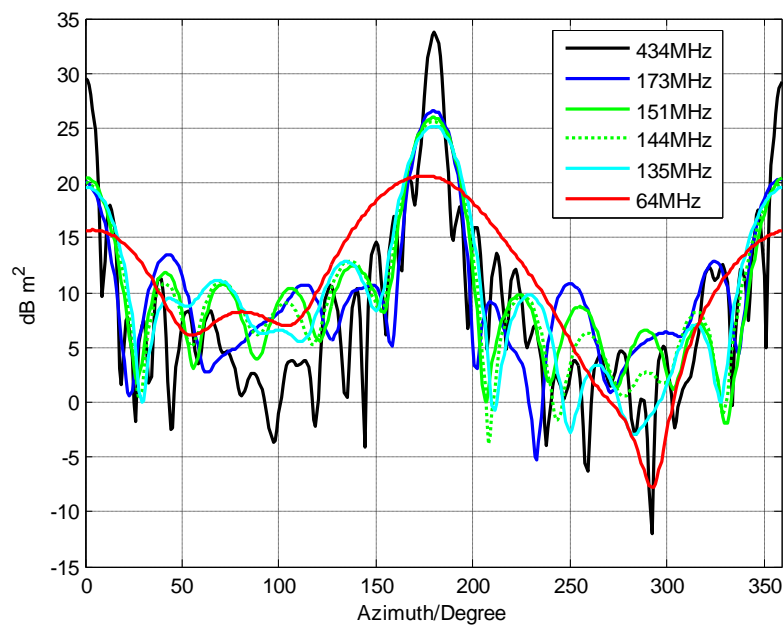


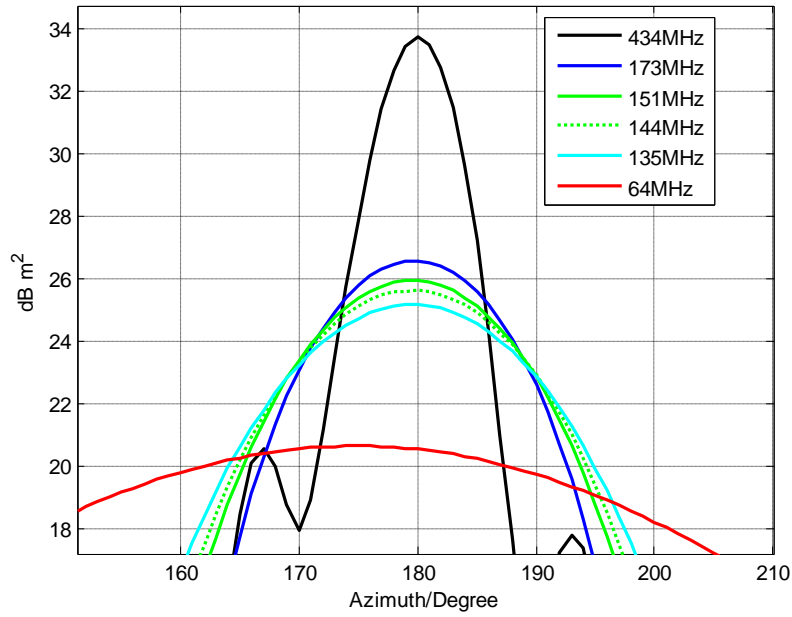
Figure 2.10 RCS farfield as a function of theta for 434MHz

The polar graphs of the RCS analysis for the frequencies from 64MHz to 173MHz can be found in Appendix A. Then we can compare the FS CS plots for the multi frequencies. The central of the curves indicate the maximum of the magnitude at 180 degrees. Figure 2.11 (b) shows the zoomed in details of the RCS curves from 150 to 210 degree, the difference of the RCS between the 434MHz and the 64MHz is 13.3dBm^2 .

Also, the RCS difference for the frequency range from 135MHz to 173MHz has an increment of 1.8dBm^2 . It is also shown in Figure 2.11 that the RCS main lobe width of the 64MHz is wider than the other higher frequencies, for the reason that the wavelength of the higher frequency is shorter than the 64MHz.



(a)



(b)

Figure 2.11 Bistatic scatter RCS comparison in multi frequencies (a) Simulation FS CS for the multi frequency (b) The zoomed in details

2.6 Target signature in FSR

The time domain target signature modelling result for small object can be found in[44]. Taking into the consideration that the target is moving along the middle path between the Tx and Rx shown in the Figure 2.12. The target is a dot object, while the Tx and Rx are the same size. The ellipse is within the azimuth projection plane, and they are the Doppler phase contours. The total target signal $U_R(t)$ is shown in the equation (2.5)

$$U_R(t) = u_L(t) - u_{tg}(t) \quad (2.5)$$

where $u_L(t)$ is the leakage power from Tx to Rx ;

$u_{tg}(t)$ is the reflection power from target

When the target crosses the baseline at the time of 0, the phase different of the $u_L(t)$ and $u_{tg}(t)$ is 0, and the amplitude of the receiving power reaches to the lowest value. As the target is moving with constant speed and direction and at the contour of phase π or $-\pi$, the $u_L(t)$ and $u_{tg}(t)$ is in phase and the magnitude reaches to the peak. When the $u_L(t)$ and $u_{tg}(t)$ is off phase and the amplitude reaches to the minimum. The whole process is called the amplitude and phase modulation effect.

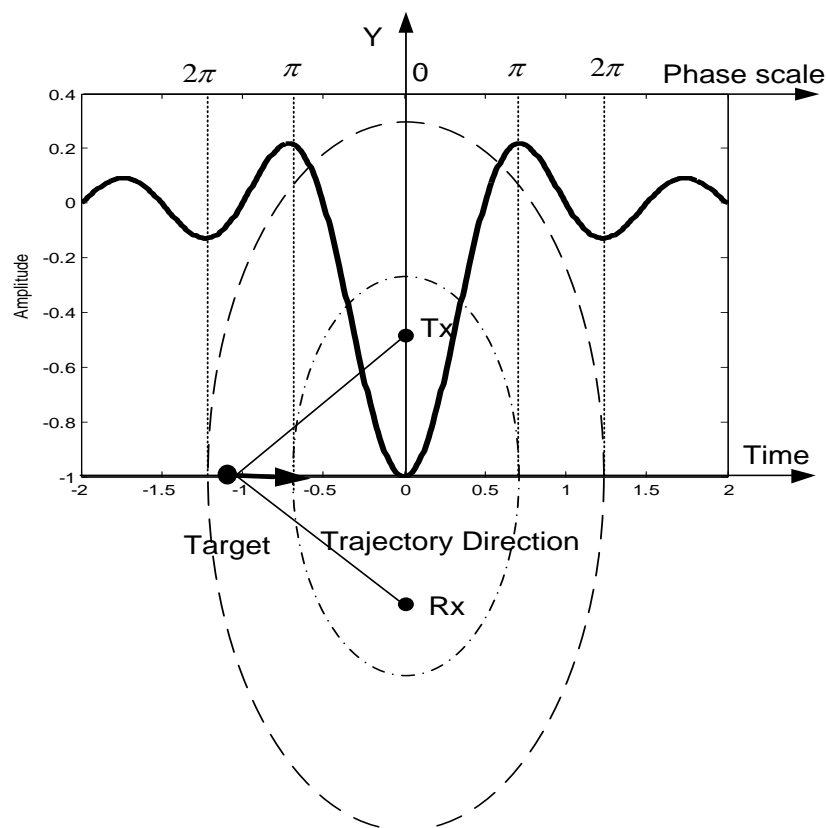


Figure 2.12 Target signature in 2D Cassini plane

It is difficult to model the exact target signatures for the practical situation at the receiver site. The size of the target is unknown and the reflection waveform can vary due to the radiation patterns and object materials etc., however, we still can model the closest target signature which is called the reference function under the assumption that we consider all the parameters in the real environments[45].

When the Tx and Rx are keeping still, and the target is the only moving object, the target Doppler shift is given by:

$$f_D = \left(\frac{2v}{\lambda}\right) \cos \delta \cos\left(\frac{\beta}{2}\right) \quad (2.6)$$

where v is the target velocity magnitude, λ is the wavelength of transmitting signal, δ and β are shown in the Figure 2.13[5].

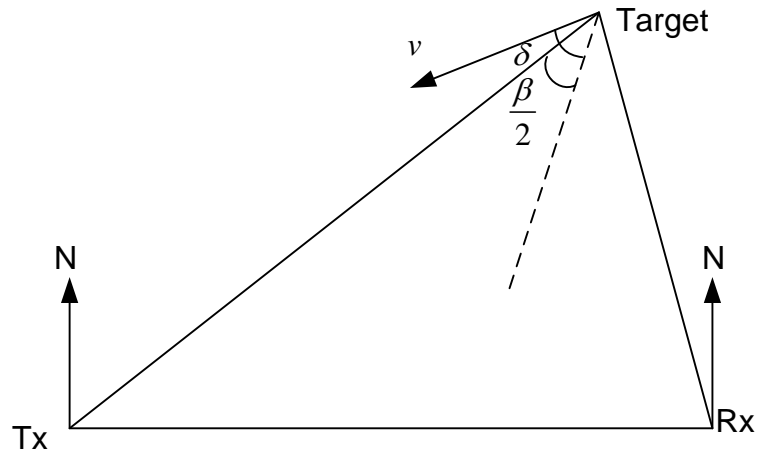


Figure 2.13 Bistatic doppler geomery

The transmitter signal is assumed to be the continuous wave and the angular frequency is ω_0 :

$$S_T(t) = \sqrt{P_T G_T} \cos(\omega_0 t + \psi_0) \quad (2.7)$$

where P_T is the transmitter power, G_T is the gain of the transmitter antenna. ψ_0 is the initial phase of the signal. The signal received will be the sum of the scattering receiver signal and the leakage signal direct from the receiver. As the target is moving, the so called pseudo Doppler effect will be extracted and the target RCS can be summarized as follows[45]:

$$\begin{cases} \sigma(t) = \frac{4\pi S^2}{\lambda^2} \sin^2[\alpha_h(t) + \psi] \cos^2[\alpha_v(t)] F_1^2(*) F_2^2(*) \\ F_1(*) = \text{sinc} \left[\pi \frac{l \sin[\alpha_h(t) + \psi_0]}{\lambda} \sin[\alpha_h(t) + \beta_h(t)] \right] \\ F_2(*) = \text{sinc} \left[\pi \frac{h \cos[\alpha_v(t) + \psi_0]}{\lambda} \sin[\alpha_v(t) + \beta_v(t)] \right] \end{cases} \quad (2.8)$$

Where $F_1(*)$ is the target's secondary antenna azimuth pattern, and $F_2(*)$ is the elevation pattern of secondary antenna, l is the length of the target, h is the height of the target, λ is the transmitter signal wavelength. Therefore, the forward scatter radar cross section $\sigma(t)$ relies on the parameter of the target dimension and wavelength.

There is another important factor, propagation loss, which is the reduction in the power density or attenuation as the waveform transmitted in the space, should be considered in the condition of the ground forward scatter radar deployment. As the height of antenna is relatively low, normally no more than 1 metre in the system, the ground reflection is the main factor, and the assumption of the perfect ground reflection coefficient is -1. The propagation loss factor is

$$L_T(t)L_R(t) = c \frac{h_t^2 h}{R_T^4(t) \cos^4 \alpha_v} \times \frac{h_r^2 h^2}{R_R^4(t) \cos^4 \alpha_r} \quad (2.9)$$

where c is constant coefficient factor relates to the environment, h_t is the height of transmitter and h_r is the height of receiver, h is the height of target, $R_T(t)$ is the range from transmitter to the heart of target, $R_R(t)$ is the range from target to receiver which can be written as:

$$\begin{cases} R_T(t) = \frac{\sqrt{(vt \cos \psi + d_T)^2 + (vt \sin \psi)^2}}{\cos \alpha_v} \\ R_R(t) = \frac{\sqrt{(vt \cos \psi - d_R)^2 + (vt \sin \psi)^2}}{\cos \beta_v} \end{cases} \quad (2.10)$$

The two ranges, transmitter-target, target-receiver and dimension of the target can influence the propagation loss factor $L_T(t)L_R(t)$.

2.7 Conclusion

The general introduction to the FSR system has been provided, and the modelling of the forward scatter RCS is analyzed with the details using motion procedure. Although there are restrictions within the FSR system, we can make most use of accounting the other main advantages of the FSR deployment. For instance, the enhanced RCS detection ability from FSR can provide us with a higher probability of detection. The specific ground target RCS analysis in the CST modelling environment has provided the initial radiation scattering result for the target electromagnetic features. This will be the fundamental proof for processing the real recorded data. The following chapter will discuss how the data is collected by the GFSR system and the GFSR system configurations.

Chapter 3 Ground FSRsystem

3.1 Introduction

In this chapter, the Ground Forward Scatter Radar (GFSR) system is introduced starting with the topology and the vehicle target description. The topology of the GFSR is similar to most of the FSR system distinguished by the features that detection target is ground vehicles or human intruders. Section 3.2 shows the GFSR topology and the vehicle target. The type and dimension of the targets determines the system parameters such as the operational frequency and the baseline length etc. The GFSR hardware descriptions are presented in the section 3.3. The hardware was applied in the real experiments. In section3.4, the data structure at the receiver reception side is briefly introduced for better understanding when processing the signal in the multiple channels in the next chapter. Finally, the conclusions are drawn in section3.5.

3.2 Ground FSR system topology and vehicle target

In Chapter2, we discussed the FSR coordinating system in detail. In this section, we will mainly discuss the deployment of GFSR sensors used in the real practice environment. The least configuration of GFSR can be organized by only one pair of transmitter and one receiver. The GFSR sensor system topology is shown in Figure 3.1. The cube target represents the vehicle is moving within the same plane(XOY) with the Rx and Tx. The h_1 and h_2 indicates the height of the antenna and the connection line between two is the baseline.

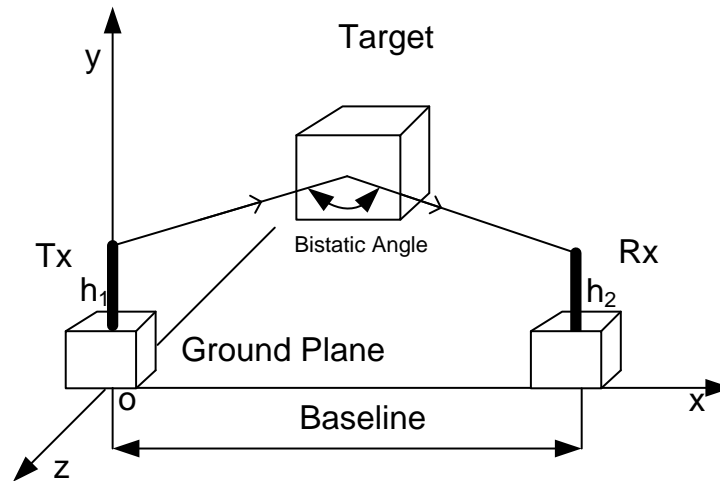


Figure 3.1 Ground FSR sensor topology

The vehicle target is Landrover. The real target body is shown in Figure 3.2. The target side surface is about 8.93m^2 using aluminum as body material. It is essential to acquire these parameters when we seek to simulate the RCS for the target.



Figure 3.2The vehicle target for the GFSR experiment.

3.3 GFSR hardware description

The GFSR system utilizes the Continuous Wave (CW) as the approach to detect and classify the ground target. The CW waveform is transmitted in the form of stable wave $\cos 2\pi f_0 t$. There are a number of advantages which CW radar possesses [4]. First, a higher mean power of the transmitter can be obtained comparing it with the pulse radar, Secondly, the

manufacture and design of CW radar required less complexity and lower costs in terms of hardware. Thirdly, the Doppler effect can be observed when the target travel between the transmitter and receiver of CW radars.

The hardware is designed and made by Dr Vladimir Sizov at the Microwave Integrated System Laboratory (MISL) of the University of Birmingham. The initial experiments were carried out at multiple sites, Pritchatts car park at the University of Birmingham and Tilesford airfield at Pershore. Numbers of first hand database are collected from the test sites.

3.3.1 Operating Frequency and Power budget

The initial feasibility research in [39] used 900MHz frequency CW radar as the transmitting source. The baseline length is 17meters and directional Tx and Rx's antennas are placed toward each other with 1 metre height above the ground. Many of the random vehicles passed through the baseline and the initial database demonstrates that the system can be used for detection and classification. In our system, the multiple frequencies at VHF and UHF bands are used in our GFSR system. As the RCS of the target using these frequencies are simulated in section 2.5, the wavelength and the output power for each frequency are listed in Table 3.1. The 64MHz has the output power of 20dBm, however the rest of the frequencies are 10dBm.

Table 3.1 The GFSR operational frequencies

Operating Frequency (MHz)	Wavelength (m)	Output Power(dBm)
64	4.69	20
135	2.22	10
144	2.08	10
151	1.99	10
173	1.73	10
434	0.69	10

At the reception side, the receiver has to apply the attenuator to reduce the power of the signal in the short baseline range cases. Figure 3.3 shows the relationship between the input power in dBm and the Received Signal Strength Indicator (RSSI) output voltage which was produced by Vladimir[46]. The RSSI is the measured signal strength level at the receiver side [47]. It is done in the intermediate frequency (IF) stage before the IF amplifier. In the figure, all Rx channels have close sensitivity and linear detection range. They are from -70 dBm to -110 dBm at the RSSI output voltage level from 0.8 to 2.3V.

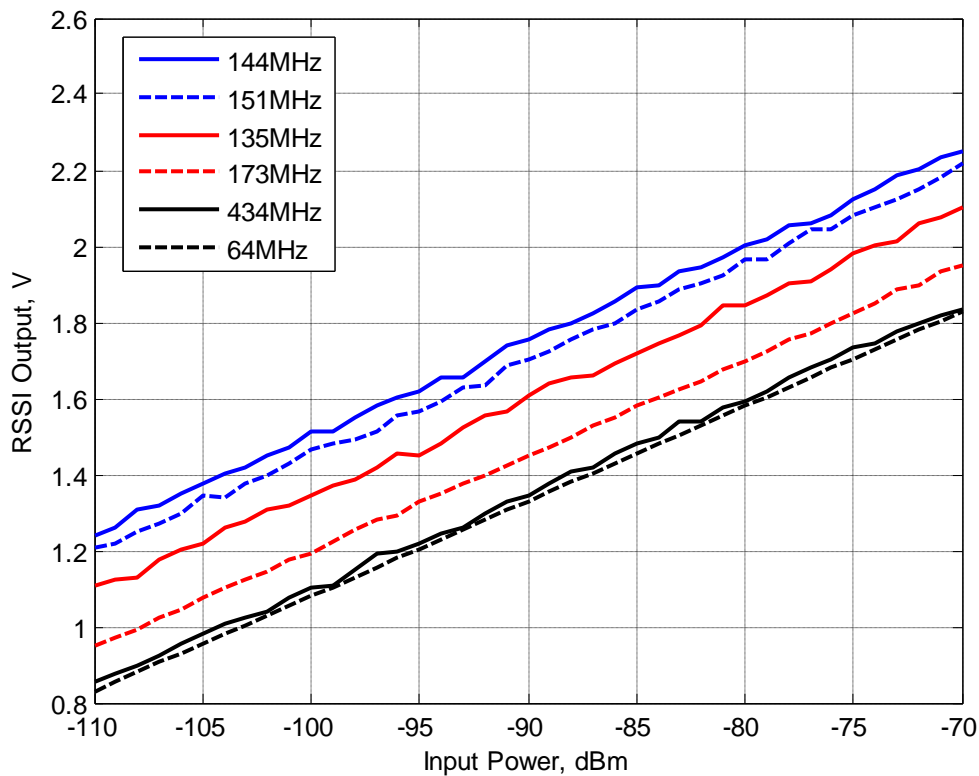


Figure 3.3 Receivers detection range

In Table 3.2, the attenuators (att) used in the experiments depend on the frequency and baseline lengths. It is shown that the longer baseline length, 64MHz at 100 m condition for example will use 10-20dB for the R_x . Whereas when the baseline length is more than 100m, no attenuators are need in the R_x and T_x .

Table 3.2 Attenuators (att) used in the experiments

Frequency channel	Baseline length		
	50 m	100 m	>100 m
64 MHz	20 dB for R _X 10 dB for T _X	10-20 dB for R _X	No att.
135, 144, 151 and 173 MHz	10 dB R _X	No att.	No att.
434 MHz	0-10 dB R _X	No att.	No att.

3.3.2 Transmitter

This thesis focuses on the VHF and UHF frequency applied in the FSR system and uses the RadioMetrix as the transmitter model of opportunity. The transmitter and receiver keep stationary while the target moving across the baseline within the vicinity of the detection zone. The transmitter hardware block diagram is shown in Figure 3.4. The signal generator utilizes the RadioMetrix [48] VHF and UHF band transmitter. The charger circuit and power supply provide the transmission power to the signal generator blocks using the RadioMetrix model. With the LED indicator, the status of the transmitter can be read when the signal is rolled out. The antenna use the directional and Omni directional types which will be shown in the following sections.

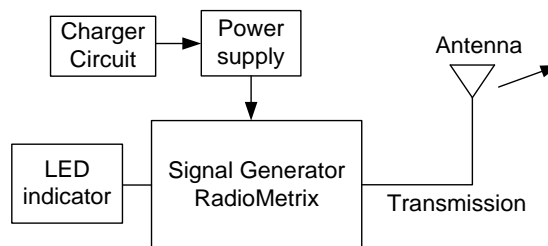


Figure 3.4 Transmitter block diagram

Figure 3.5 shows the block diagram of the signal generator RadioMetrix[48]. The module can offer specified low power, reliable data link in the outdoor environment. It is suitable for the specified FSR application which requires low cost multi-frequency channel operation. It is capable of connecting multi frequency channels and programmable for the selection of

predefined CW waveforms. In the block diagram, the power supply connects to the Centre Processing Unit(CPU) and synchronization (SYN) block, the channel selector send the command to the CPU for the predefined waveform and configure the frequency. The transmitter data provides the phase and amplitude information. They are modulated to the amplifier units and send out by the RF output port via the LPF block.

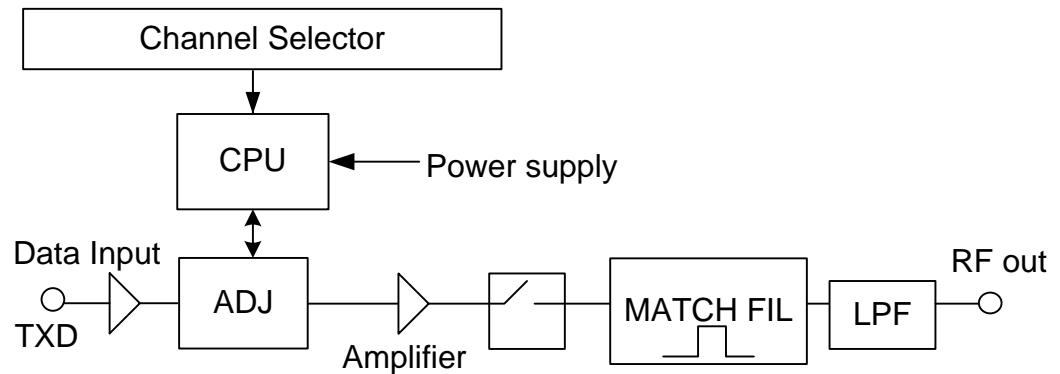


Figure 3.5 The RadioMetrix (RM) transmitter inner block diagram

The real boxed transmitter is shown in Figure 3.6. The black arrow marked on the top surface indicates the direction of device placement. The pointing direction of the Tx and Rx is determined by the paired device purpose and will be explained in the following sections.

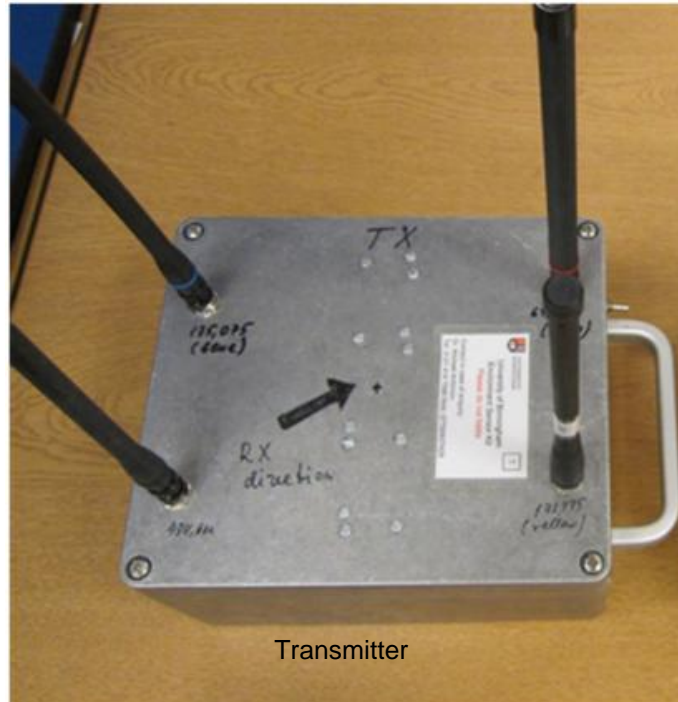


Figure 3.6 Transmitter with antennas

3.3.3 Receiver

The receiver block diagram is shown in the Figure 3.7. The charger circuit provides the converter from Alternation Current (AC) power to DC (Direct Current) into the battery, and the battery provides the power to the signal receiver module for the reception of the waveform from the Received Signal Strength Indication(RSSI) channel. Then the Analog Digital Converter (ADC) modulates the signal to digital signal and sends to the PC.

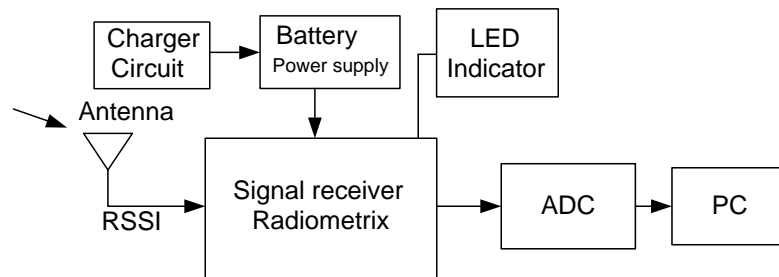


Figure 3.7 The receiver block diagram

Figure 3.8 shows the receiver box without the antennas. On the top of the metal shield, there are four aerial connectors which indicate the four frequency channels. They are 64MHz, 135MHz, 173MHz Omni directional and 434MHz directional channels. The black arrow in the centre of the box also indicates the direction of the placement in the experiments.

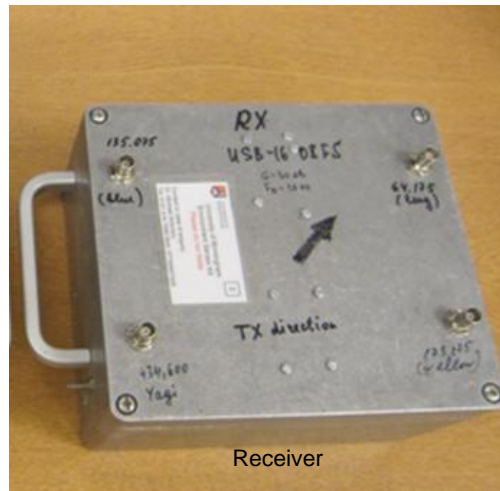


Figure 3.8 Receiver without antennas

The orientation of the Tx and Rx is shown in Figure 3.9 . When placing the Tx and Rx, we want to make the best use of the frequency channels. In order to reduce the antenna array effect caused by the multiple channel communication system, the placement orientation of Rx and Tx can be the solution to the distortion of the Omni-directional pattern of monopole antennas. It was found that antenna array effect present complex in multi-channel modules antenna system which distort Omni-directional pattern of monopole antennas used and makes the modules sensitivity and radiated power depending on modules orientation. The four channel device is more sensitive to orientation because of close frequencies of antennas for 135 to 173 MHz channels.

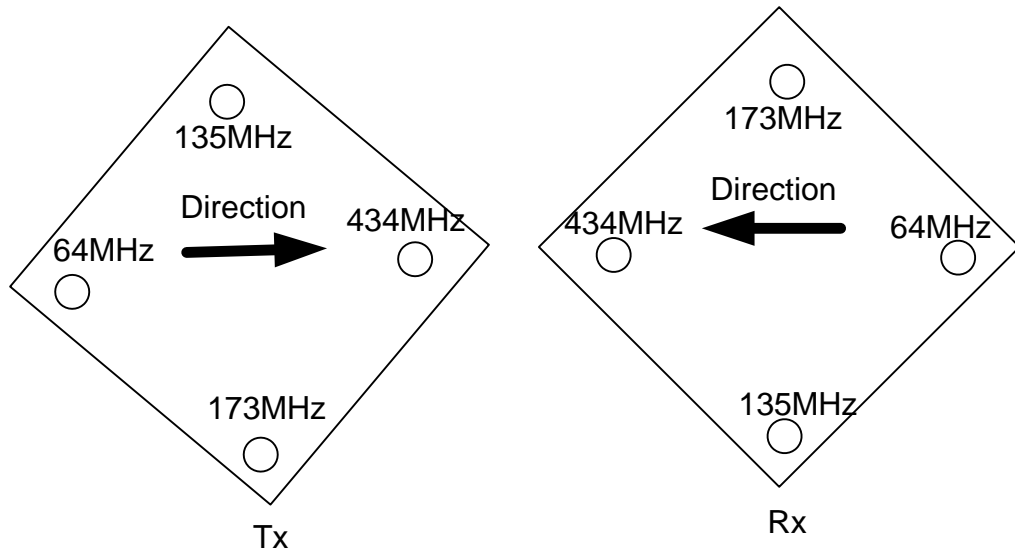


Figure 3.9 Mutual orientation of Tx and Rx devices

3.3.4 Antenna

We applied the Omni directional helical antenna to the lower frequency in VHF and UHF channels and one directional antenna to the 434MHz channel. The helical antenna, which is Omni directional, can radiate the power of waveform uniformly in all directions within one plane[49]. Figure 3.10 shows the helical antenna property at the frequency of 64MHz. The green rotation loop indicates the shape and the current distribution(a), while the radiation intensity distribution is uniformly emitted outside of the space (b).

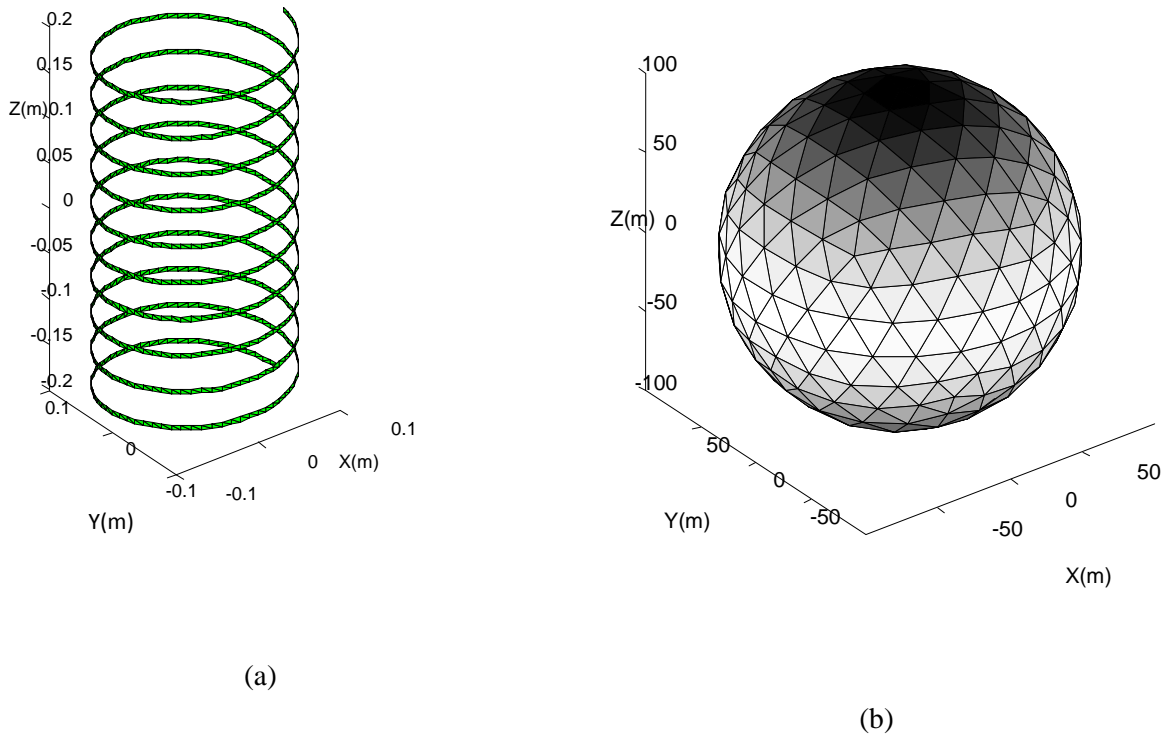


Figure 3.10 (a) The helical antenna surface current distribution (b) The radiation intensity distribution of the helical antenna

Figure 3.11 shows the radiation pattern of the centre fed 10 turn normal mode helical antenna at 64MHz.

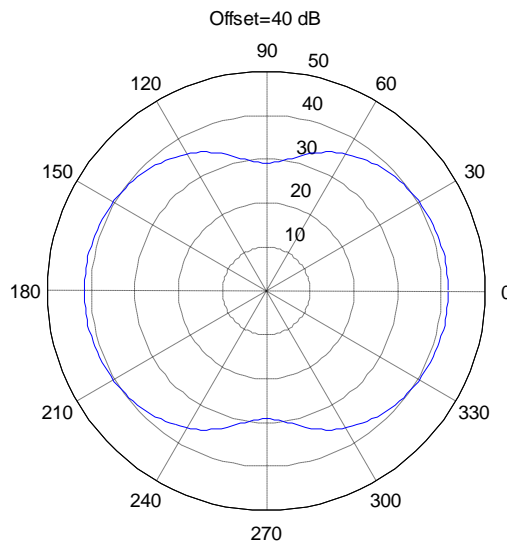


Figure 3.11 The radiation pattern of the centre fed 10 turn normal mode helical antenna at 64MHz

We also applied the 434MHz Yagi directional antenna in the trial and the radiation pattern of antenna is shown in Figure 3.12[50]. The front to back propagation ratio is nearly 15dB. The front gain at 0 degree is 0 dB while the back gain at 180 degree is -15 dB.

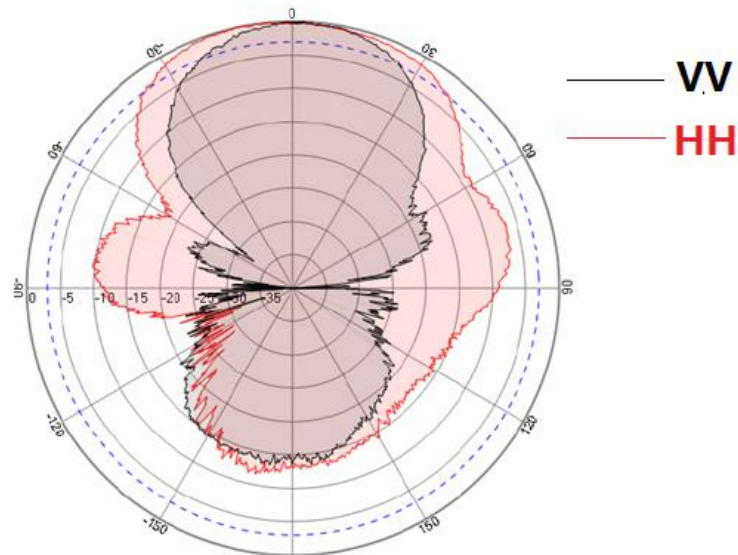


Figure 3.12 Directional antenna radiation pattern

The electrical specifications of antenna are listed in Table 3.3. The frequency range contains the 434MHz and the gain is 10dB at 450MHz.

Table 3.3 Yagi antenna electrical specifications

Frequency range	390-480MHz
Nominal Impedance	50 Ω
Gain	10dBi at 450MHz
Polarization	Vertical
F/B ratio	15dB

Figure 3.13 shows the image of antennas used in the GFSR system. The antennas are all connected directly to the attenuators for the special requirement of the power link budget in the short baseline length.

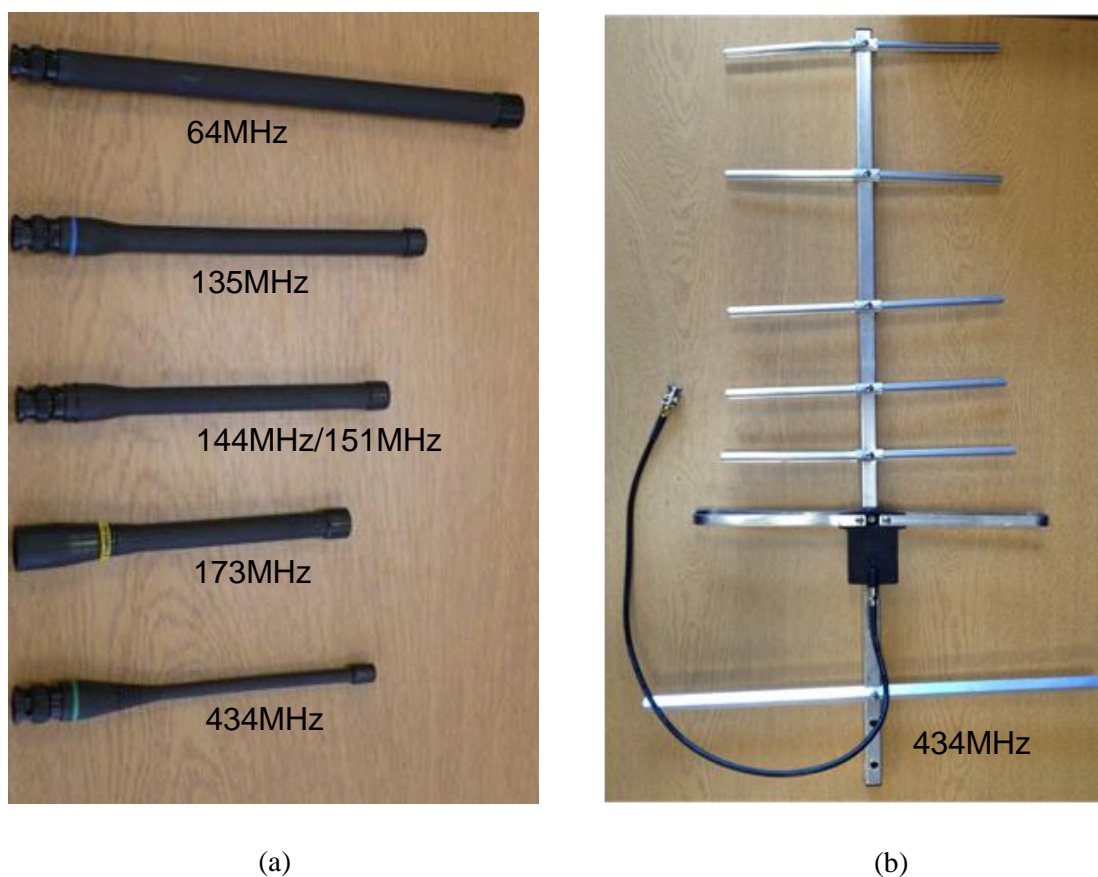


Figure 3.13 Antenna (a) Omni directional helical (b) 9dB Directional Yagi

3.4 *GFSR software description*

The GFSR software system can be divided into two parts, one is acquisition, the one is processing. The acquisition part is the raw radio signal strength capture procedure. The code is written by Dr Vladimir Sizov in Mathcad and can connect the ADC processing board. The sample frequency and channel selection can be done by running the acquisition code. The raw file is in the binary format.

The processing software is the post processing step for the further analysis and understanding the features of the signals or signatures. This part of the software is written in Matlab. The functions are programmed to finish the data base reorganization, frequency

signal separation, modelling of the target signatures, target detection, target classification and so on.

3.4.1 Data structure

The experimental data are collected from the receiver using the Analogue to Digital Converter (ADC) and the data is stored in files directly on the laptop via a USB cable. The data acquisition program is developed by Dr Vladimir Sizov. It is noteworthy that the array is stored in the order of frequency and channels. The data structure is registered in the hardware configuration. For example, when the 4 frequency device 4N_receiver is in the reception mode, the initial 8 ADC results are stored parallel from 4 different frequencies with two dependent channels, Doppler and RSSI. Moreover, in the Doppler Channel, it captures the transformed RSSI signal with Doppler effect feature. In the further processing, only the RSSI channel data is used as the main source data. In addition, both of the data formats are shown in Figure 3.14. At the time T_0 , all of the eight frequency channels captured the data and convert the analogue value into digit in the Array A_0 to A_7 in a mean while. Each cell in row corresponds to its own frequency channels and stored in the order of lower to higher frequency.

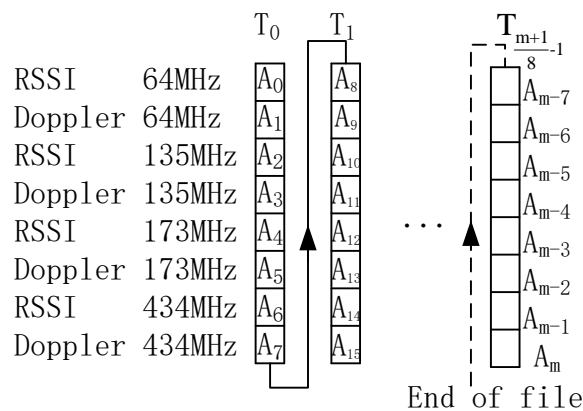


Figure 3.14 Data storage format in the bin file

3.5 Conclusion

In this chapter, the hardware and software design have been introduced. The multiple continuous frequency channel system will meet the short range bistatic radar detection requirement. The features of the power budget and antenna radiation pattern were also highlighted in order to get a better understanding how the reception signals acquired. At last, it was very beneficial to introduce the data structure storage in the software side of the system. In the following chapter, the modelling and recorded signals captured by the hardware system will be used for the target detection algorithm design.

Chapter 4 Automatic target detection

4.1 Introduction

The Automatic Target Detection (ATD) requires the statistical framework for the prediction of the presence of the target. There are little publications on the statistical ATD in FSR. In a broad sense, the process of automatic detection in FSR is similar to the appropriate process in traditional radar. Nevertheless, the peculiarities of FSR shall be taken into account and will be considered in this section alongside with the automatic speed estimation as an inherent part of the coherent detection.

This chapter provides the MonteCarlo simulation result for the probabilistic analysis, the probability of detection(P_d) and probability of false alarm(P_{fa}), to compare the coherent and non-coherent detection block algorithm. The modelling rectangular sinusoidal and recorded target signals are tested in both of the blocks. However, in most cases, the coherent detection performs better than the non-coherent detection in the traditional pulse radar system, which has a weak echo signal in a low SNR, and the non-coherent detection requires less computer calculation consumption. The non-coherent detector can be useful in the FSR system, because the higher SNR can be easily acquired so that the non-coherent detection can be utilized in some practical detection scenarios. Using the same detection block diagrams, the software filter bank parameters are optimized. This chapter also introduces the short time wavelet transform to show the recorded signal with the short window spectrum power indicator. The automatic target classification algorithm is introduced using the principal component method.

4.2 *Automatic target detection*

ATD is a signal processing procedure which requires the extraction of useful target signals. Moreover, the primary goal is to increase the SNR and make the target signal significant. In order to identify the target signal from the background of clutters or noises, the target detection algorithm should be developed. The main target detection method includes the ideal coherent detection, coherent detection, practical coherent detection. The three blocks are shown in this chapter and illustrated with their results. The probability of detection (P_d) and the probability of false (P_{fa}) is introduced as the statistical terms to indicate the performance of the detectors.

Detection of a radar signal is based on establishing a threshold at the output of the receiver. If the receiver output is large enough to exceed the threshold, a target is said to be present. If the receiver output is not of sufficient amplitude to cross the threshold, only noise is said to be present. This is called threshold detection[3]. When a large echo signal from a target is present, it can be recognized based on its amplitude relative to the Root Mean Square (RMS) noise level. If the threshold level is set properly, the receiver output would exceed the threshold if a strong target echo signal were present along with the noise. If the threshold level were set too low, noise might exceed it and be mistaken for a target; this is called a false alarm. If the threshold were set too high, noise might not be large enough to cause false alarms, but weak target echoes might not exceed the threshold and would not be detected. When this occurs, it is called a missed detection. A threshold level is shown in Figure 4.1 by a red dash line, and the amplitude peak level A,B and C indicate the presence targets. It is not very difficult to decide that a target echo signal is present if the signal is large enough and exceed the threshold. However, considering the two weaker signals at B and C, representing two target echoes of equal amplitude. The

noise accompanying the signal at B is assumed to be of positive amplitude and adds to the target signal so that the combination of signal plus noise crosses the threshold and is declared a target.

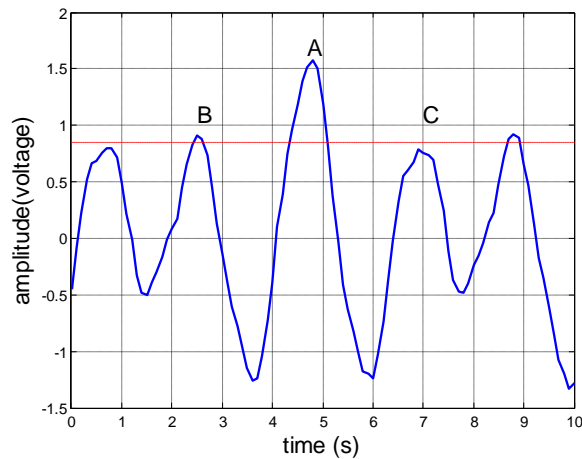


Figure 4.1 Envelope of the radar signal and threshold

At C, the noise is assumed to be subtracted from the target signal, so that the resultant signal and noise do not cross the threshold and is a missed detection. The ever-present noise, therefore, will sometimes enhance the detection of marginal signals, but it may also cause loss of detection. The signal at C would have been detected if the threshold were lower. However, too low a threshold increases the likelihood that noise alone will exceed the threshold and be improperly noted as detection. The selection of the proper optimal threshold is therefore a compromise that depends upon how important it is to avoid the mistakes of either (1) failing to recognize a target signal that is present (missed detection) or (2) falsely indicating the presence of a target signal when none exists (false alarm)[3]. The Signal-to-Noise Ratio (SNR) was mentioned in the first chapter; it is a better measure of a radar's detection performance. The relationship between the two will be introduced in the following sections.

The concept of the Probability Density Function(PDF)[51] is important in the detection of radar signals with noise. The noise is a random phenomenon and should be

described in probabilistic terms. Probability is a measure of the likelihood of the occurrence of an event. The scale of probability ranges from 0%(0) to 100%(1). An event that is certain has a probability of 100% and an impossible event has a probability 0. The intermediate probabilities are assigned so that the more likely an event, the greater is its probability. Probabilities represent discrete events. The variable x represents the value of a random process such as a noise voltage or current. It is assumed that each x defines a point on a straight vertical line corresponding to the distance from a fixed reference point. The distance x from the reference point might represent the value of the noise voltage or noise current. Dividing the line into small segments of length Δx and counting the number of times that x falls within each interval. The probability density function is then defined as:

$$p(x) = \lim_{\substack{\Delta x \rightarrow 0 \\ N \rightarrow \infty}} \frac{(\text{number of values within } \Delta x \text{ at } x) / \Delta x}{\text{total number of values} = N} \quad (4.1)$$

Thus $p(x)$ expresses probability as a density rather than discrete values, and is more appropriate for continuous functions of time as is noise in a radar receiver. The Gaussian PDF or the normal distribution [52] is important in detection theory[53] since it describes many sources of noise, including receiver thermal noise. In addition, it is more convenient to manipulate mathematically than many other PDF. The Gaussian PDF has a bell-shaped appearance, which is shown in Figure 4.2, and is given by:

$$p(x) = \frac{1}{\sqrt{2\pi\sigma^2}} \exp\left[-\frac{(x-\mu)^2}{2\sigma^2}\right] \quad (4.2)$$

where μ is the mean value of variable, σ is the standard deviation.

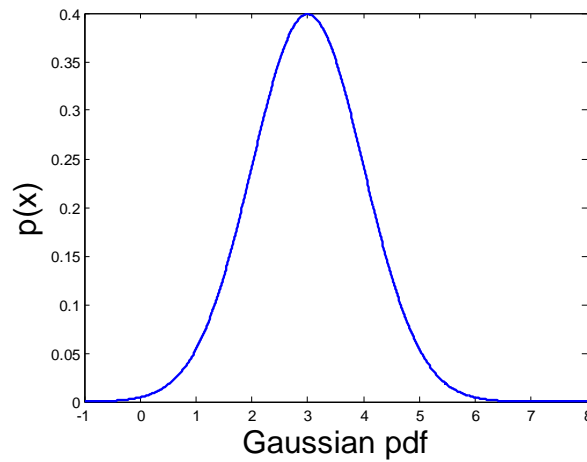
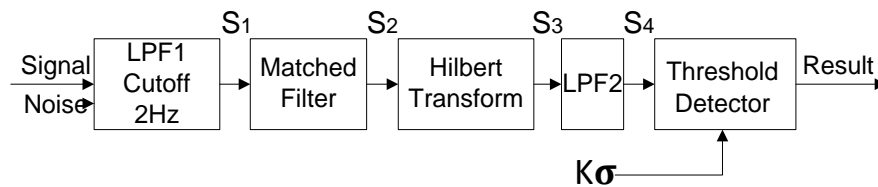


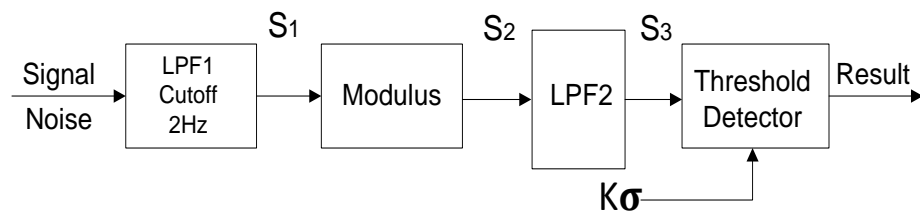
Figure 4.2 Gaussian PDF

At the same time, when we only detect the clutter or noise in the detection system, we will choose the proportional value to the standard deviation of the noise as the threshold level, so any detection will be determined as a false alarm[54] since there is no target. Before we start to process the recorded signal we need preprocess some modelling signal, which is generated by the PC, and then deal with the real recorded sample signal.

Figure 4.3 shows the comparison of two detection blocks. The first Low Pass Filter (LPF) in the four blocks is the same which are the second order butterworth low pass filter with the cutoff frequency of 2Hz[55]. The thresholds are all set as the $K \times \sigma$, where σ is the standard deviation of the output of only noise passing through the first Low Pass Filter (LPF).



(a)



(b)

Figure 4.3 Signal Processing block diagram (a) Ideal coherent detector with matched filter (MF) (b) Non-coherent detector

The noise, as the input signal without target, is the White Gaussian Noise (WGN) having the random interfering feature with Standard Deviation (STD) of 1 and mean value 0, shown in Figure 4.4.

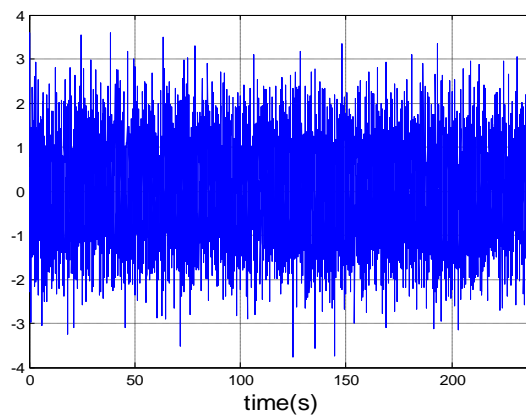


Figure 4.4 Additive White Gaussian noise $N(t)$

The PSD of the white Gaussian noise is shown in Figure 4.5. It is uniformly distributed in the frequency domain.

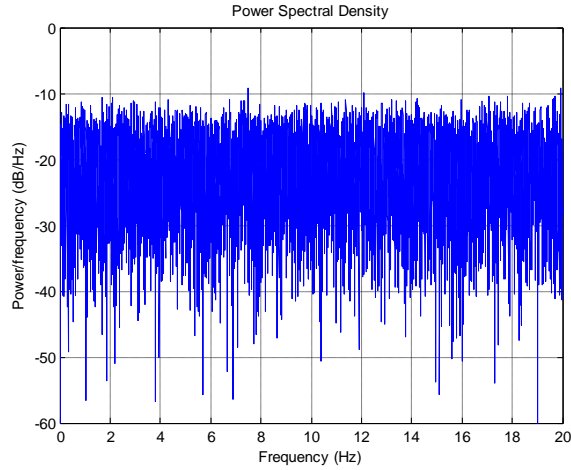


Figure 4.5 The PSD of the white Gaussian noise

After the I/Q demodulation, the distribution of WGN is Rayleigh distribution and described in the equation (4.3). The probability of detection of a target in the case of the only noise is considered as a false alarm.

$$p(x) = \frac{U(x)}{\sigma} \exp\left(-\frac{U(x)^2}{2\sigma^2}\right) \quad (4.3)$$

Where $p(x)$ is the probability of noise over the threshold level,

$U(x)$ is the envelope of the S_2 in Fig.4.3(b),

x is the variable values,

σ is the standard deviation value of the noise,

In Figure 4.6, the blue curve indicates the equation (4.3) calculation result for the detection system, and the red curve is the modelling result using the MonteCarlo simulation procedure, and clearly the modelling result fits with the ideal calculation result.

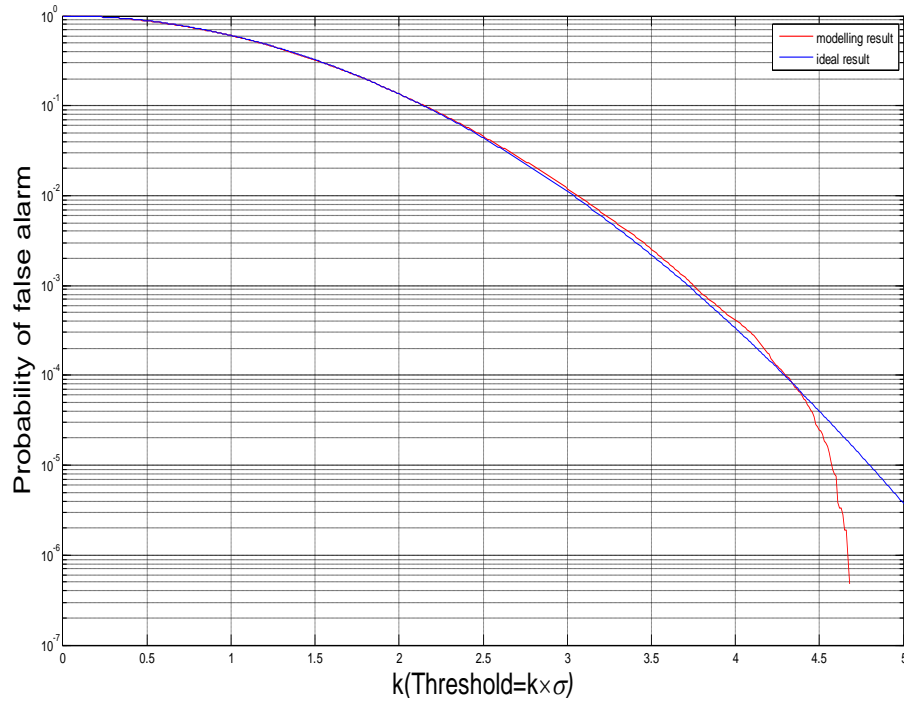


Figure 4.6 Comparison of the modelling and analytical result

The probability of detection P_D is defined in the equation (4.4)[49], then the relationship between P_D versus the SNR is plot in Figure 4.7. The P_{fa} ranges are chosen from 10^{-2} to 10^{-7} . In order to evaluate the performance of the signal processing block diagram, the MonteCarlo simulation result was compared with the equation calculation result at the $P_{fa}=10^{-3}$ shown in Figure 4.8. It is shown that the two curves fit very well at the acceptable tolerant level, and the difference is mainly determined by the Monte Carlo repeatable number. Due to the computation limitation, the simulation number cannot be set to be infinite.

$$P_D = \int_{V_T}^{\infty} \frac{r}{\sigma^2} I_0 \left(\frac{rU}{\sigma^2} \right) \exp \left(-\frac{r^2 + U^2}{2\sigma^2} \right) dr \quad (4.4)$$

Where I_0 is modified Bessel function 0 order.

U is the test signal amplitude,

V_T is the threshold value.

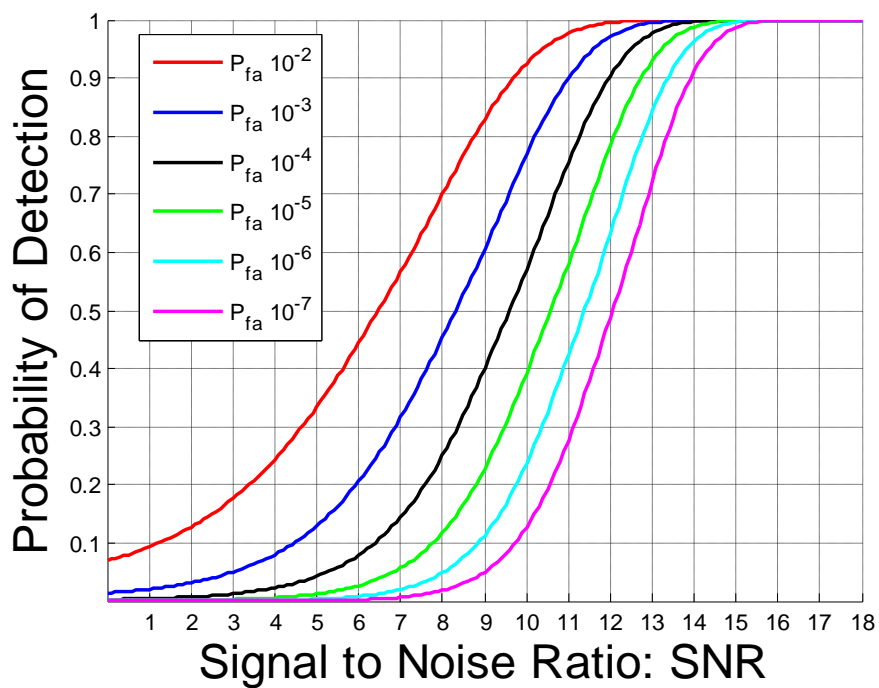


Figure 4.7 The P_D versus SNR

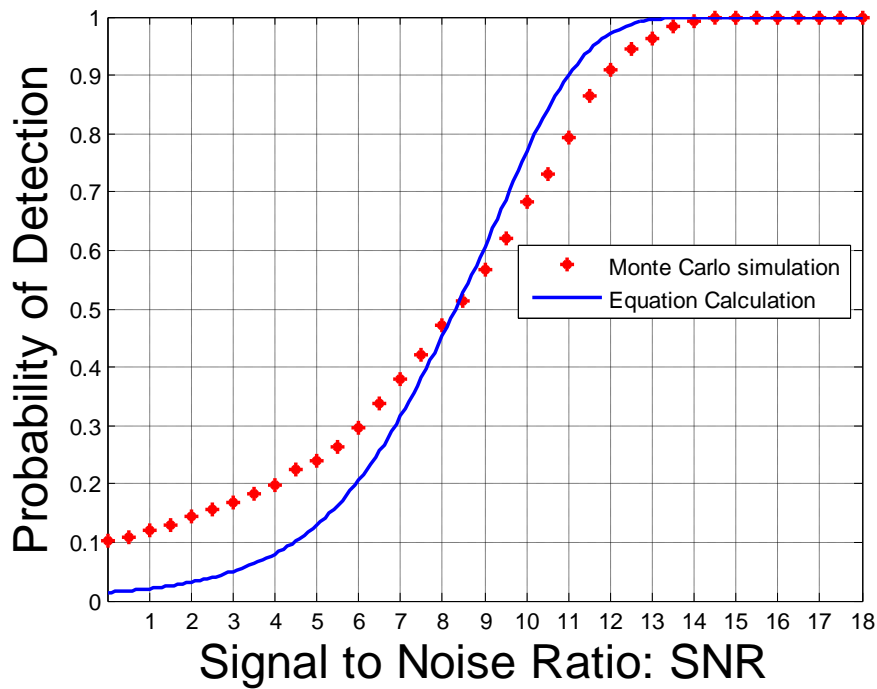


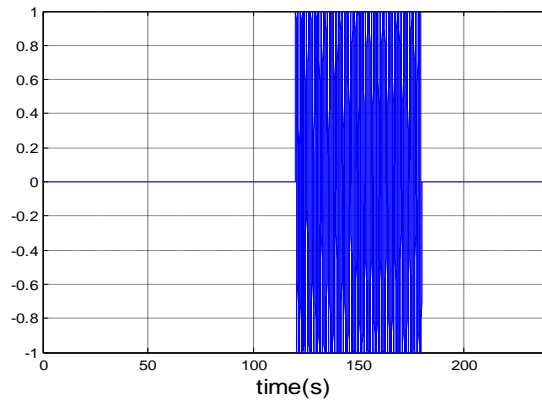
Figure 4.8 Comparison of the P_d vs SNR at $P_{fa}=10^{-3}$

4.2.1 Modelling signature

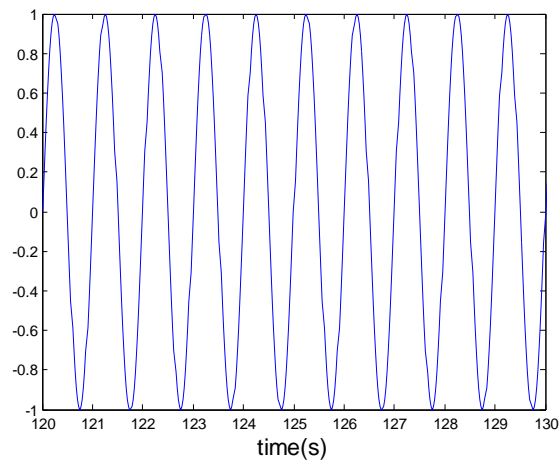
The modelling target signal is truncated cosine waveform, given in the equation (4.5). Figure 4.9 shows the truncated signal with total duration 240 seconds and target duration 60 seconds.

$$U(t) = U_0 \sin(2f_0\pi t) \quad (4.5)$$

where signal frequency $f_0=1\text{Hz}$, amplitude $U_0=1$. The sample frequency $f_s=40\text{Hz}$,



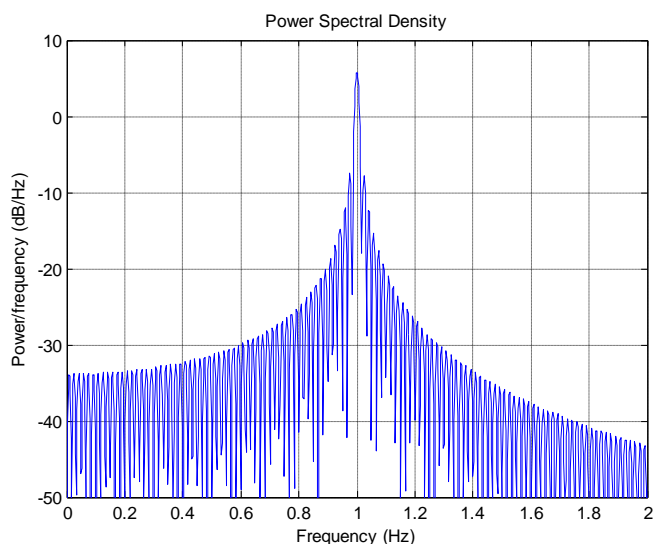
(a)



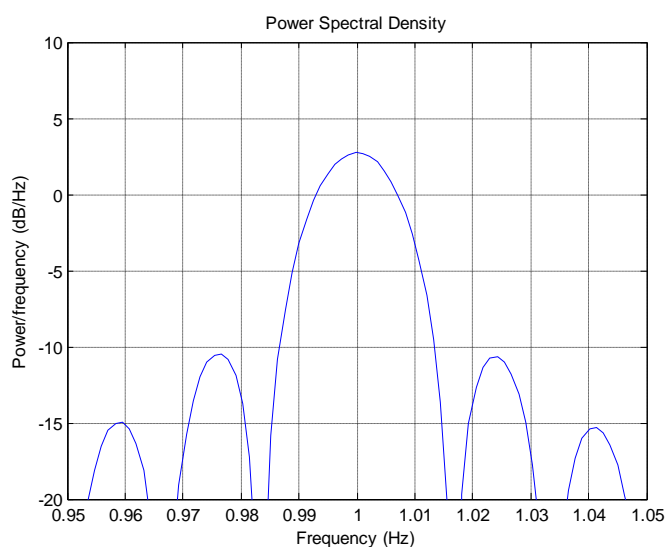
(b)

Figure 4.9 Input modelling signal $U(t)$ -truncated sine waveform(a)Total signal truncated signal: $U(t)$ (b)Time period from 120 to 130 seconds

Then we can get the Power Spectral Density (PSD) of the modelling truncated sine waveform shown in Figure 4.10(a). The peak main lobe of the signal is at 1Hz while the magnification details are shown in Figure 4.10(b). The amplitude range of the target signal is from -1 to 1V and can be adjusted when generating the desired combination of the signal and noise with specific SNR.



(a)



(b)

Figure 4.10 Power Spectral Density (PSD) of modelling signal (a) Total frequency range to 2Hz (b) Magnification of main lobe

If the noise alone passes through the LPF1 with cut off frequency 2Hz, and get the standard deviation σ . Utilizing the equation (4.6) to define the SNR, we can get the waveform of S_1 with SNR 15dB which is the combination of signal and noise after passing through the first LPF shown in Figure 4.11.

$$SNR = 10 \times \log_{10} \frac{U_0^2}{2\sigma^2} \quad (4.6)$$

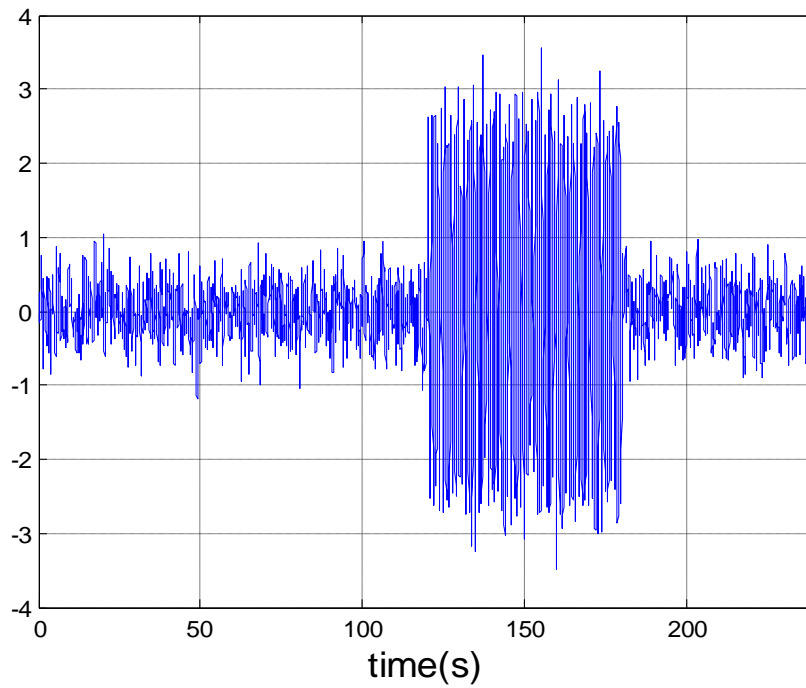


Figure 4.11 Output of first low pass filter - S_1

Figure 4.12 illustrates the signal recorded using the FSR system when a target walks cross the baseline. The total time of the record is 300 seconds and the target movement time is around 60 seconds.

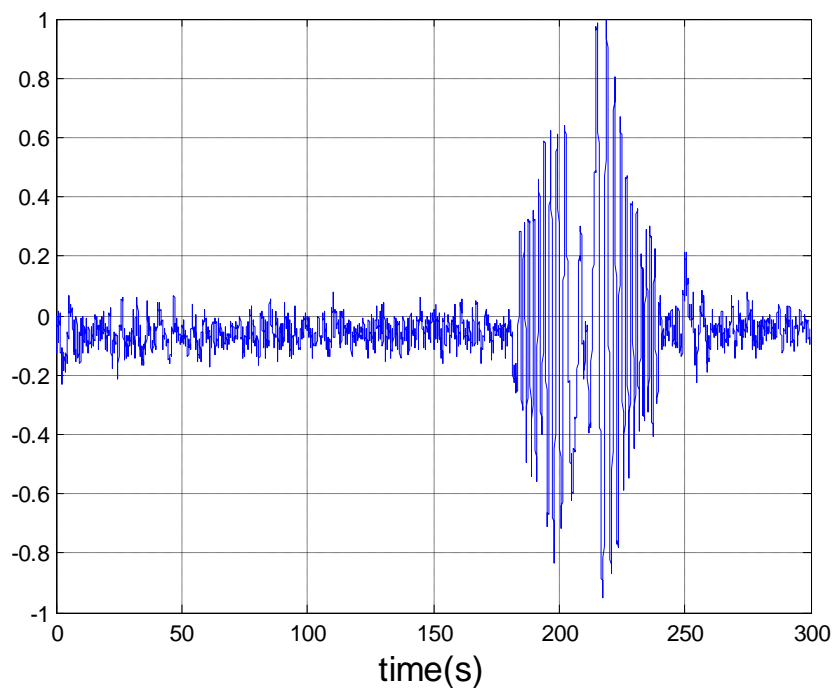


Figure 4.12 Signal wave form received from the RX

The real recorded signal from the experiment is shown in Figure 4.12, and the target signal is truncated manually and reshaped with white Gauss noise.

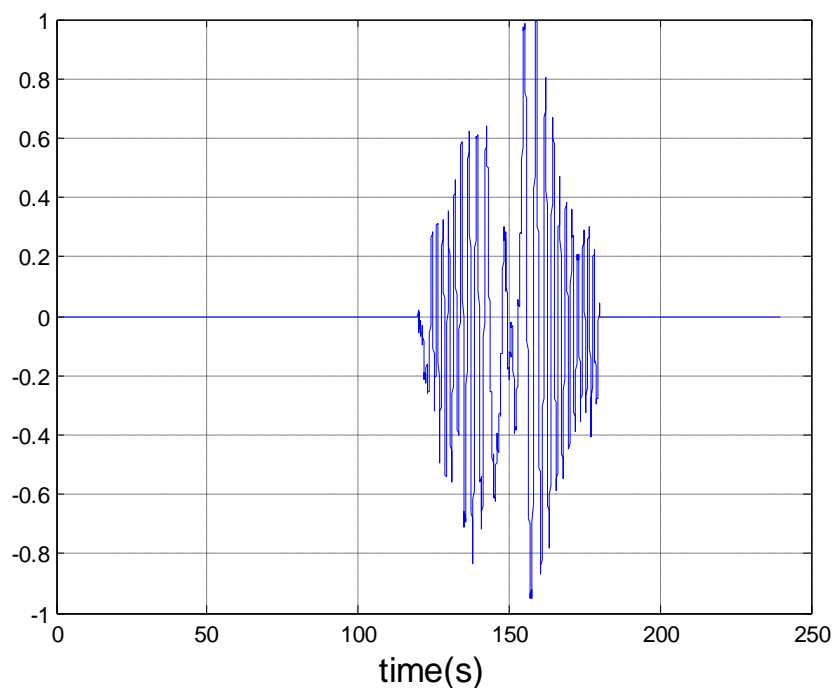


Figure 4.13 Truncated target signature

Then we add the white Gaussian noise and pure recorded signal together for the comparison to the modelling signal. The combination of the two signals with noise is shown in Figure 4.14 . The SNR level is set to be 15dB as the power of the noise estimated after passing through LPF1.

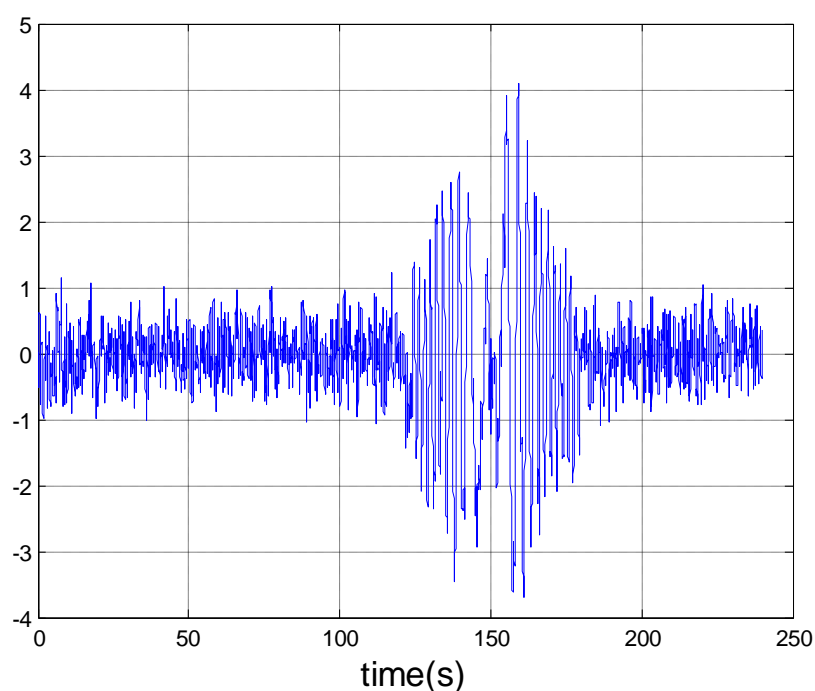
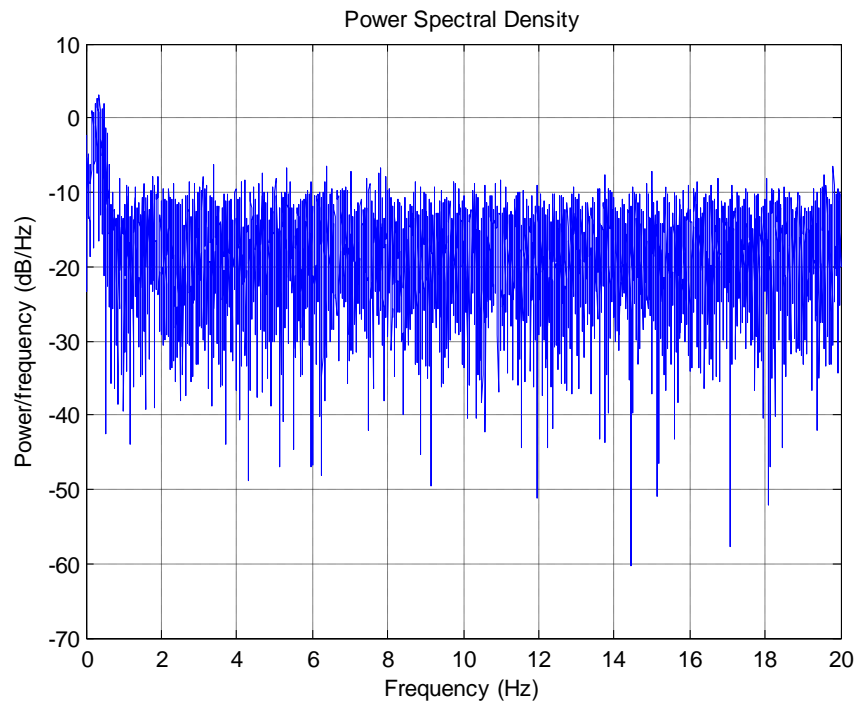
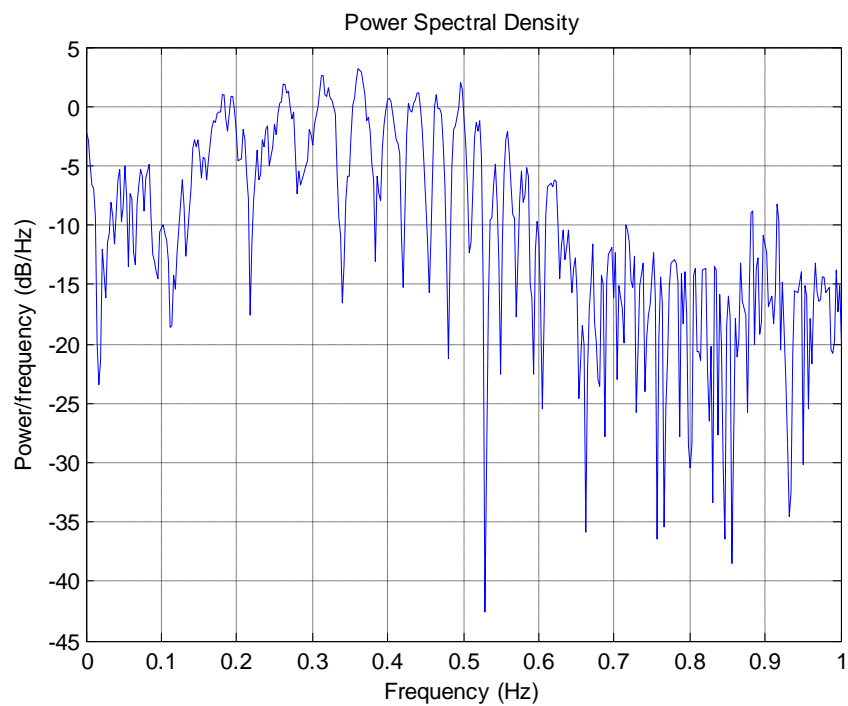


Figure 4.14 Modelling signature with target signal and white Gauss noise

The PSD of the artificial signal, which is the recorded signal combined with WGN is calculated and shown in Figure 4.15. We can see that the main lobe of the PSD is within the 2Hz and the magnification is shown in the Figure 4.15(b) in detail. The main power of the recorded signal distributes from 0.2 to 0.6Hz.



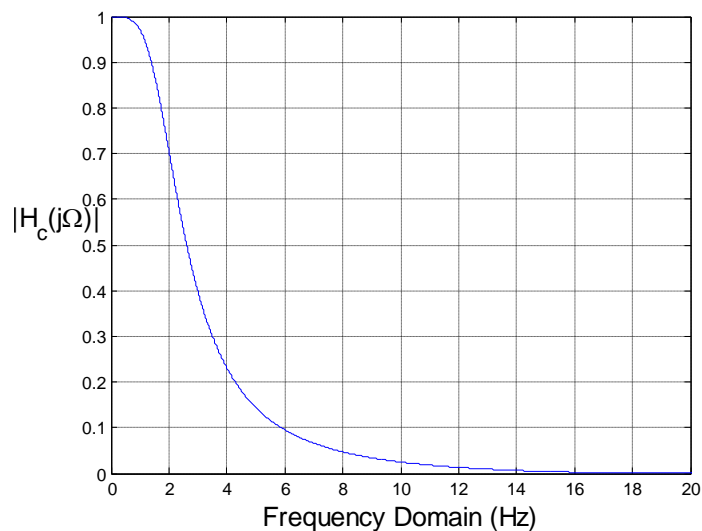
(a)



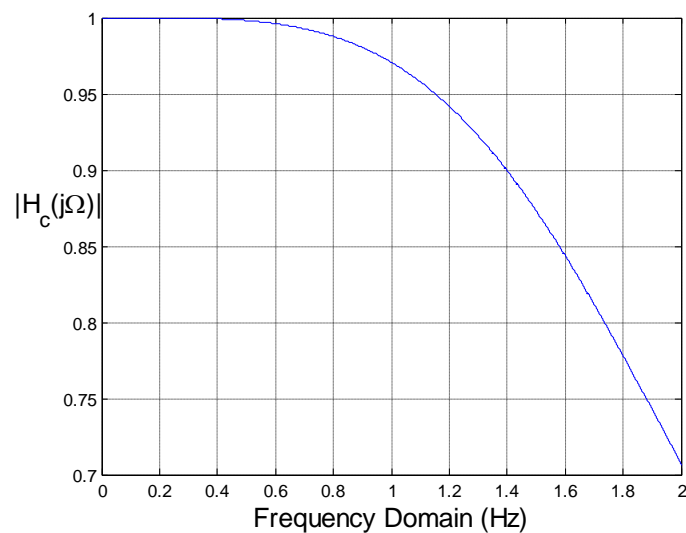
(b)

Figure 4.15 PSD of the modelling signature (a) PSD within full frequency range (b) Magnification in details

In Figure 4.16, the frequency response of LPF1 is illustrated. The first low pass filter's cutoff frequency is 2Hz while the frequency response magnitude is 0.707 which equal to $2^{-\frac{1}{2}}$.



(a)



(b)

Figure 4.16 The frequency response of the first LPF with cut off frequency 2Hz (a) Full frequency range (b) Magnification in details within 2Hz

4.2.2 Coherent detection

A signal is named the coherent waveform if its phase is a determinate function of time[3]. The ideal coherent detector block diagram is shown in Figure 4.3(a); it mainly applies the matched filter as the detector and Hilbert transform as the envelope generator. Under some certain conditions, maximizing the output power ratio of a radar receiver maximizes the detection ability of a target. A linear network that does this is called a matched filter. Thus a matched filter, or a close approximation to it, is the basis for the design of almost all radar receivers. The matched filter that maximizes the SNR when the input noise spectral density is uniform (white noise) has a frequency response function:

$$H(f) = G_a S^*(f) \exp(-j2\pi f t_m) \quad (4.7)$$

where G_a is a constant, t_m is the time at which the output of the matched filter reaches the maximum, and $S^*(f)$ is the complex conjugate of the spectrum of the (received) input signal $s(t)$, found from the Fourier transform of the received signal $s(t)$ such that:

$$S(f) = \int_{-\infty}^{\infty} s(t) \exp(-j2\pi ft) dt \quad (4.8)$$

The received signal spectrum can be written as:

$$S(f) = |S(f)| \exp[-j\phi_s(f)] \quad (4.9)$$

Where $|S(f)|$ is the amplitude, $\phi_s(f)$ is the phase. Similarly, the matched filter frequency-response function can be expressed in terms of an amplitude and phase as:

$$H(f) = |H(f)| \exp[-j\phi_m(f)] \quad (4.10)$$

Letting the constant G_a equal unity, we can use these relations to write equation (4.7)

as

$$|H(f)|\exp[-j\phi_m(f)] = |S(f)|\exp\{j[\phi_s(f) - 2\pi ft_m]\} \quad (4.11)$$

Equating the amplitudes and phases in the above gives

$$|H(f)| = |S(f)| \quad (4.12)$$

and

$$\phi_m(f) = -\phi_s(f) + 2\pi ft_m \quad (4.13)$$

It is seen that the magnitude of the matched filter frequency response function is the same as the amplitude spectrum of the input signal, and the phase of the matched filter frequency response is the negative of the phase spectrum of the signal plus a phase shift proportional to frequency. The effect of the negative sign before $\phi_s(f)$ is to cancel the phase components of the received signal so that all frequency components at the output of the filter are of the same phase and add coherently to maximize the signal. The matched filter processing block is shown in Figure 4.17.

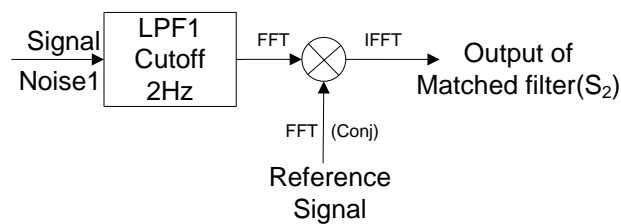


Figure 4.17The matched filter processing block

In Figure 4.17, the complex conjugate of reference signal times the output of the combination signal and WGN passing through the LPF1. Then we can get the inverse FFT of the multiply result which is the matched filter output. The reference signal is the cosine rectangular shape starting at 0 second and lasting 60 seconds shown in the Figure 4.18.

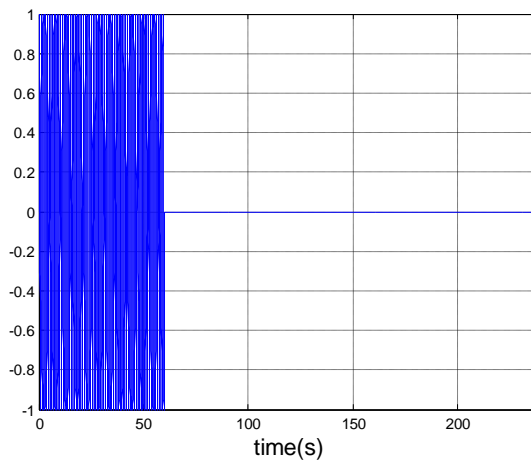


Figure 4.18 Rectangular shape cosine reference function

Utilizing the matched filter processing block in Figure 4.17 to the modelling cosine signal, we can get the output of the matched filter shown in Figure 4.19.

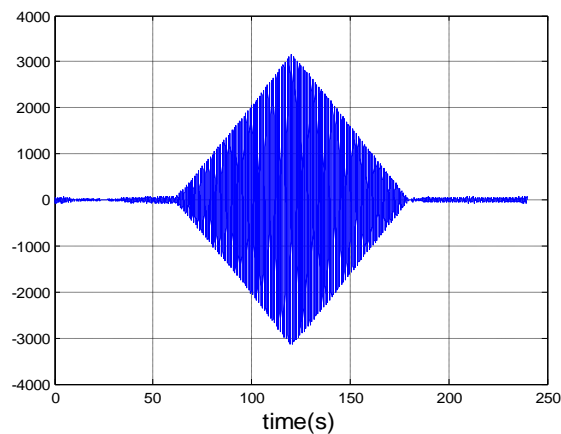


Figure 4.19 The output of the matched filter

The Hilbert transform in the coherent detection block will generate the envelope of the output of matched filter- S_2 which is illustrated in Figure 4.20. The triangular shape of the envelope represents the envelope of absolute value of the signature.

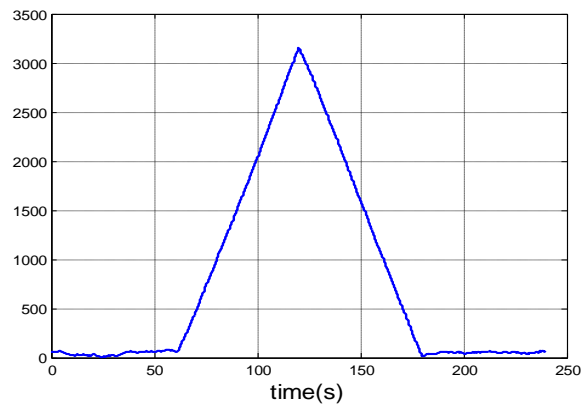
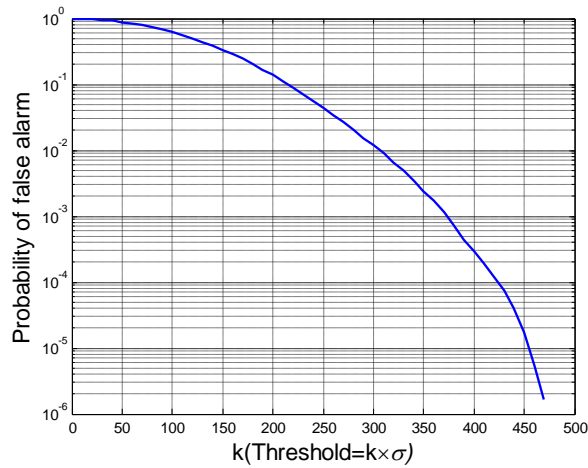
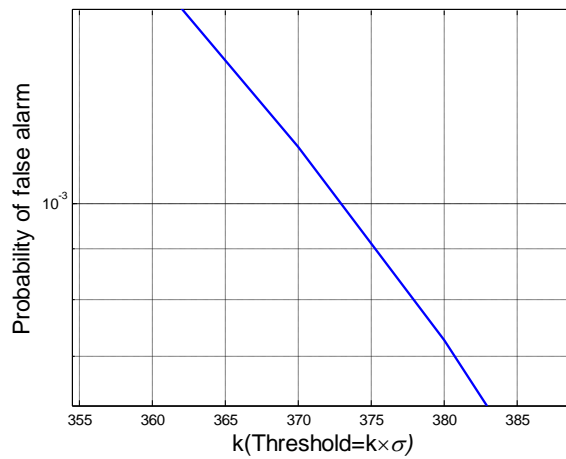


Figure 4.20The output of Hilbert Transform

After we obtain the one single envelope of the signal and noise, we can state that the matched filter will greatly increase the SNR level. If the amplitude of the input signal is 0, or there is no target showing, the noise is the only input from receiver. Then, a group of the threshold values are set from 0 to 470 times the standard deviation of the pure noise passing through LPF1 with step 10 to build the threshold detector. In addition, the total number of noise intervals is set to be 1000. Any detection in these intervals is regarded as a false alarm. Finally, the value of P_{fa} corresponding to the threshold is shown in Figure 4.21.



(a)

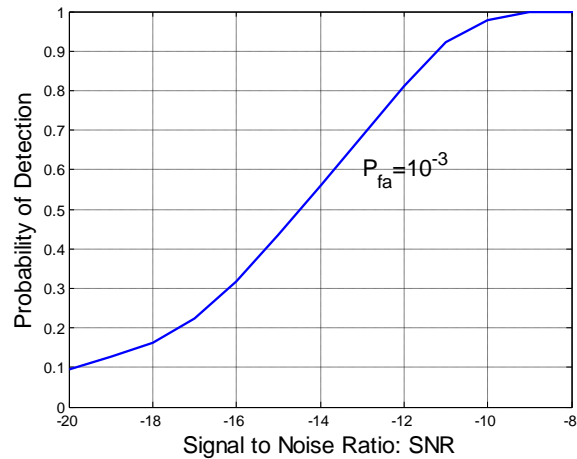


(b)

Figure 4.21The relationship between the P_{fa} and threshold (a) Full range of threshold to 470

(b) the magnification figure when the $P_{fa}=10^{-3}$

According to Figure 4.21(b), the corresponding threshold level factor for $P_{fa}=10^{-3}$ is 372.5. In this case, the threshold must be set at 372.5 times the noise power. Then we apply the rectangular shape signal together with the WGN as the input signal, using the coherent detection block in Figure 4.3 to get the P_D versus SNR shown in Figure 4.22 (a).



(a)

(b)

Figure 4.22 The relationship between the P_d and SNR(dB) at $P_{fa}=10^{-3}$

We have already processed the modelling rectangular shape signal; when the recorded signal is applied in the same procedure, we will have the reference signal shown in Figure 4.23.

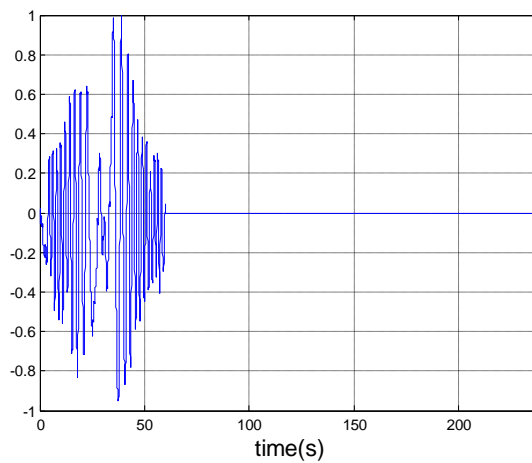


Figure 4.23 Reference signal for recorded signal

Then we can get the output of the matched filter S_2 shown in Figure 4.24 when we utilize the recorded signal and the white Gaussian noise with SNR=15.

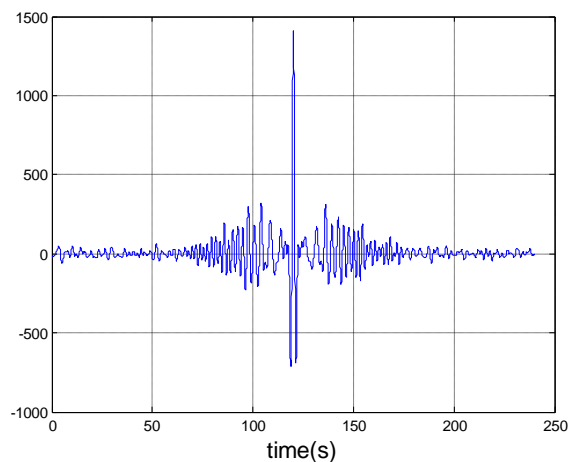


Figure 4.24The output of the matched filter S_2

Then we utilize the Hilbert transform to get the envelope of the S_2 . We can get the modulus value of the waveform illustrated in Figure 4.25.

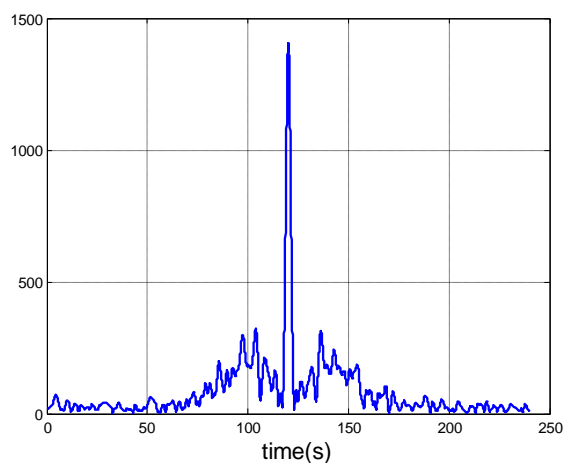


Figure 4.25 The output of Hilbert Transform S_3

Then we can get the P_{fa} versus threshold levels shown in Figure 4.26.

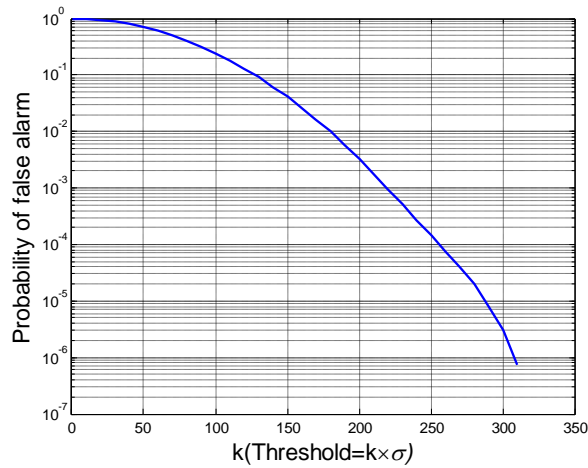


Figure 4.26 The P_{fa} versus threshold K level

Then we add the recorded signal with the white Gaussian noise as the input signal, using the coherent detection block to process the combined input signal.

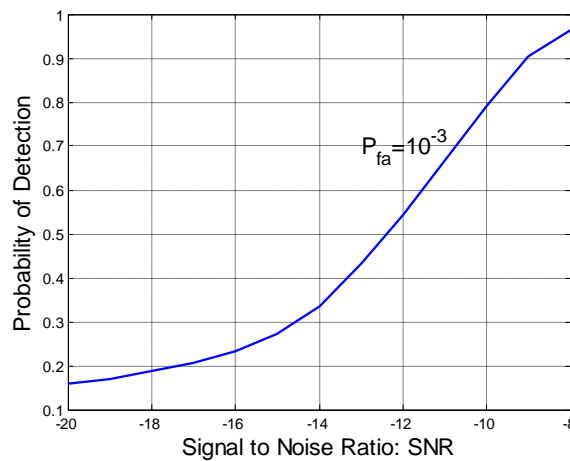


Figure 4.27 The relationship between the P_d and SNR at $P_{fa}=10^{-3}$

After combining Figure 4.22 and Figure 4.27, the comparison between the two curves are made and shown in Figure 4.28, and we will find that in the coherent detection result, the modelling signal and the recorded signal has nearly 2dB shift when the $P_d=80\%$, while the non-coherent detection has no more than 1dB shift. However, there is nearly a 7 to 8 dB difference between the coherent and non-coherent case. Therefore, we still need to find new non-coherent detection block to decrease the difference.

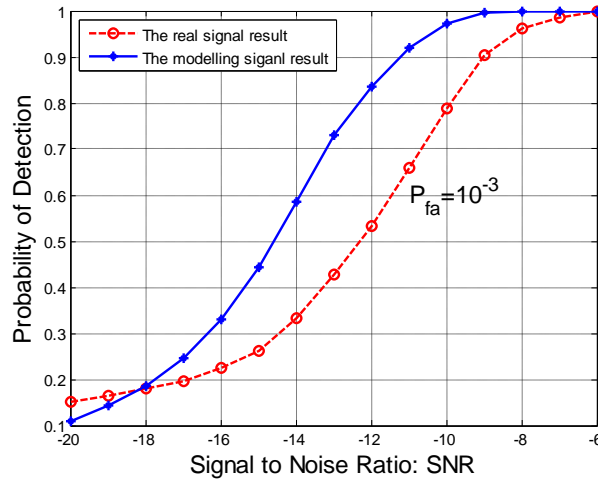


Figure 4.28 The comparison of P_d versus SNR for the modelling signal and recorded signal

4.2.3 Non-coherent detection

In the previous section, we introduced the coherent detection block diagram for both the modelling rectangular and recorded signal. Non-coherent detection previous modulation techniques were all been based on coherent detection schemes. That is the receiver “knows” the carrier phase of the input signal. In a non-coherent receiver, no assumption of the carrier phase is made by the receiver. While the radar receiver is possible without knowing the carrier phase, it will be shown in this section that there is a sizeable penalty in the time duration of the input signal. The second LPF cut off frequency is set to be $1/T_s$, where T_s is the truncated signal duration: 60 seconds. The wave form S_3 is shown in Figure 4.29.

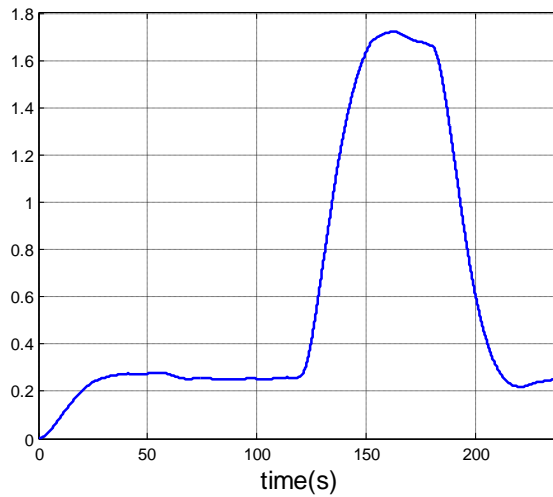


Figure 4.29 Wave form of S_3

The P_{fa} versus threshold for the non-coherent detection block diagram is performed and is shown in Figure. The threshold level for P_{fa} at the 10^{-3} is chosen for the P_D versus the SNR level.

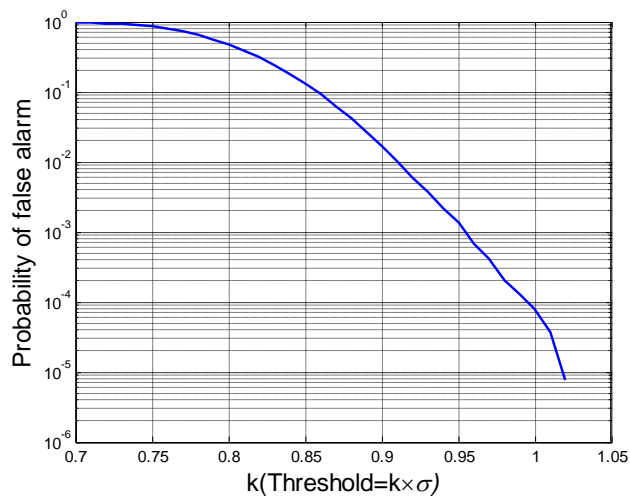


Figure 4.30 The relationship between the P_{fa} and Threshold

Once again, Figure 4.31 shows the P_D versus SNR at the P_{fa} level of 10^{-3} for the modelling signal. It is shown that the P_D is far more less than the coherent detection processing block, and that is the reason we chose the coherent detection as the main target detection method. After processing the real recorded signal by utilizing the same non-

coherent detection, we compare the 4 curves of the P_D versus SNR in one graph and this is shown in Figure 4.32.

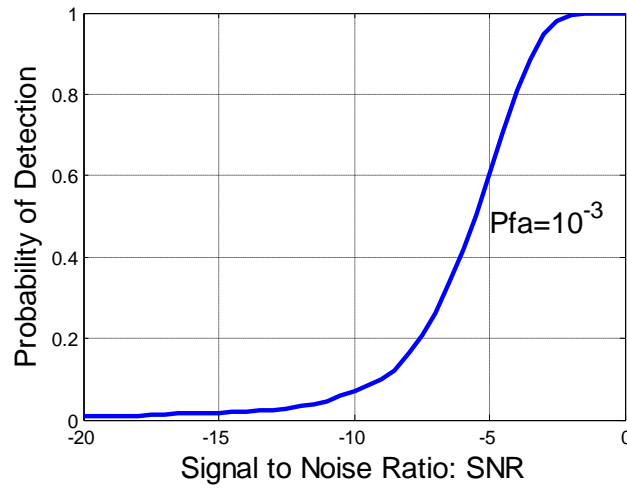


Figure 4.31 The relationship between the P_{fa} and SNR at $P_{fa}=10^{-3}$

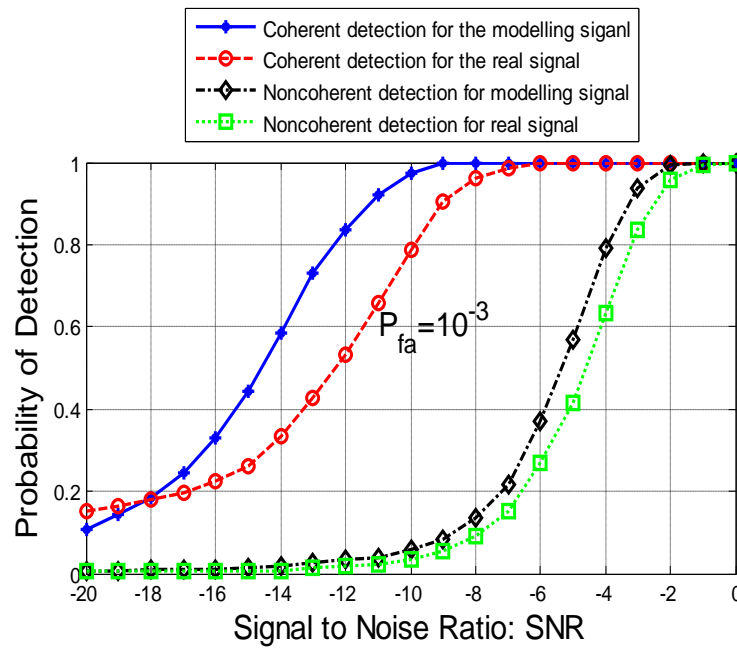


Figure 4.32 Comparison of coherent and non-coherent detection for the modelling and recorded signal

From Figure 4.32, it is concluded that the coherent detection is more effective than the non-coherent detection. Using the same test signal modelling rectangular waveform for

example, to achieve the same $P_D=80\%$, the coherent detection in blue has less SNR 8dB than the non-coherent detection in black. Within the same detection block diagram, the modelling signal gives a better P_D result than the real recorded signal, at the same P_D level of 80%, the SNR level has nearly 2dB increasing ratio. While for the non-coherent detection, it has no more than 1dB increasing between the modelling and real recorded signal.

4.2.4 Investigation on LPF1's cut off frequency

From the previous section, the main lobe of PSD for the recorded target signal is within the vicinity of 0.5Hz, shown in Figure 4.15(b). In order to find the optimum cut off frequency (f_{c1}) of the LPF1 in the non-coherent detection, f_{c1} is set from 0.2Hz to 1.8Hz with the step of 0.4Hz. The LPF2's cutoff frequency is set to be $1.8/T_S$ (Hz), where T_S is the truncated signal duration: 60 seconds. We utilize the standard deviation of S_1 which is the output of LPF1 to set the threshold and calculate the SNR.

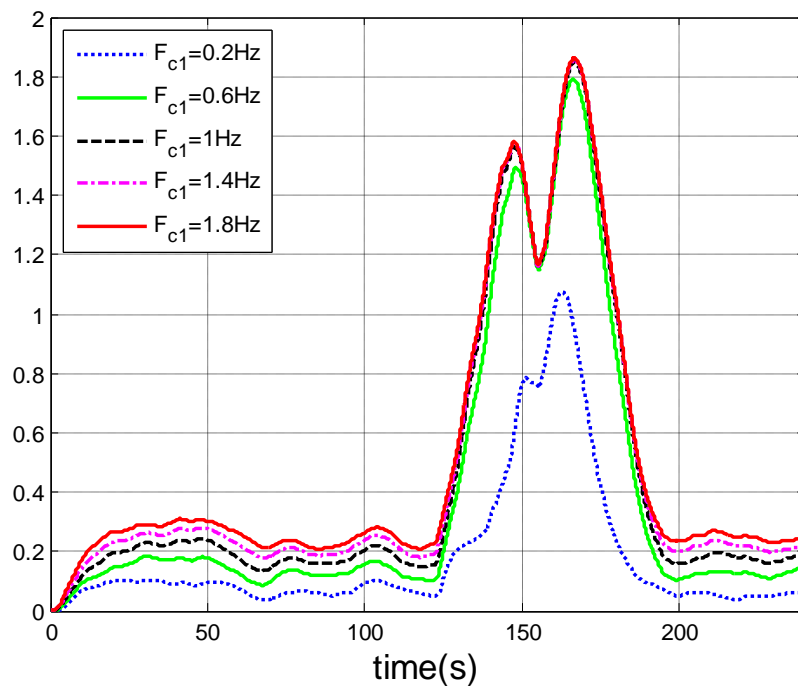


Figure 4.33 The output of the LPF2 after passing through the filter banks

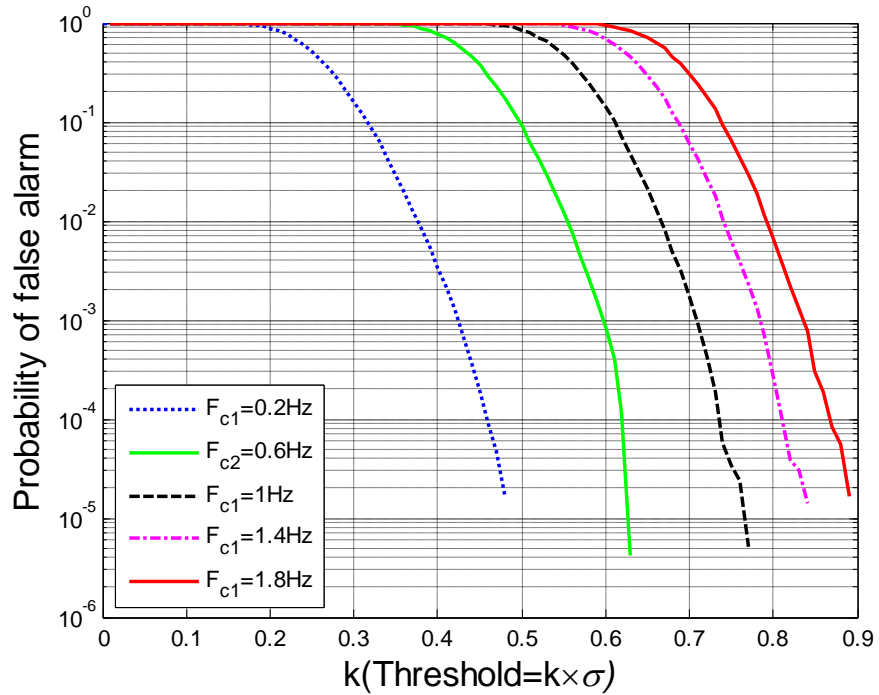


Figure 4.34 The relationship between the P_{fa} and threshold at varies LPF1

Using the Monte Carlo procedure in the non-coherent detection, we can get the relationship between P_D and the SNR in Figure 4.35.

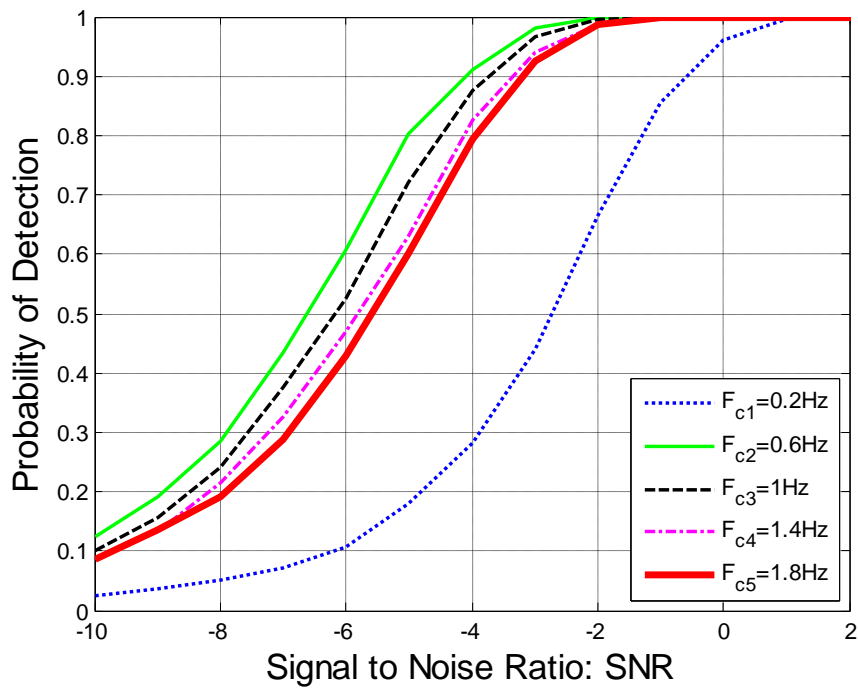


Figure 4.35 Relationship between the P_d and SNR at $P_{fa}=10^{-3}$.

From Figure 4.35 we can clearly find out that when the LPF1's cut off frequency is set to be 0.6Hz we will get the highest probability of detection at the same signal to noise ratio. The lower or higher cut off frequency of first low pass filter will decrease the probability of detection. The relationship between the P_d and the first low pass filter cut off frequency at the varies Signal to Noise Ratio is shown in Figure 4.36. Similarly, the P_D will reach the maximum at the 0.6Hz for the SNR range -6 to -2dB.

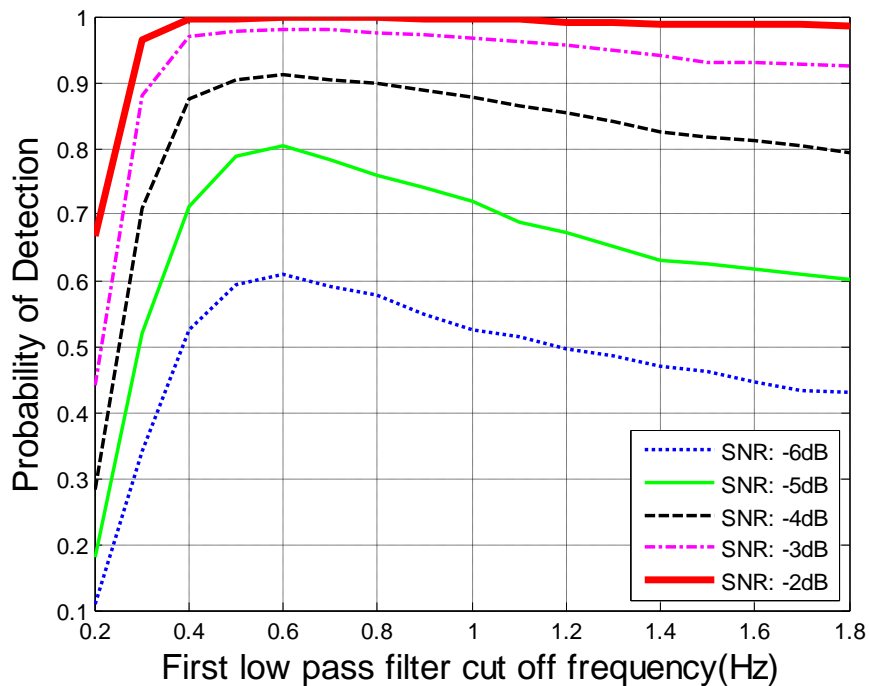


Figure 4.36 The relationship between the P_{fa} and LPF1's cut off frequency at different SNR

4.3 *Short-time Fourier transform of the recorded target signature*

In this section, the Short-Time Fourier Transform (STFT) is applied in the real recorded signature. The short time Fourier transform (STFT) can be described mathematically in the continuous time domain by:

$$STFT(t, \omega) = \int_{-\infty}^{\infty} s(\tau) \omega^*(\tau - t) e^{-j\omega\tau} d\tau = \int_{-\infty}^{\infty} s(\tau) \omega_{t,\omega}^*(\tau) d\tau \quad (4.14)$$

Where the $s(t)$ is the signal and $\omega(t)$ is the window function

While the discrete time format of the STFT can be displayed as followed:

$$STFT(n, k) = \sum_{m=n}^{N-1+n} \omega(m-n) s(m) e^{-j\omega_k(m-n)} \quad (4.15)$$

The main idea of the STFT is to perform the Fourier transform block by block of the signal in the time domain rather than process the long time signal at once. Therefore, each block of the FT result stands for the time point frequency domain amplitude which can not only be reflected in the time domain, but also can be seen in the frequency domain.

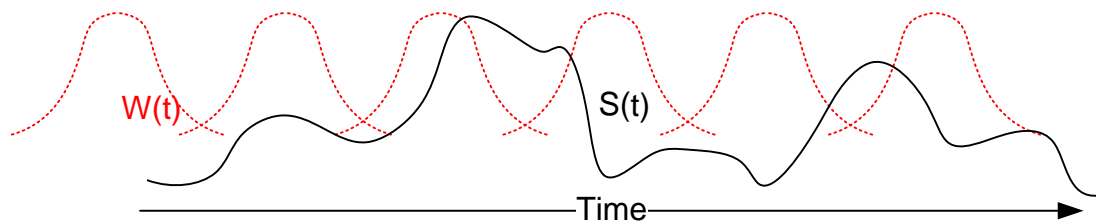
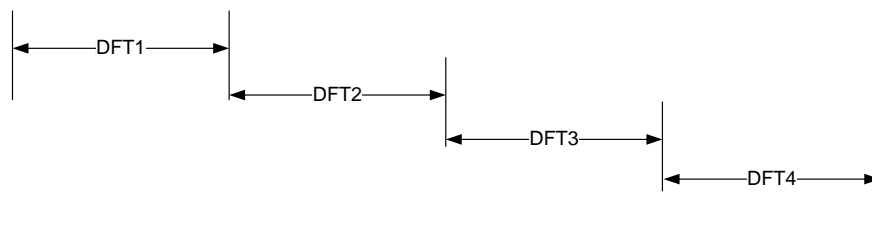
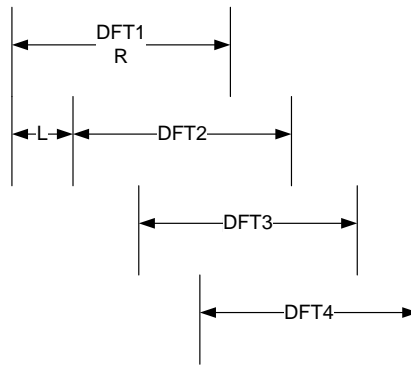


Figure 4.37 Short time Fourier transform indication in time domain



(a)



(b)

Figure 4.38 DFT segments overlapping (a) without overlap (b) With R-L overlap

In order to extract the main target signature when it passing through the baseline, the rectangular window is added and plotted in Figure 4.39. The rectangular window length is determined by the short time FFT target length.

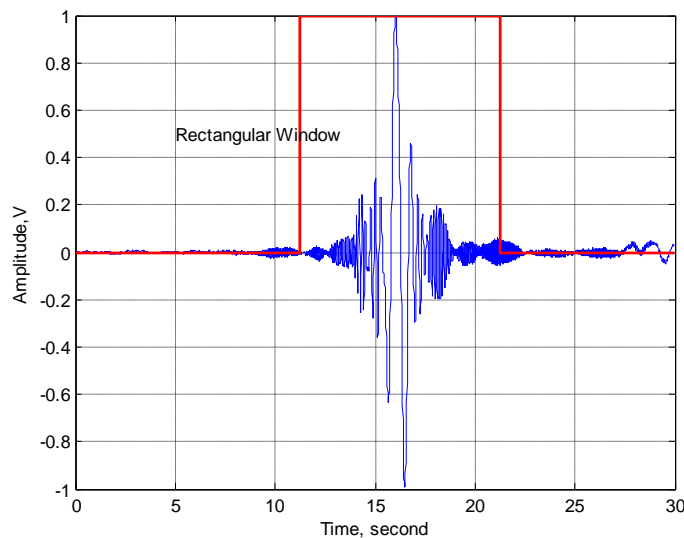


Figure 4.39 Rectangular window added in the recorded signal

In Figure 4.40, the yellow and red area, more than -10dB, shows the existence of the target[56].The window used in the STFT is 256 point symmetric Hamming window shown as followed. It determined the length of each block of the signal. After setting the time-

frequency domain power threshold level to be -10dB, the power below -10dB is set to be -10dB and the rest of area keeps the original colour. Finally, we can get the time frequency plot shown in Figure 4.40.

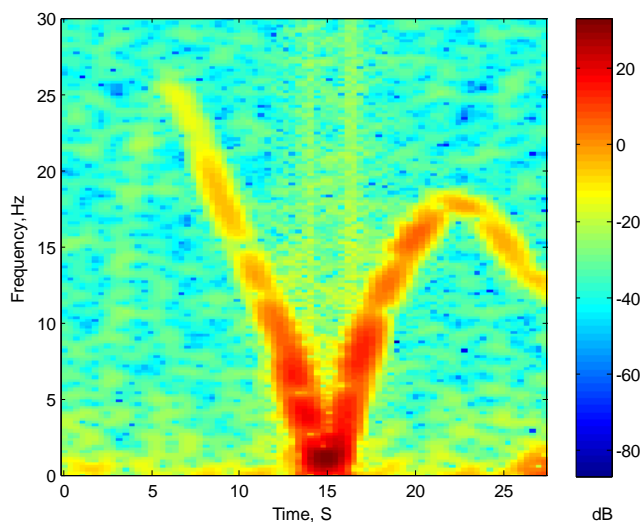


Figure 4.40 STFT of the recorded signal

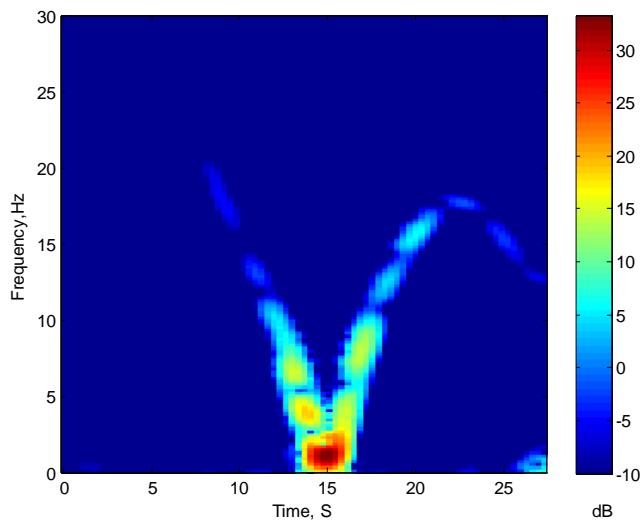


Figure 4.41 After setting the threshold power equal to -10dB

In some low SNR cases, the signal could be only vaguely identified from the emerged noise floor. For example, Figure 4.42 shows the target signature with low SNR level, and it is likely to be wrongly recognized as the noise floor.

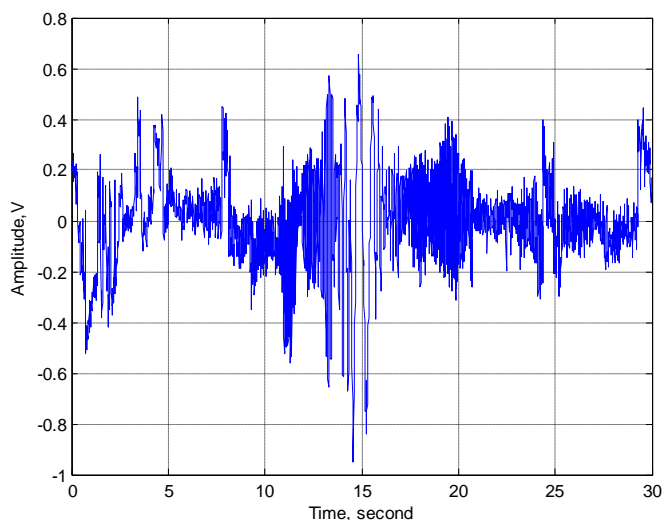


Figure 4.42 The time domain signature with low SNR

Figure 4.43 shows the STFT result for the time domain signature with the low SNR. The red 'V' shape image area clearly shows the present of target Landrover and the target is obviously isolated from the background noise.

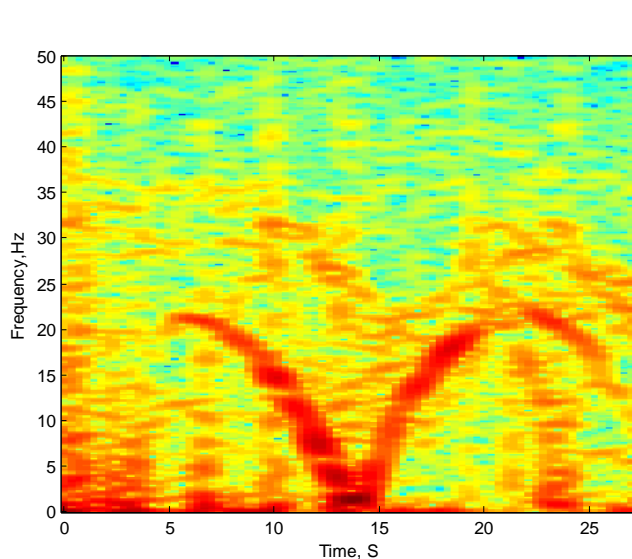


Figure 4.43 STFT result of the recorded signal

4.4 *Mathematical approach to Principal Component Analysis*

In the classification domain, we have to extract the main features of the target and set up the appropriate classifier. In this section, the Principle Component Analysis (PCA) is introduced to the reader for a better understanding of how the feature is extracted. Pearson [57] invented PCA and first applied by Hotelling[58] in the area of statistics study. Due to the outstanding performance in the large data dimension reduction, the PCA is widely utilized in the pattern recognition such as facial, number plate, movement recognition. The aim of the PCA is to summarize the features in a highlights way to the target data.

For a given set of data X, The PCA algorithm can be concluded as follows:

Identify the symbales

Step1: Calculate the mean value of the x_i

$$\mu = \frac{\sum_{i=1}^N x_i}{N} \quad (4.16)$$

Step2: Normalization the data to the mean value

$$N = (x_i - \mu) \quad (4.17)$$

Step3: Calculate the covariance matrix of X

$$M = \frac{\sum_{i=1}^N (x_i - \mu)(x_i - \mu)}{n-1} \quad (4.18)$$

Step4: Calculate the eigenvectors and eigen value

$$(M - \lambda I)e = 0 \quad (4.19)$$

where M is covariance matrix, λ is eigen value, I is the identity matrix,

Step5: Rearrange the eigenvectors in the descending order

$$W = (e_{\max}; \dots; e_{\min}) \quad (4.20)$$

Step6: Transform the data in the eigen value space

$$D = W^T \times N^T \quad (4.21)$$

The number of the Principal Components (PC) is hard to determine due to the variance of the data type and the dimension. It is practical to choose 80%-90% weight of PCs as the target feature. It is shown in [40] that the first 10 PCs can be retained for the database collected from the FSR system. In addition, there are many other methods for classification, such as artificial neural networks, deep learning methods and Bayesian classifier, which can be applied into our database and classify the ground targets.

4.5 *Conclusion*

In this chapter we have analyzed the ATD in the FSR system with the modelling signal and the recorded signals. The coherent and non-coherent detection block diagrams for the

target detection are provided. They are evaluated by the MonteCarlo simulation method. It is proved that the coherent detection block diagram will obtain the highest P_d at the same P_{fa} levels. Further all, the time frequency analysis shows that the short time wavelet transform can be utilized in the target detection algorithm for the further research. Finally, the PCA algorithm is briefly introduced for the further experimental result analysis. The sample matlab code is shown in Appendix D and more details are provided in the attached disc.

Chapter 5 Experimental evaluation and test result

5.1 *GFSR experiment description*

In this chapter the experimental evaluation for the GFSR system is presented and the preliminary processing result is shown. There are numbers of experiments that were conducted by the author and other research members during the PhD study period. The aims of those experiments were varied. Based on the complexity of the radio environment, the experiments can be classified into three main categories: the ideal open field with no vegetation surroundings; the medium density vegetation clutter environment; and the high density vegetation environment.

First, the ideal open field experiment was performed at Tilesford airfield, Worcestershire, United Kingdom. The test field is airplane tracks from World War II. No large vegetation and buildings existed within the test site. Only the grass covers the land outside of the tracks. The GFSR Rx/Tx system is deployed at 6 positions to investigate the robust signature when the devices are moved to other locations.

The second test site is located at Senneleys Park, Birmingham, UK. It can be categorized into medium complexity with some vegetation around the forward scatter zone and near the Rx/Tx devices. The parallel deployment was also conducted to investigate the potential interference caused by the obstacles; 3 positions are applied.

The third trial was implemented at Pritchatts car park, Birmingham, UK. This test site has larger vegetation surroundings and lower bushes in the middle of the baseline, which can be defined as complex radio environment for the GFSR system. The number of parallel placement is three.

5.2 Tilesford airfield trail

5.2.1 Location effect

The four channel and three channel frequency Rx/Tx systems are deployed at six different positions where the baselines of every placement are parallel with each other. The top view of the devices deployment is shown in Figure 5.1. The same Rx/Tx was placed in three positions on the concrete surface while another three groups were located on the grassland. All of the baselines are parallel with each other at a distance of 5m. The top view of the deployment from the Google map is shown in Figure 5.2 . The target used for this experiment was Landrover and the speed was predefined to be 9m/s, 13.499m/s and 18m/s at position 3. At the rest of the positions, the target speed is set to be 8.94m/s. The trajectory of the target is perpendicular to the baselines.

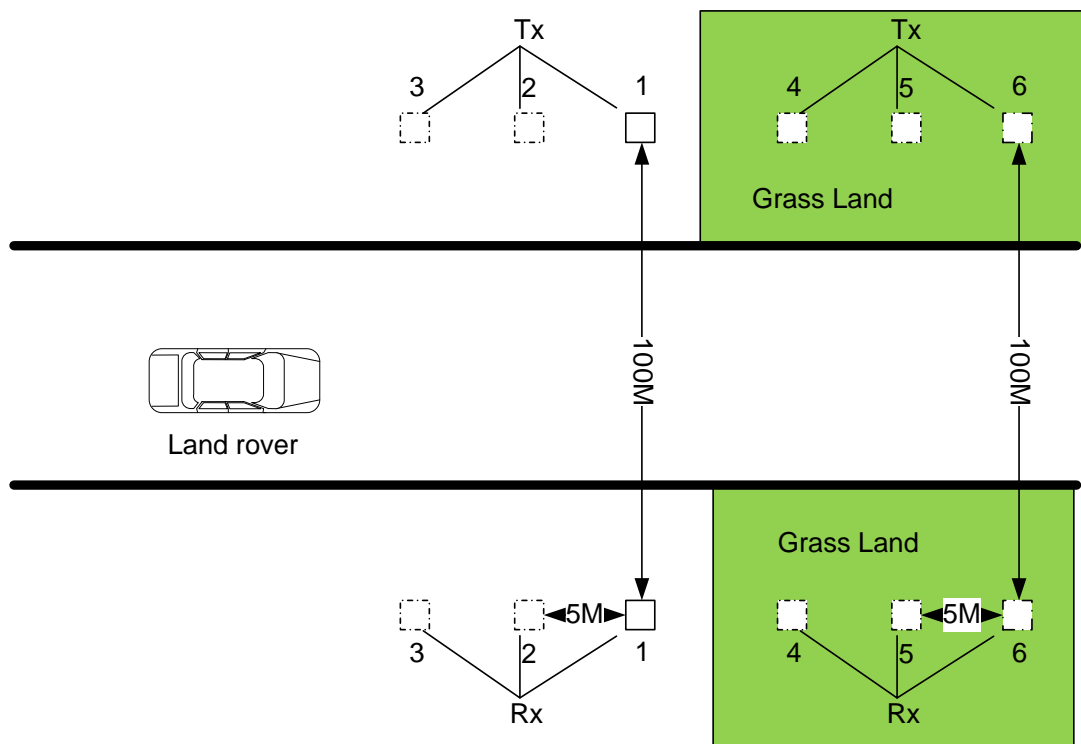
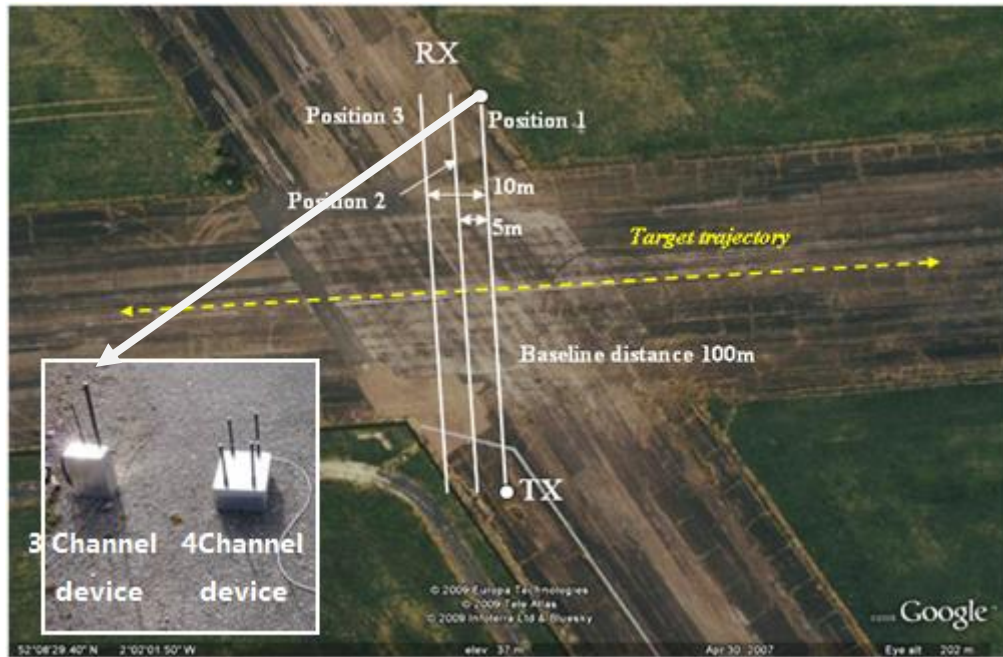
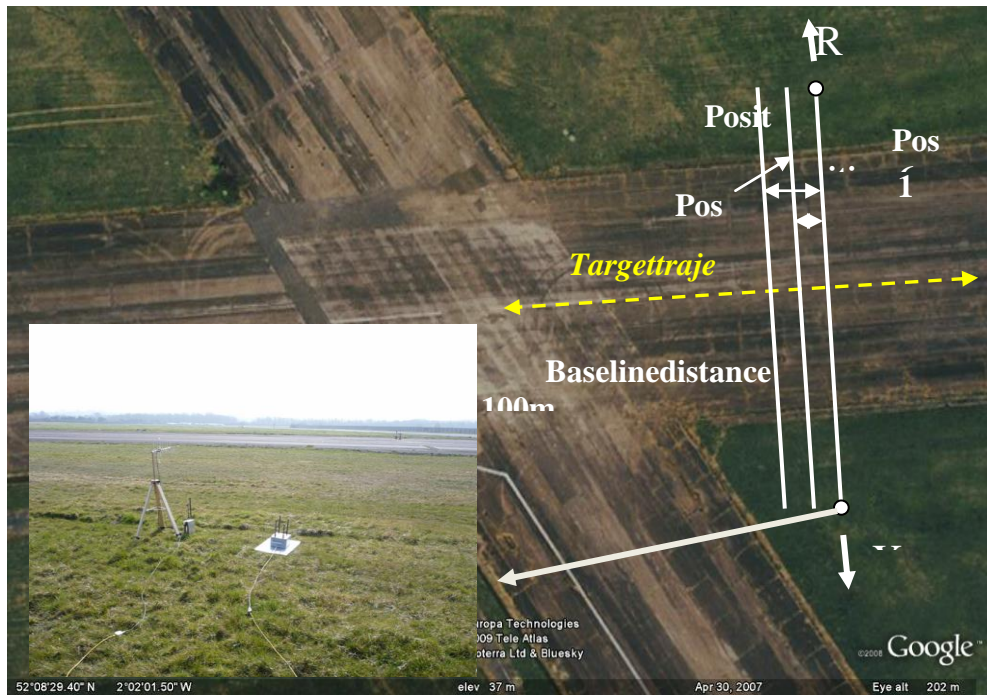


Figure 5.1 Tilesford airfield experiment description



(a)



(b)

Figure 5.2 Tileford field trial with Tx/Rx deployment (a) First three positions 1-3 on concrete (b) Another three positions (4-6) are on the grass

Although in [40], single selected samples for three positions had been compared to investigate the location effect, the frequency domain, PSDs for all of the 6 positions should be done as well. In addition, in Figure 5.3 and Figure 5.4, the 64MHz omni directional channel PSD signature and the 434MHz directional channel signature can detect the different positions (Po1- Po6 for 64MHz, and Po1- Po5 for 434MHz) effect interference is very limited when the environment is open without vegetation and other surroundings because the signatures fit quite well after they are applied, the target speed normalization algorithm. It is noteworthy that the speed estimation and normalization will be introduced in the next chapter and this is just to quote the result form the final result. The PSDs of other frequency channels such as 135MHz and 173MHz can be found in Appendix C.

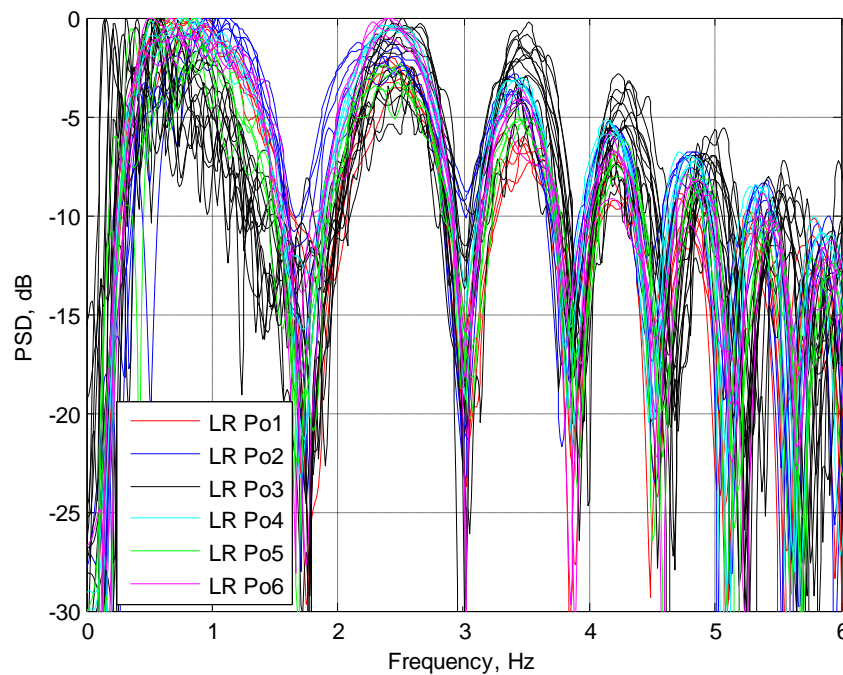


Figure 5.3 PSD signatures for the 64MHz frequency channel after speed normalization

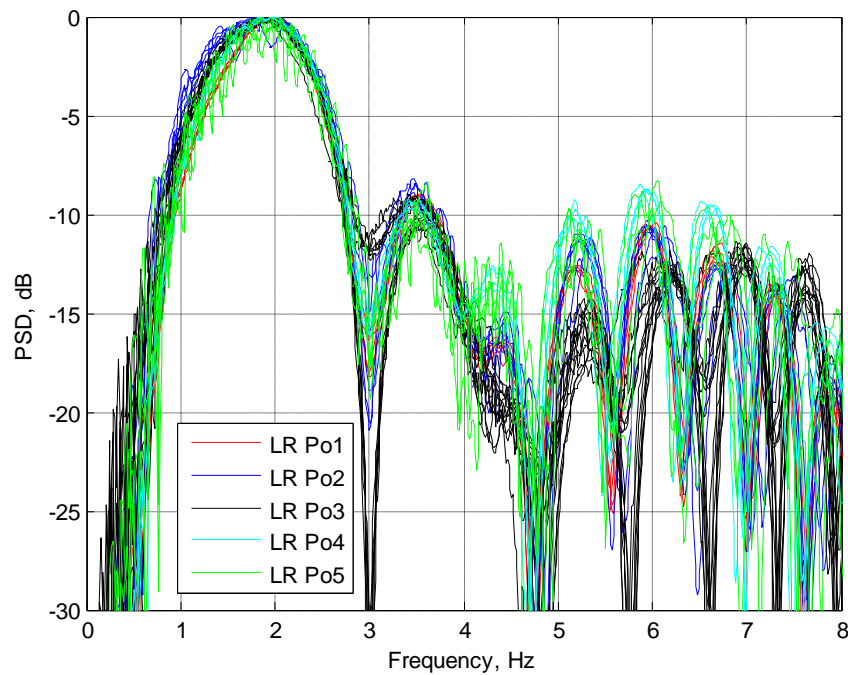


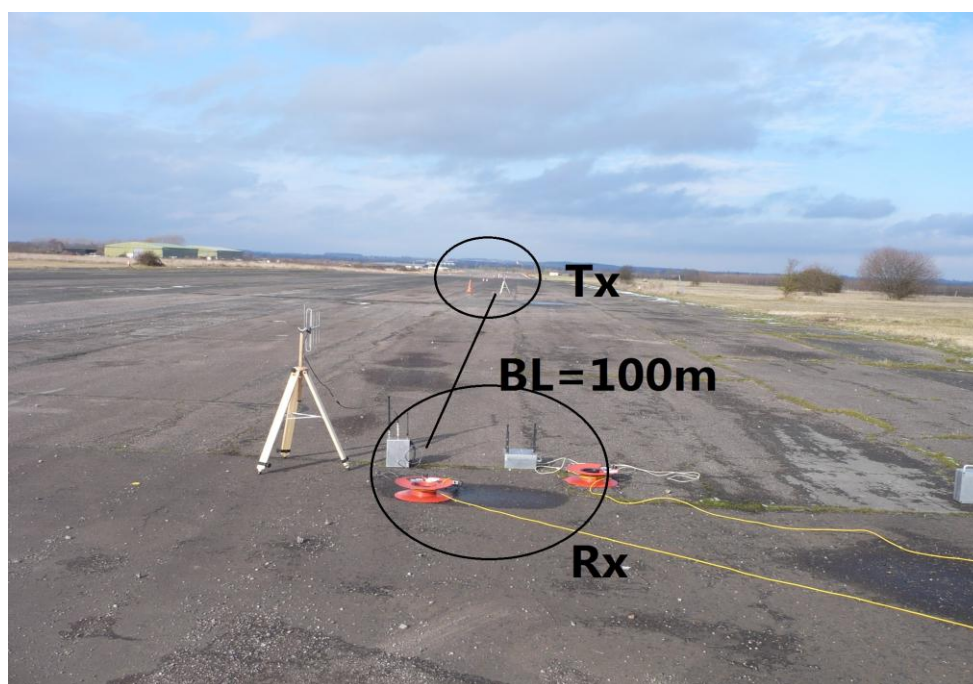
Figure 5.4 PSD signatures for 434MHz frequency channel after speed normalization

5.2.2 Target shape effect

Because of the RCS varies between the targets, different shapes will provide distinct signatures when applying the same frequency for target classification[59]. So in order to distinguish the different ground targets, the PSD signatures of varies target shapes will be used as the main features. In the Tilesford Airfield trial, the ground targets Landrover and Ford Fiesta were under test. Both of the targets were following the same route and the trajectory was perpendicular to the baseline. The baseline length is 100m and the Rx/Tx were deployed at the same location. Figure 5.5 (a)GFSR deployment view along the baseline shows the GFSR system with the four channel plus three channel devices placed on the ground. Figure 5.5 (a)GFSR deployment view along the baseline indicates the target Landrover running cross the baseline from left hand side while the second target Ford Fiesta was running from the right hand side is shown in Figure 5.5 (a)GFSR deployment view along

Chapter 5 Experimental evaluation and test result

the baseline . From all of the photos taken at the test site, it is shown that the environment has no blocks of vegetation or other buildings. Only the wooden fences were fitted away from the test site. In addition, the long length USB extension cables were used to reduce the operational position reflection effect to the receiver. Because the data were captured using a laptop computer and any movement from the operators can cause the fluctuation to the receiver signal.



(a)



(b)

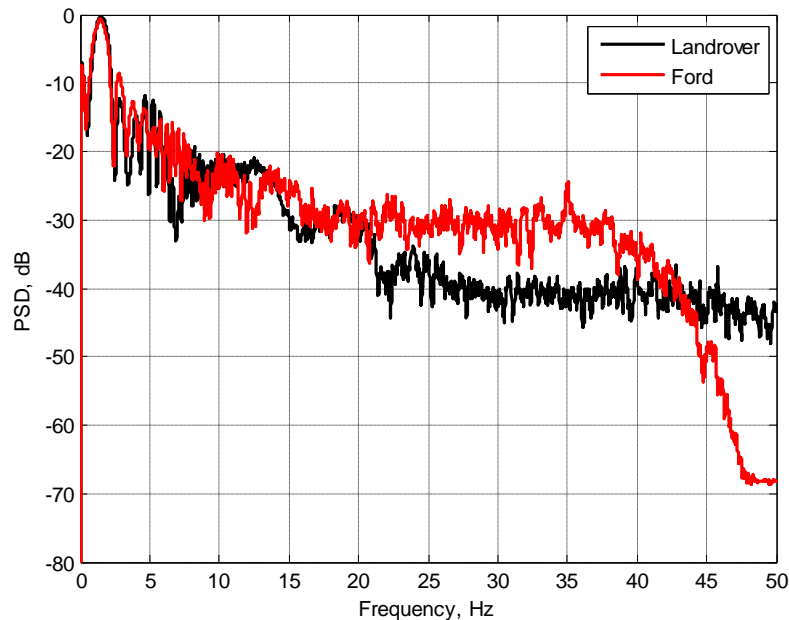


(c)

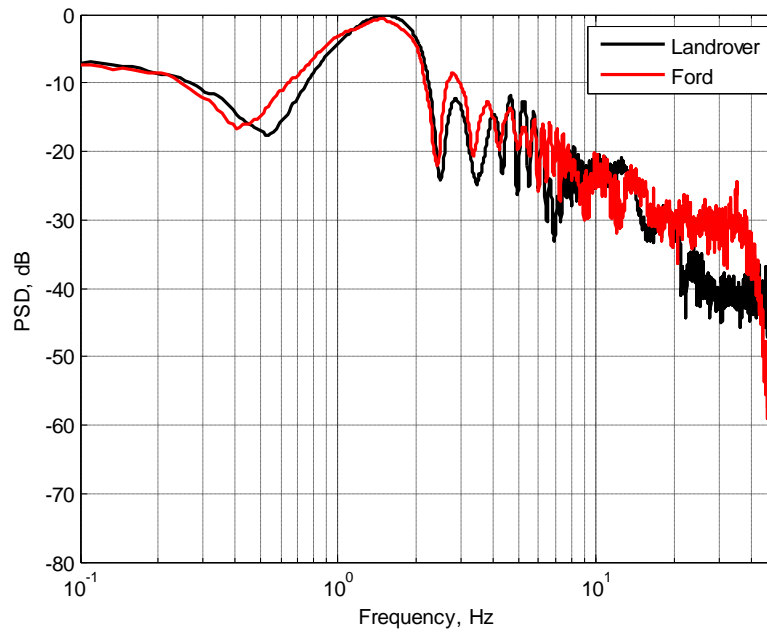
Figure 5.5 (a)GFSR deployment view along the baseline (b) Ground target Landrover passing through baseline (c) Ground target Ford Fiesta passing through baseline

The PSD signature for the Landrover and Ford Fiesta is compared and shown in Figure 5.6. The frequency channel 434MHz directional is chosen and the velocity of both targets are normalized to 10m/s. The black curve is Landrover while the red plot indicates the Ford Fiesta. Two types of the plot scale is applied, one the linear (Figure 5.6(a)) another one is semi logarithmic plot (Figure 5.6(b)). The reason for the semi logarithmic plot is to zoom in the details of the signature in the lower frequency domain.

It is clearly shown that the main lobe width of the Ford fiesta is wider than the Landrover. Since the width of main lobe for the target is equal to the target speed divided by the target length[39]. The length of Landrover is longer than the Ford Fiesta, so the main lobe of the Landrover is narrower than the target Ford Fiesta. At the higher frequency band which is more than 25Hz, the PSD of the Ford curve decreases quicker than the Landrover. In the target classification procedure, the difference shape effect can be used as the criterion features.



(a)



(b)

Figure 5.6 PSD signatures comparison for two targets, Land rover and ford fiesta.

(a)linear plot (b) semilogarithmic plot

5.2.3 Multiple speed effect

For the same type of the ground target, the signature of the PSD will change when the speed is varied. Figure 5.7 shows three examples of the PSD signatures for three different speeds at the same position. The target had the speed 8.94 m/s, 13.4 m/s and 17.9 m/s. It is observed that the main lobe and second null shifts to the higher frequency domain when the speed is increasing. This is because of the higher speed of the target maneuver, the higher frequency of the Doppler effect generated by the scattering signals. From Figure 5.7, the speed difference between the three runs is 4m/s and the x-axis is in the logarithmic scale. Therefore, the speed is in linear relationship with the frequency at the logarithmic scale.

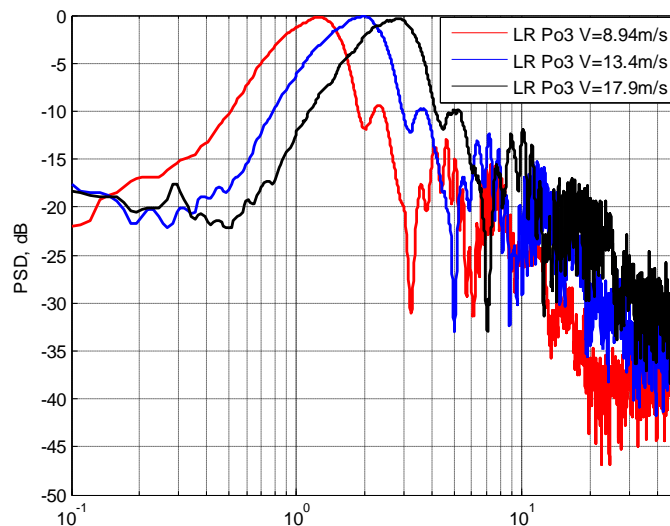


Figure 5.7 PSD signatures comparison for three different velocities using 434MHz directional antenna

The above figure shows only three samples for position3 at three different speeds. A total number of 15 runs were conducted after plotting all of the PSDs at position3. In order to group the PSD signatures for the similar speed ranges, all position 3 time domain signals are transferred into frequency domain and are presented in Figure 5.8.

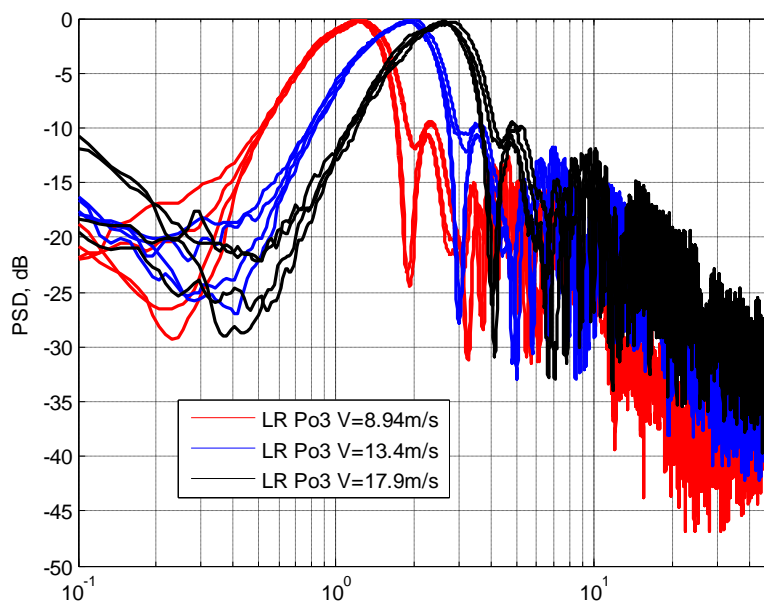


Figure 5.8 PSD signatures for 434MHz at multi speed in the same position (Tilesford airfield)

Figure 5.8 is the product of the PSD grouping for the 434MHz channels. Each colour stands for different speeds. The higher the speed of the target is, the further the second null of the main lobe can reach. In another respect, the target PSD will fit as close as possible if the parameter of the experiment keeps same. The speed normalization algorithm will be applied to these raw target signatures in the next chapter.

5.3 *Senneleys Park trial*

In the previous section 5.2, we investigated the open airfield environment. That is an ideal radio scenario for the GFSR system. However, when the system is working in the medium complexity environment, the greater uncertainty could contribute to the fluctuation in the received signal signatures when the Rx and Tx are placed in different positions. In addition, the aim of the trial at Senneleys Park is to find whether the large trees could cause multipath effect to the receiver. In this experiment, the four frequency channels, 64MHz, 135MHz, 173MHz and 434MHz channel, were used. The field has multiple large trees with only branches. As the experiment time was in winter and the foliage had fallen. Figure 5.9, shows the deployment of the GFSR system. The Rx/Tx

devices were located at three positions. All of the baselines had the same length. At position1, the Tx was put in front of a medium height tree while the Rx is clear. At position 2, there is one tree on the baseline and no obstacles behind of the Rx/Tx. A large tree locates behind the Rx at the position 3. Figure 5.10 shows the top view from Google Maps, and the vegetation positions can be identified.

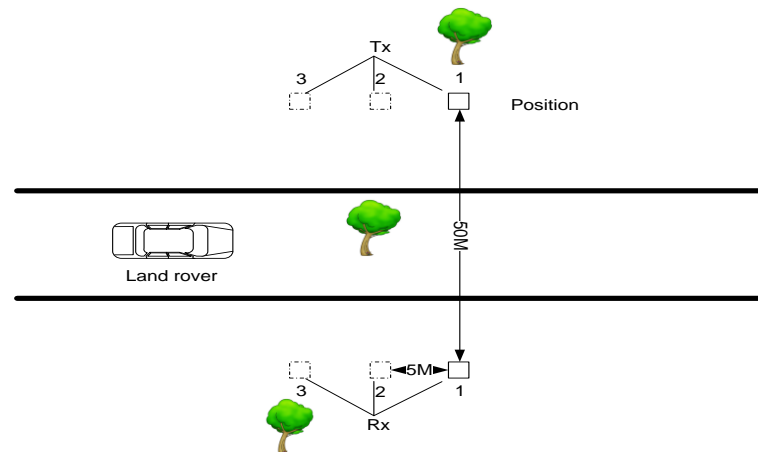


Figure 5.9 Top view of the Senneleys Park trial

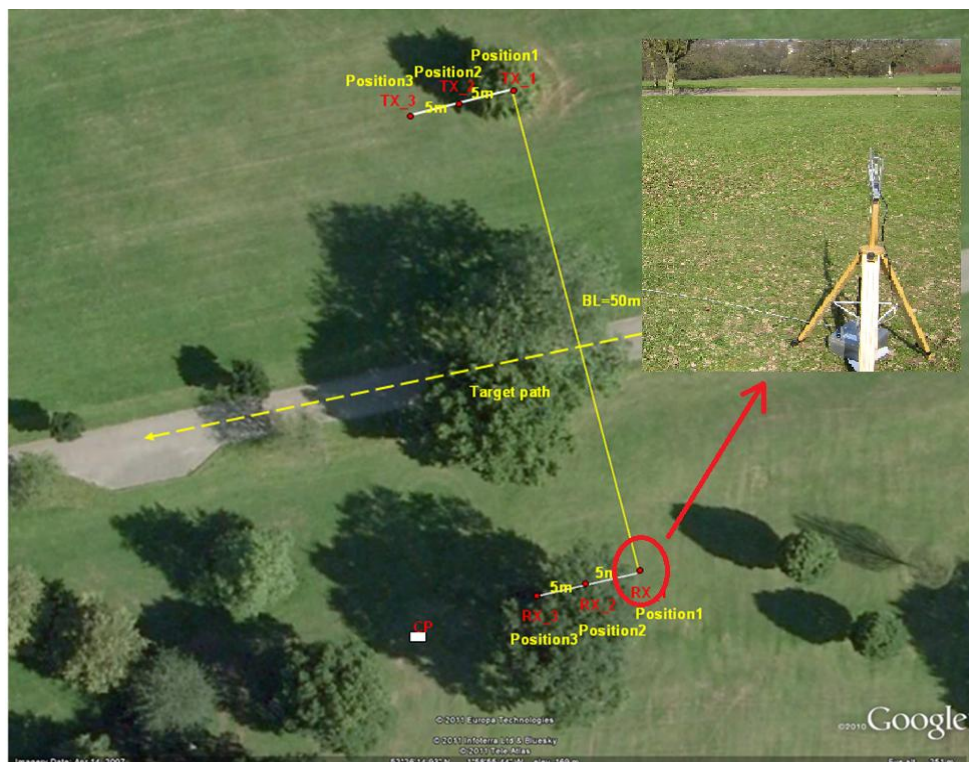


Figure 5.10 Senneleys Park trial top view on google map

Figure 5.11 shows the horizontal point of view when the target Landrover was running across the baseline when the Rx/Tx was located at position 2. On the day of the experiment, it was a clear sunny day with wind of no more than 3m/s.



Figure 5.11 Senneleys Park trial at position 2

Following the same procedure as in the Tilesford airfield trial, the spectrum analysis results for the Senneleys Park are presented in Figure 5.12 to Figure 5.15. These are the PSD signatures for the same target while the Rx/Tx were deployed at different positions. The speed of the target is normalized to 10m/s and the scale of the spectrum varies between the frequencies. For example, from the frequency channel 64MHz, the spectrum at the position 1 and 3 are fitted with each other while at position 2, the amplitude of the first main lobe is lower than the others. The possible reason for this effect is that the obstacle in the middle of the baseline will block the signals when the target moves across and decreases the reflection power in the lower frequency domain.

In the other higher frequency channels, the spectrum changes greatly as the Rx/Tx position moves. One of the reasons is that the frequency channel used the omni directional antenna and the receiver could capture the surrounding scattered signal from the vegetation. From the 434MHz channel with directional antenna, it is shown in Figure 5.15 that the three

positions have less difference than the omni directional channels. However, position 1 has a deeper first null at the frequency 0.5Hz. The rest of the spectrum signatures have highly repeatable factor. The multipath effect will be carried for the more complex environment and further analyses should be done in the future.

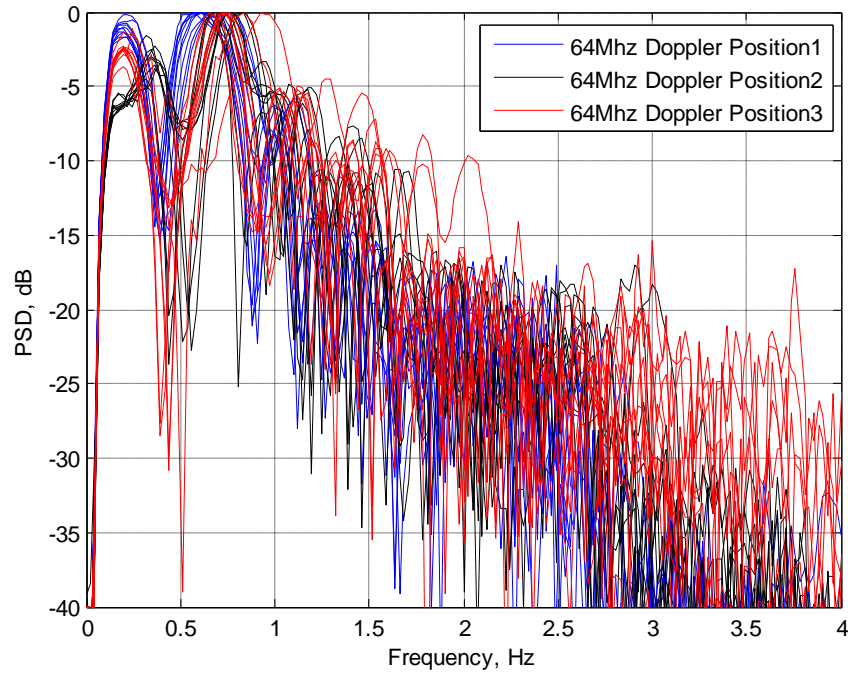


Figure 5.12 PSD plot of the 64MHz Doppler channel at 3 positions after speed normalization

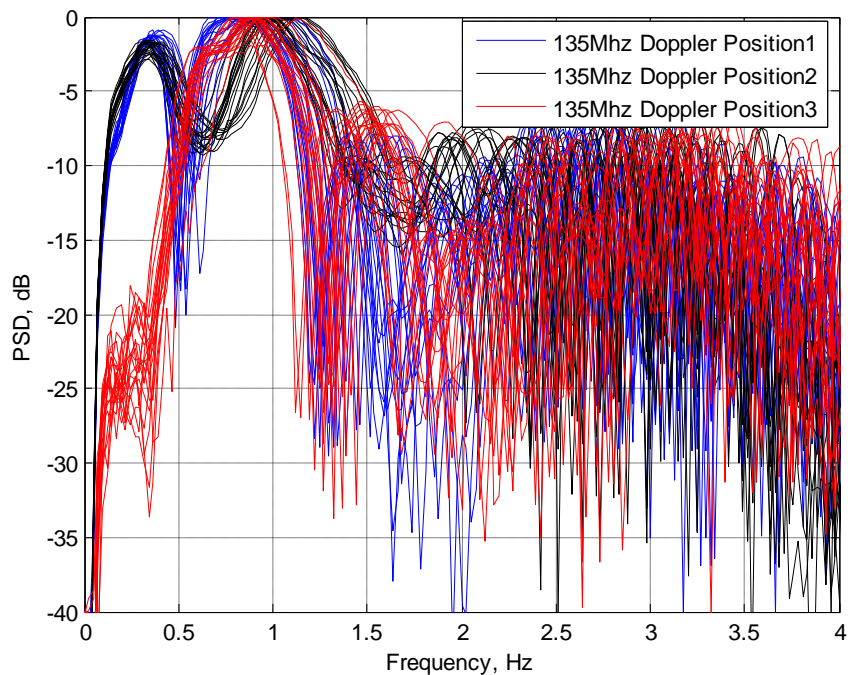


Figure 5.13 PSD of the 135MHz Doppler channel in 3 positions after speed normalization

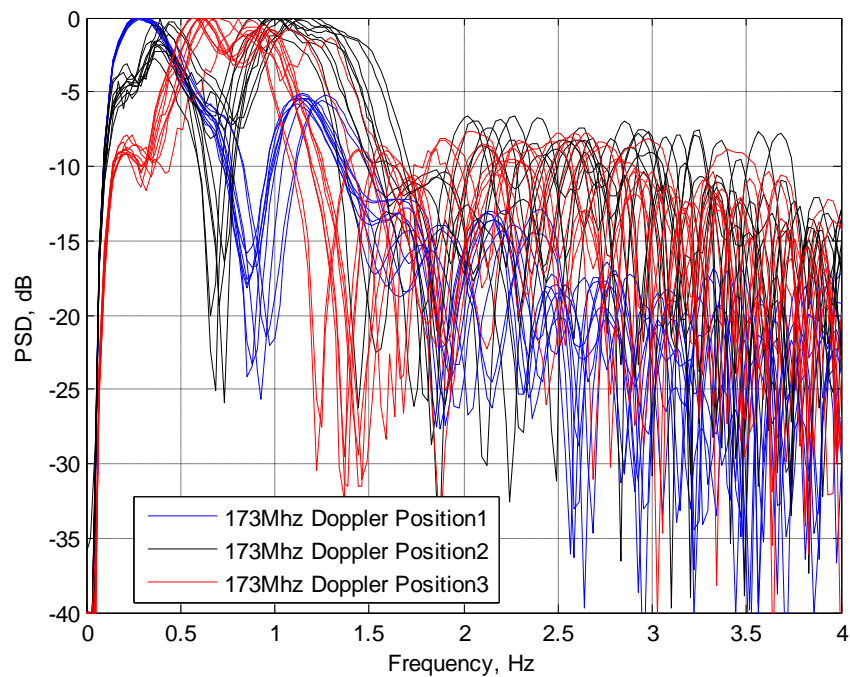


Figure 5.14 PSD of the 173MHz Doppler channel in 3 positions after speed normalization

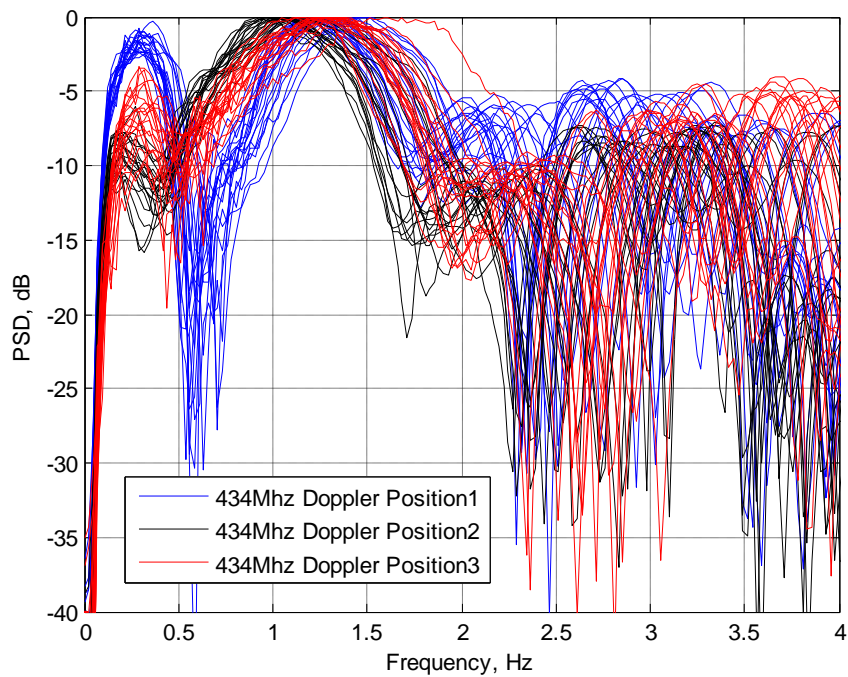
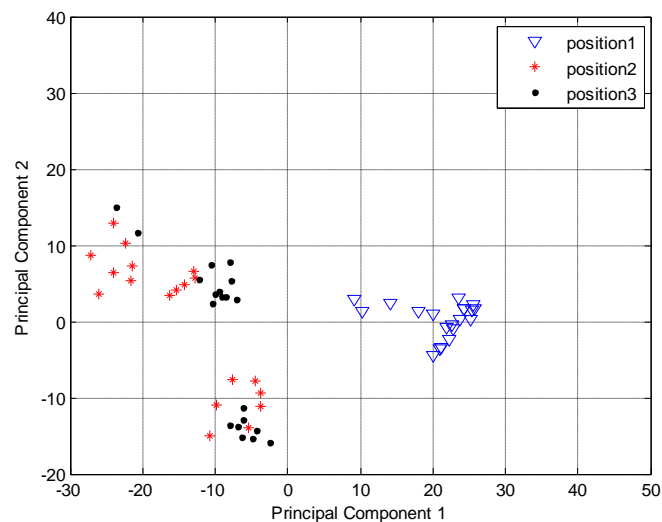
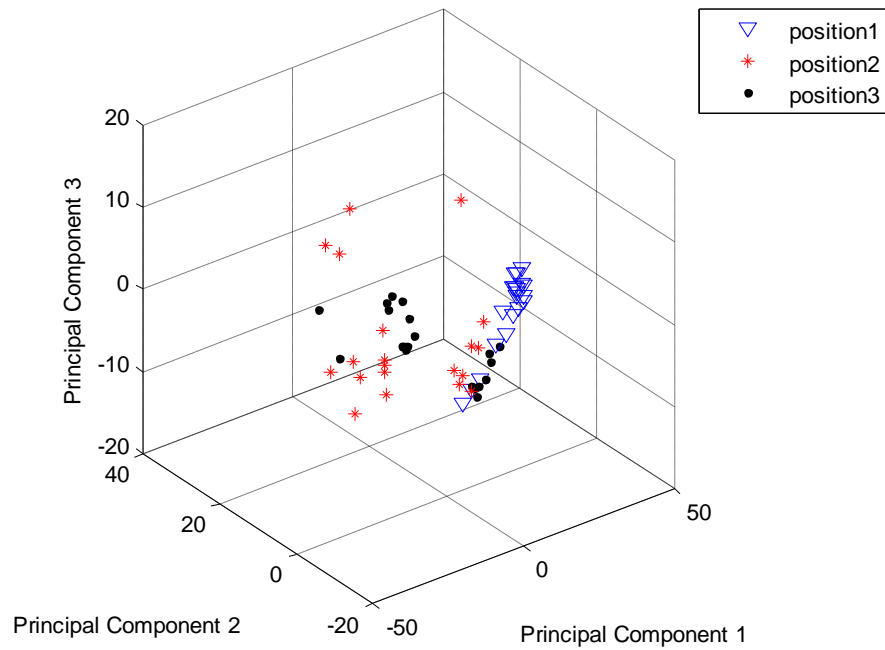


Figure 5.15 PSD of the 434MHz Doppler channel in 3 positions after speed normalization

The principle analysis is another perspective to observe the difference between the multi location effect. So the frequency 434MHz is chosen as an example and was plotted in the 2D principle plots in Figure 5.16.



(a)



(b)

Figure 5.16 PCA plot (a) two principal components (b) three principal components

From the Figure 5.16(a), the position 1 has larger distance to positions 2 and 3 while positions 2 and 3 has some overlap points which means positions 2 and 3 could be classified as the same type of the target while position 1 is another. This will cause the error in the target distinguish performance if the PCA is applied as the classifier. In order to avoid this occasion, more ‘clever’ classifier with low classification error should be designed and applied in the GFSR system.

5.4 Pritchatts car park trial

This section mainly investigates the PSD analysis in the same experiment environment and the same target with parallel Rx/Tx positioning. The surrounding areas of Pritchatts car park have a lot of arbour and low bushes organizing the complex radio environment. The PSD analysis is employed to classify the positioning effect in the frequency domain.

The top view of the test site Pritchatts car park, University of Birmingham, is shown in Figure 5.17. The Tx and Rx were located at three positions whose baselines were paralleled to each other in a distance of 5m, and the baseline length was 50 metres. The trajectory of the target was perpendicular to the baseline crossing the middle point. The frequencies used are 64MHz, and 434MHz. In the complex experimental scenario, the small foliage is presented along the trajectory of the target. Behind the Tx, the higher trees organized the vegetation fence at back of the Tx operational positions.



Figure 5.17 Top view of Pritchatts car park test site

In order to investigate the multi positioning effect, the Landrover was used as the target and Figure 5.18 shows the images of the target running across the baseline when the Rx/Tx was placed at the position 1 (Po1), position 2 (Po2) and position 3 (Po3). At position 1, the Landrover were driven at 4 increasing speed ranges 4.47m/s (Sp1), 6.7m/s (Sp2), 8.94m/s (Sp3) and 11.17m/s (Sp4).

From Figure 5.18, we can see that the low height bushes were growing at the left side of the target and at the far end of the Tx, there were tall tree fences. The Tx was put on the

grass surface while the Rx devices were placed at the sandy concrete with the 434MHz frequency antenna 1m above the ground.

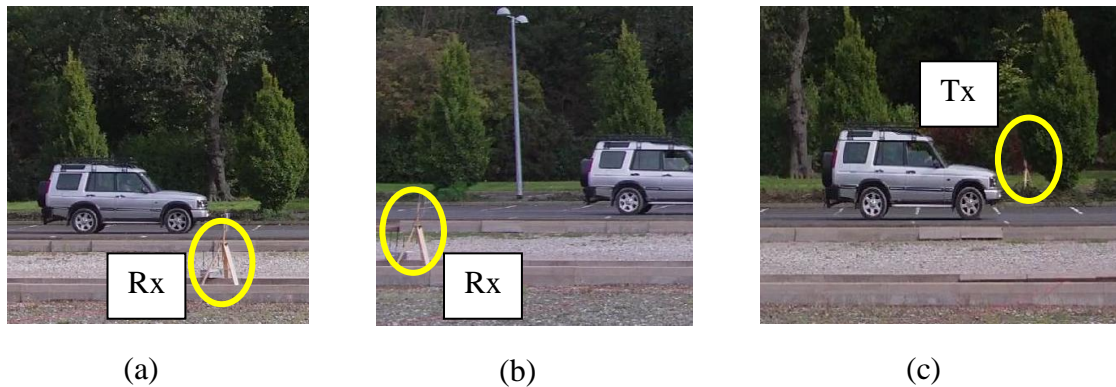


Figure 5.18 (a) position 1 (b) position 2 (c) position 3

In Figure 5.19, the speed and power spectrum amplitude is normalized, the frequency 64MHz and 434MHz were chosen for the location comparison. It is found that the signatures for all the three positions and speeds after speed normalization has highly repeatable consistent. This means the 64MHz has robust feature in the complex environment.

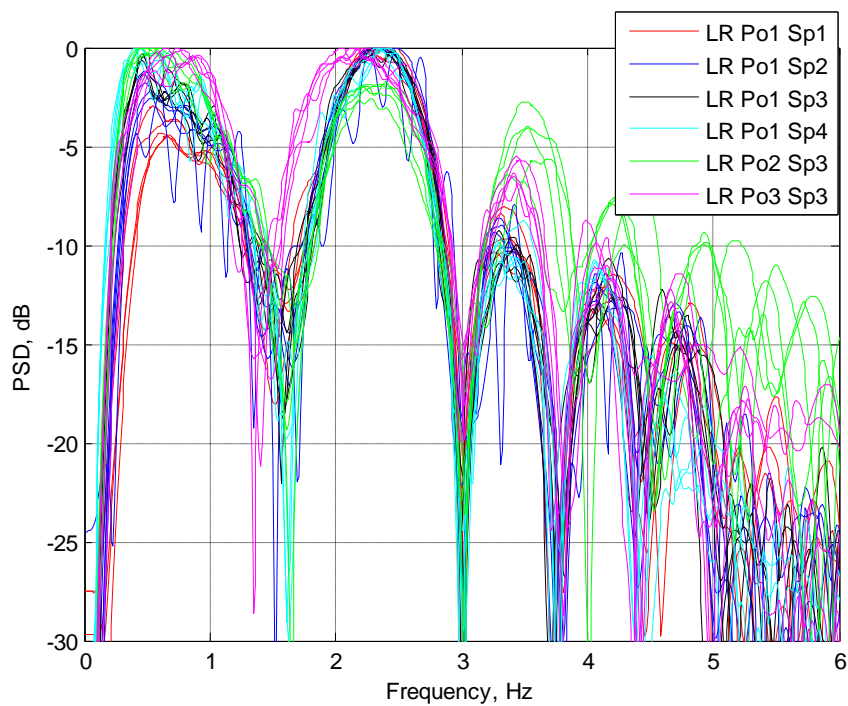


Figure 5.19 PSD for the 64MHz frequency channel

When the 434MHz frequency channel is processed after speed and the PSD normalization, the signatures are compared in the order of the one same position with four speed and 2 positions with one speed shown in Figure 5.20. The conclusion that can be drawn are as follows:

1. The PSDs of the target Landrover at the same position(Po1) with four speeds have no fluctuation using the 434MHz directional frequency channel. Therefore, the frequency domain signatures will keep consistency for the same target after speed normalization.
2. Different positions of the Rx/Tx will contribute to the main lobe shift and difference. The light green for position 2 with speed 8.94m/s and purple for position 3 with speed 8.94m/s have great difference with the grouped signatures in position1.

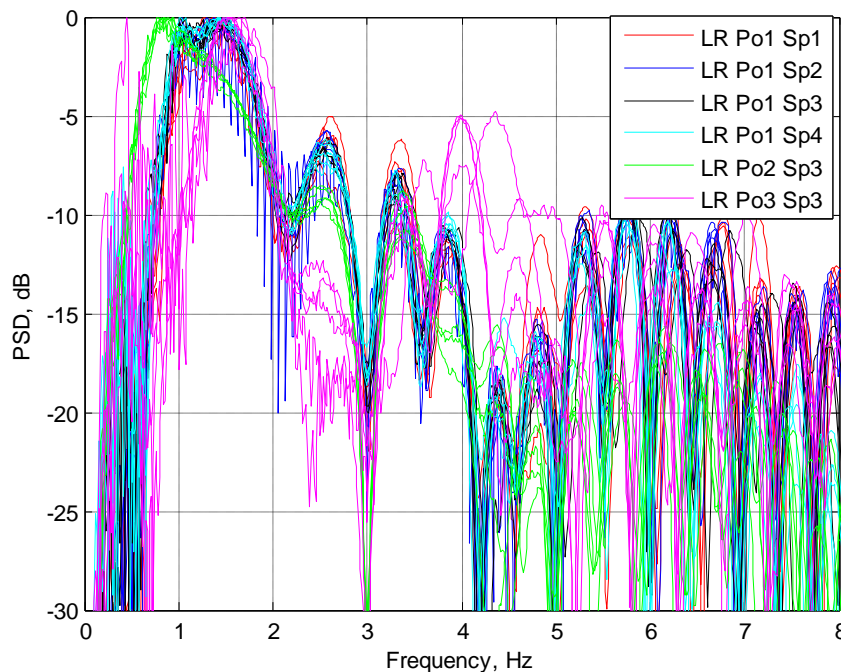


Figure 5.20 PSD for the 434MHz frequency channel (separate into two plots po1(spe1-4) and sp3(po1-3))

5.5 Conclusion

In this chapter, the experimental evaluation and initial result is presented. In the clear open space, the PSD of the target signal will be robust in the frequency domain when the transmitter and receiver are changing position, while keeping the baseline length constant and the reflection is only from ground without any vegetation reflection. When the environment becomes more complex, which involves in reflection interference from vegetation fence, the PSD of the target signal will be varied depending on the of the environmental complexity levels.

In the Tilesford airfield trial, we can obtain the conclusion that all the frequency from 64MHz to 434MHz channels (64MHz 135MHz 144MHz 151MHz 173MHz 434MHz Omni Directional and 434MHz Directional) can provide robust results when the position of the TX and Rx parallel changes because the environment is ideal without huge reflection from the air space. Comparing to the Tilesford airfield, the environment of Senneleys Park is more complicated, which has some arbour trees generating reflection from the branches. The channels 135MHz and 173MHz omni directional channels are affected a lot when we found that in position 3, the big tree blocked the transmitting route between Tx and Rx.

The most complex environment is Pritchatts car park which has more trees behind the transmitter and buildings are all around. The distortion in the PSD frequency space becomes even worse in the 434MHz Directional antenna with the Rx and Tx changing of positions.

In all three different complex environment trials, the 64MHz Omni Directional channel performs best among all channels since the wave length is 4.7metreswhich can diffract the obstacles, such as trees or buildings. The 434MHz directional antenna can only work well when there is little or no obstacle on the route of baseline.

Chapter 6 Speed estimation for the ground vehicle target

6.1 Introduction

Speed of target is one of the most important parameters in the forward scatter radar system for the reason that the target classification recognition accuracy decreased proportionally to the increased Speed Estimation (SE) error. In addition, the Doppler frequency shift follows the quasi-linear law when the target is crossing the baseline at different speed[3], [5], [60]–[66]. In this chapter, we improved the SE accuracy by employing the 90 degree multiphase shift reference function and more sophisticated criterion when we estimated the speed of the target. They are all automatically estimated and evaluated by large size experimental database achieved at Tilesford airfield and Pritchatts car park sites.

The structure of this chapter is as follows: subsection 4.2 discussed the full block diagram of SE procedure by detailed demonstration of processed signals; in the subsection 4.3, the conventional SE algorithm is explained in details with experimental result evaluation; the improved SE algorithm is proposed in the subsection 4.4 and 4.5. The conclusion is drawn in subsection 4.6.

6.2 Target signal pre-processing

The block diagram of the signal processing for the SE is shown in subsection 1.2.1. The first step is to extract the speed information by the estimation algorithm, and then in the next

subsection, we demonstrate how the raw recorded signal is processed through the designed algorithm. Finally, the PSD signature in the frequency domain shows the difference between raw recorded data and the processed data.

6.2.1 Signal processing diagram

The signal processing block diagram is displayed and explained in this subsection. Figure 6.1 shows how the recorded signal is transformed into the frequency domain for the further target classification. The purpose of the signal pre-processing and target detection is to extract the target signature S from the raw recorded signatures.

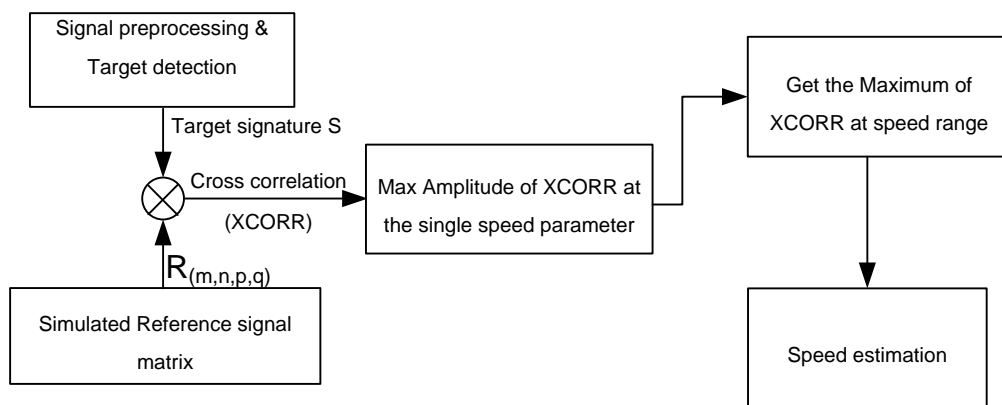


Figure 6.1 Signal processing block diagram

The simulated reference signal matrix is generated depending on the real environmental experiment configurations. The $R_{(m,n,p,q)}$, shown in Figure 6.1 is the simulated reference signals, where m is the speed vector, n is the time domain length of simulated signal, p is the cross point location on the baseline, q is the crossing angel between target trajectory and baseline. In the following sections, we only consider the restrict case for the experiment configuration. The ranges and parameters values are shown in Table 6.1.

Table 6.1 Parameters specification of reference signal

Parameters	Values
m	0m/s-30m/s
n	20 seconds
p	Midpoint of baseline
q	90 degree

The cross correlation between the recorded signals and the reference signatures are calculated using the equation (6.1):

$$XCORR_{v(i)}(t) = \int_{-T/2}^{T/2} S_r^*(\tau) R_{ref}[v(i), t + \tau] d\tau \quad (6.1)$$

Where, T is the total integration time, which is the visibility duration of vehicle target crossing the forward scatter zone. $S_r^*(t)$ is the conjugate of the recorded signature, R_{ref} is the generated reference functions, $v(i)$ is the speed range from 0 to 30m/s, i is the speed step index.

The equation (6.2) is the normalized discrete cross correlation of equation (6.1) so that the autocorrelations of the same signal at zero lag will get the final result of one. In [40], the conventional SE utilized the non-normalized cross correlation format since only one single pattern of reference signal is generated. The comparison of the new and conventional algorithm will be concluded in the following sections and in this section, only the equation is displayed:

$$XCORR_{v(i)}(n) = \frac{\sum_{m=0}^M S_r^*[m] R_{ref}[v(i), n+m]}{\sqrt{\sum_{m=0}^M S_r^*[m]} \times \sqrt{\sum_{m=0}^M R_{ref}[v(i), n+m]}} \quad (6.2)$$

where, M is the total length of the signal, n is the speed index in the time domain.

The output of cross correlation (XCORR) shown in Figure 6.1 is the correlation result between recorded signal and reference signal generated by the simulation parameters. Then

the block 'Max Amplitude of XCORR at single speed parameter' is to record the maximum cross correlation result at the predefined single speed parameter m . The equation (6.3) is the main procedure for the 2D signature generating process.

$$V^* = \underset{V(m)}{\text{Index}}(\text{Max}(\text{XCORR}(V(m)))) \quad (6.3)$$

More sophisticated criteria is considered in the SE procedure, and they are discussed in the following sections. After the speed values are all extracted from the SE algorithm, the speed is applied to the time domain speed normalization algorithm. Then the normalized time domain signal is transformed into the PSD in the frequency domain to indicate the accuracy of the SE results.

6.2.2 Demonstration of the signal pre-processing procedure

In this section, we demonstrate how the raw signal is pre-processed in the block diagram. The experimental collected data utilized here is captured from the Tillesford airfield, with the target speed at 8.94m/s and the radar channel is 144MHz Omni directional RSSI channel. The pre-processing and target detection block in Figure 6.1 is shown in Figure 6.2.

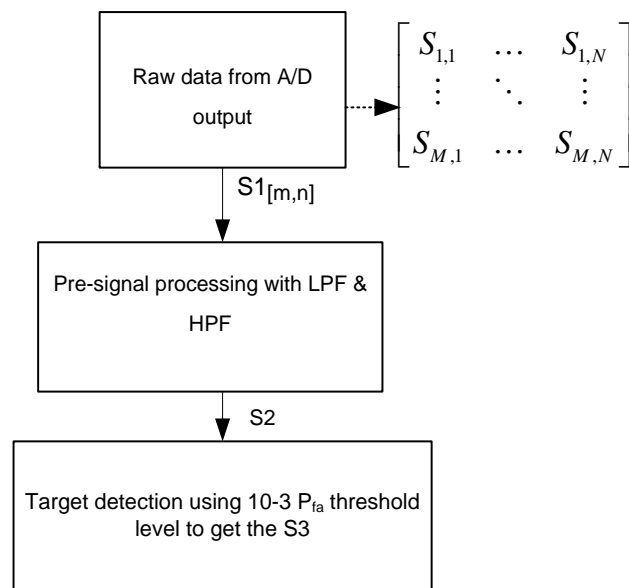


Figure 6.2 Signal pre-processing block diagram

As shown in the block diagram Figure 6.2, the first block with the raw data from A/D output is the Analogue to Digital Converter (ADC) in the hardware which converts the multi-channel analogue data into the digital format- binary file. S_1 is the data matrix in the size of $M \times N$, where M is the number of frequency channels, N is the sample in the sequence of time domain. Figure 6.3 illustrates the recorded raw RSSI data. The data is collected directly from 144MHz RSSI channel. In this sample runs, the total length of signature S_1 is 30 second with the sample frequency 100Hz, so the data has 3000 samples.

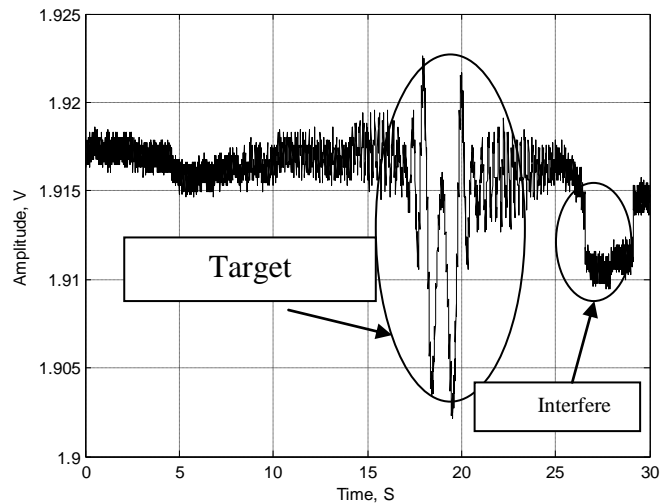


Figure 6.3 Raw RSSI 144MHz time domain signature S1

We can see clearly that the target signature starts around 15 seconds and ends around 25 seconds, while the unknown anomaly interference starts around 27 seconds which should be filtered out. The amplitude of the signature shows the mean value of the data is around 1.915 V and the DC offset should also be removed by subtracting the mean value of the total signal.

The next step is to extract the target signal in each frequency channels by the target detection algorithm (see chapter 3). The output of LPF and HPF filtering block is the signal S2, after passing through the filters, the unwanted noise lower frequency ($< 0.1\text{Hz}$) and higher frequency ($> 19.9\text{Hz}$) is filtered out. In the next block, the target detection algorithm introduced in the previous chapter is used to extract the pure target signature S3. This means that the target signature can be obtained after the target detection and extraction block.

Table 6.2 Filter configurations

Filter	Parameters	Frequency responds
--------	------------	--------------------

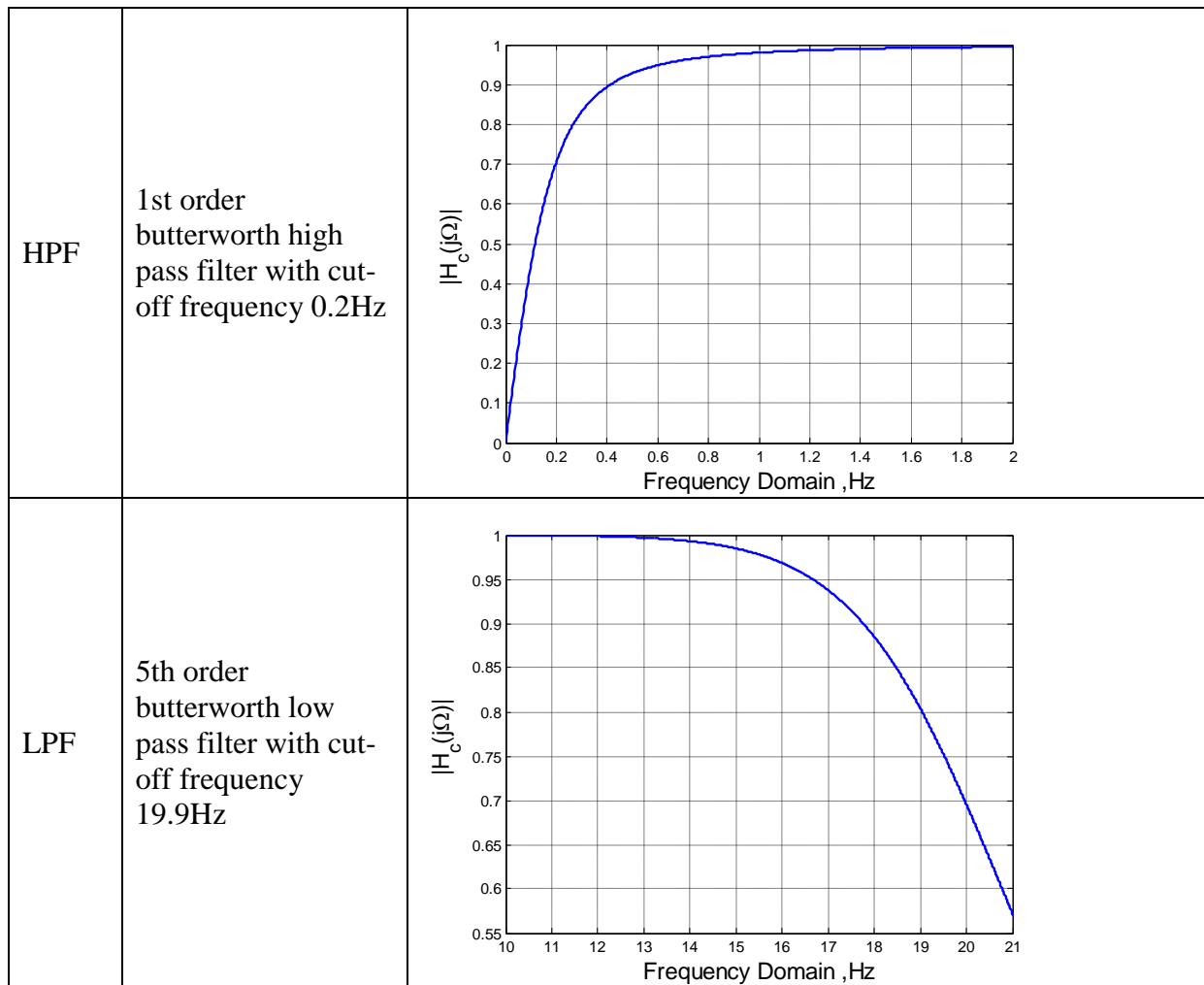


Figure 6.4 shows the signature of S2 whose DC component has been removed and the unwanted noise with lower frequency 19.9Hz the higher frequency 0.2Hz has been filtered out.

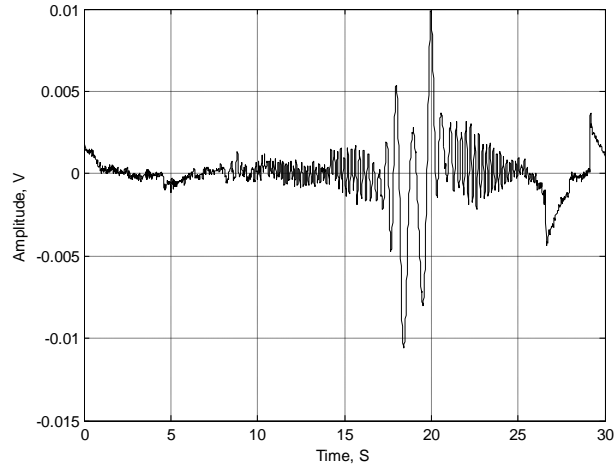


Figure 6.4 Time domain signature of S2

Figure 6.5 shows the truncated pure target signature without the unwanted interference.

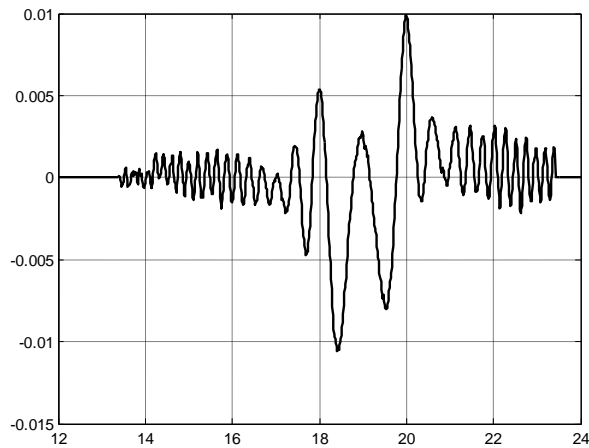
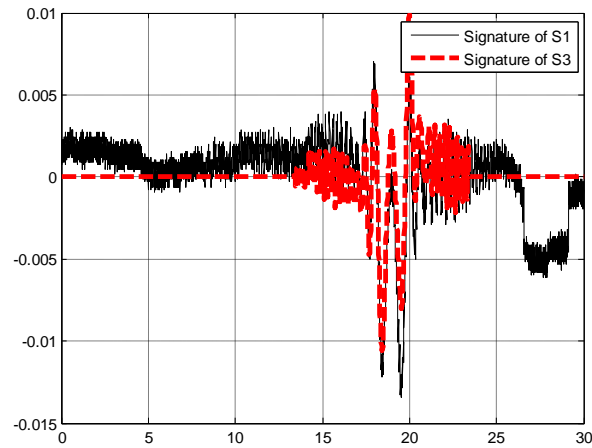


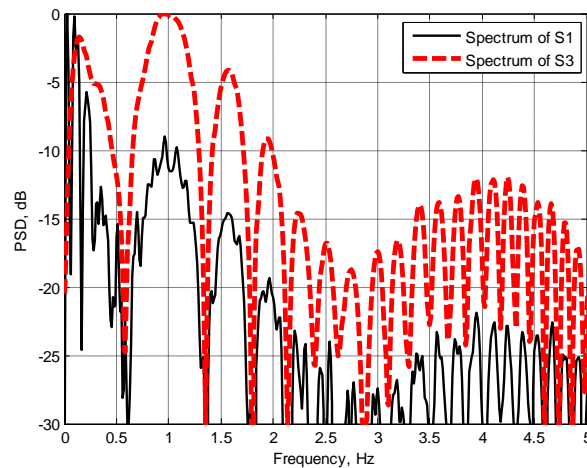
Figure 6.5 Truncated target signature S3

For the power spectrum density calculation, we applied the equation (6.4) which is the normalized PSD function to the raw recorded data and pre-processed data. The comparison of these two spectrums is illustrated in Figure 6.6.

$$PSD = 10 \log_{10} \left(\left| \sum_{n=0}^{N-1} \exp(-2\pi i k n / N) x_n \right| / \max \left(\sum_{n=0}^{N-1} \exp(-2\pi i k n / N) x_n \right) \right) \quad (6.4)$$



(a)



(b)

Figure 6.6 Comparison of the signature with and without truncation (a)Time domain signature of signal S1 and target S3(b)Spectrum of the S1 and S3

In Figure 6.6(b), we can find that the spectrum of detected target signature S3 (red dotted curve) has the maximum power spectrum at around 1 Hz and the PSD of S1 (black solid curve) has peak power at 0.1 Hz, because the interference DC component contributes more power in the lower frequency to the raw target signature and the target PSD signature will not be recognized until the interference is removed. Secondly, the Spectrum of S3 is smoother than

the spectrum of S1 since unwanted noises with higher and lower frequencies have been filtered out. Therefore, the target frequency domain feature can be clearly identified after signal pre-processing procedure. The main lobe width is determined to be 1Hz, while the side lobe power decreased dramatically 15dB after 2.3Hz.

6.3 Conventional SE algorithm

In this section, the conventional SE algorithm is introduced and evaluated by the experimental data. Due to the unitary type reference function confined SE estimation accuracy. It is shown in [53] that the unitary reference function can only be suitable for few frequency channels typically 64MHz, and it is found that the unacceptable SE error happens when we apply the traditional single phase reference function to part of the other frequency channels and data.

The unitary reference function in the equation (6.5)[40] is derived from the classic Monostatic radar equation .

$$r_i(n) = \cos\left(\frac{2\pi f_{ch}}{c} \times (R_{TX} + R_{RX} + L_{TA} - L_{BL})\right) e^{-\frac{1}{2}\left(\frac{2.5n}{N/2}\right)^2} \quad (6.5)$$

where, f_{ch} is the channel frequency, c is the speed of light, R_{TX} is the distance from TX to target, R_{RX} is the distance from RX to target, L_{TA} is the target cross range, L_{BL} is the baseline length, Gaussian window $e^{-\frac{1}{2}\left(\frac{2.5n}{N/2}\right)^2}$ is applied to the reference signals.

The equipments we used are multi-frequency integrated Rx/Tx devices which have 64MHz, 135MHz, 141MHz, 151MHz, 173MHz omni directional and 434MHz Yagi antenna

channels operated simultaneously. The target vehicle crossed the baseline 30 times. The SE result of Tilsford airfield is evaluated using the single reference function, which is cosine waveform.

Conventionally, the SE algorithm based on the maximum cross correlation calculation utilizing the unitary coherent reference signal can be successfully applied to the 64MHz frequency channels. However, the same reference function could not be applied to the other frequency channels and a mismatch was shown between recorded signal and simulation functions.

Assuming we have got the speed parameter 8.94m/s of the data shown in Figure 6.5 . The single cosine wave simulation reference signal shown in the Figure 6.7(a) was applied in the SE algorithm to get the cross correlation result, illustrating in Figure 6.7(b). We can find that the main lobe of cross correlation result has suppressed the side lobes, which are regarded as good match for the recorded signal.

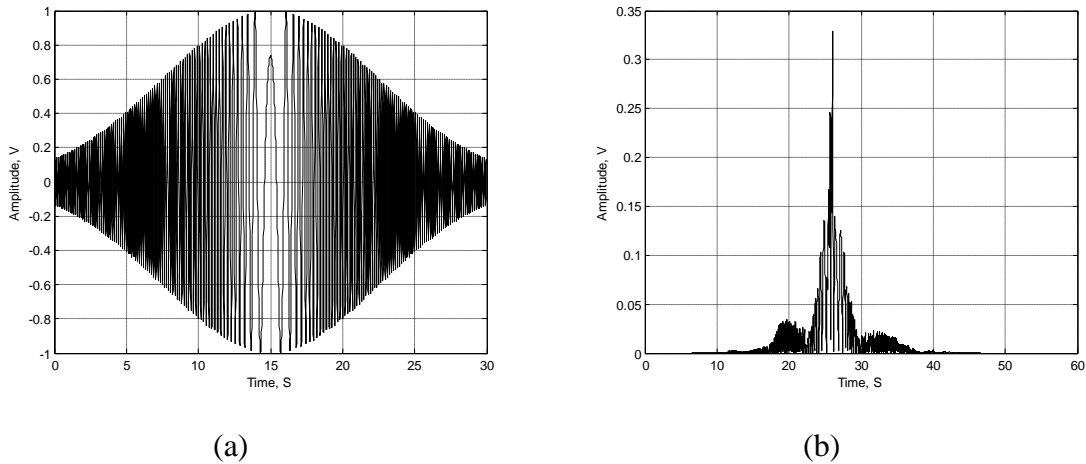


Figure 6.7 (a)Time-domain cosine reference signal (b) modulated cross correlation result

We apply the Root Mean Square Error (RMSE) calculated by the equation (6.6) to indicate the variation between the estimated speed(V_{est}) and actual speed(V_{act}).

$$RMSE = \sqrt{\frac{1}{M} \sum \left(\frac{V_{est} - V_{act}}{V_{act}} \right)^2} \quad (6.6)$$

where, M is the total size of data, V_{est} is the estimated speed value, and V_{act} is the actual speed of the target. In Table 6.3, we evaluate the speed estimation by RMSE in all frequency channels. It is suggested that the cosine format reference functions can acquire high accuracy speed result (<6%) in 64MHz frequency channel. From Table 6.3 we can get the conclusion that the SE result has very large RMSE values; more than 10% when using the cosine wave reference function in 5 frequency channels except the 64MHz. It indicates that the single cosine wave form does not match with the other frequency channels database.

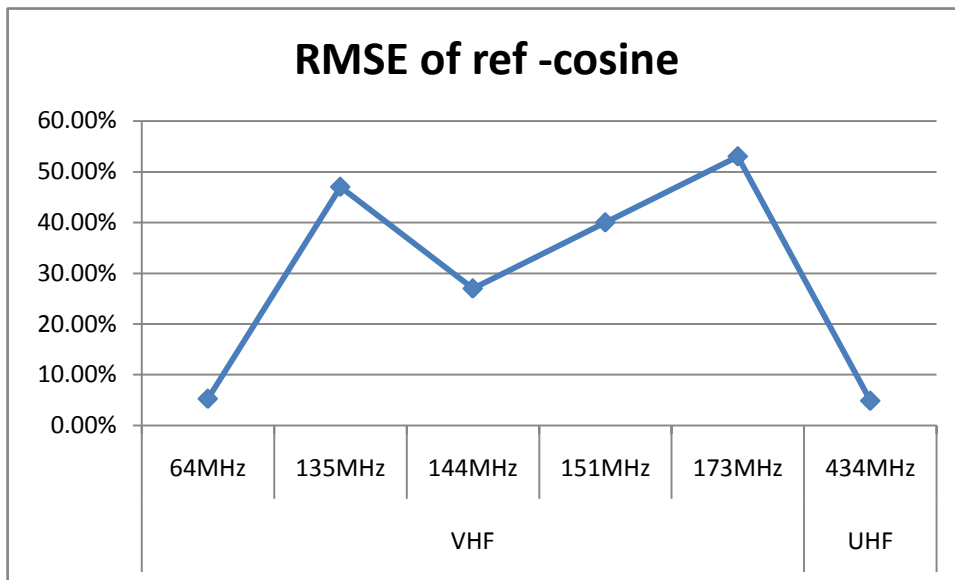


Figure 6.8SE RMSE results for Tilesford airfield by using cosine wave reference function

Table 6.3SE RMSE results for Tilesford airfield by using cosine wave reference function

Band	Frequency	Channels	Antenna Type	RMSE
VHF	64MHz	Doppler and RSSI	Omni directional	5.3%
	135MHz	Doppler and RSSI	Omni directional	47%
	144MHz	Doppler and RSSI	Omni directional	27%
	151MHz	Doppler and RSSI	Omni directional	40%
	173MHz	Doppler and RSSI	Omni directional	53%
UHF	434MHz	Doppler and RSSI	Yagi	4.9%

6.4 Speed normalization using modelling signal

In this section, rough speed estimation process will be introduced. In the frequency domain, the width of the main lobe of the target signature depends on the speed and length. From the target classification perspective, the target speed should be estimated as accurately as possible for the target PSD normalization.

The modelling time domain target signals with the multiple speeds are shown in Figure 6.9.

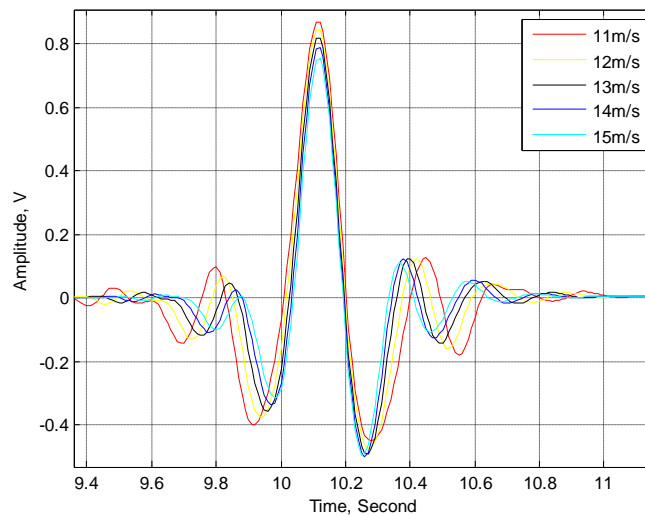


Figure 6.9 Time domain signatures of modelling target signal

Then we applied the time domain speed normalization algorithm to the signatures of the modelling signals.

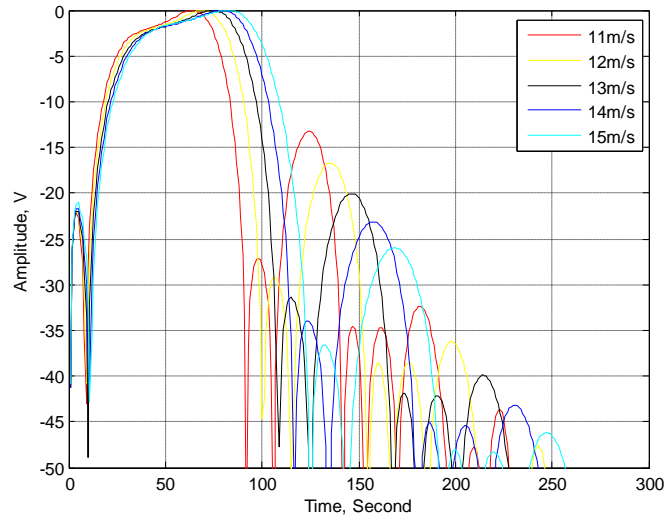


Figure 6.10 PSD of the time domain target signatures

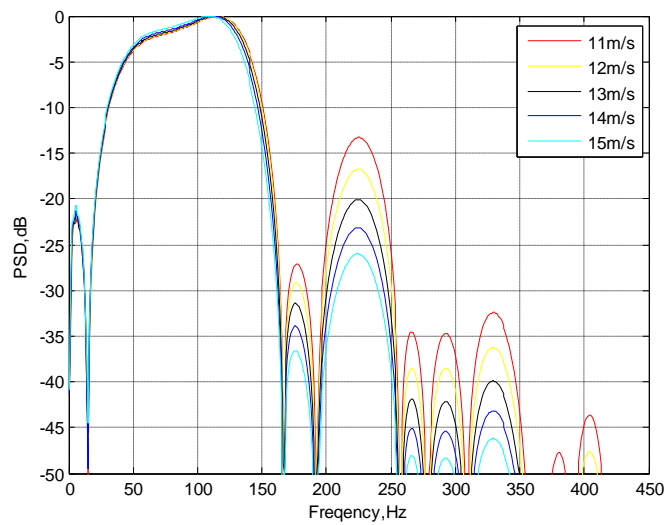


Figure 6.11 PSD of target after speed normalization

For the recorded signals, the time domain speed normalization is applied to the same reference speed so that the PSD target feature extraction can be utilized.

6.5 Improvement of the SE algorithm

6.5.1 Multiple 90 degree phase shift reference functions

From the RCS perspective, the moving target trajectory can be divided into three stages, shown in Figure 6.12, the reflection region (stage 1 and 3), where the reflection of radio wave is the dominate signature. The forward scattering zone is at stage 2.

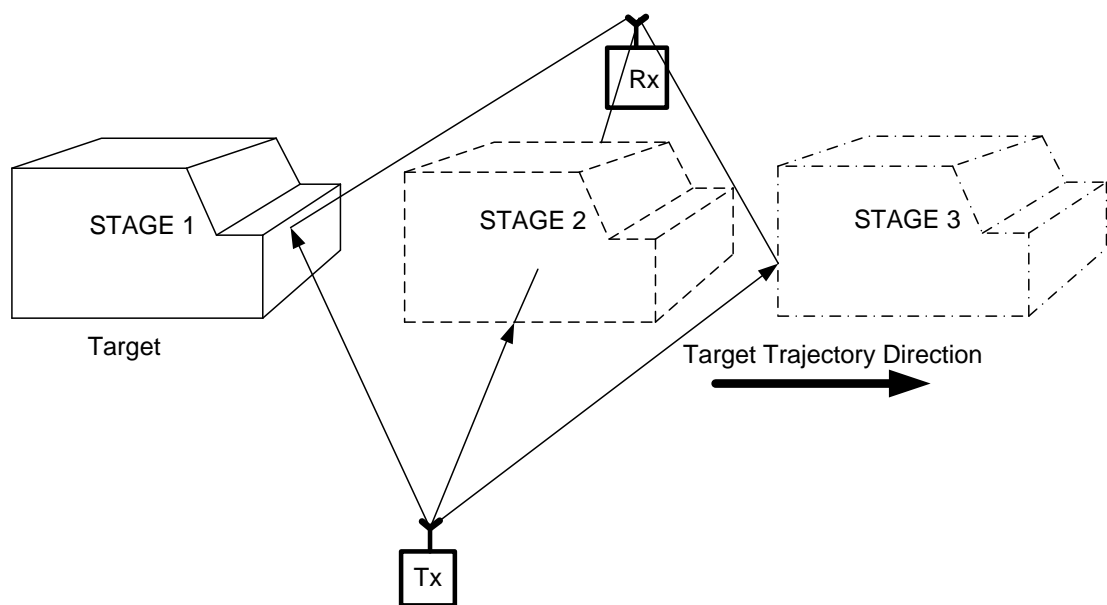


Figure 6.12 Target movement trajectory stages

Figure 6.13 shows the time domain signature comparison for all the frequency channels from 64MHz to 434MHz at Tilsford airfield. We can find that the central of the signatures for all of the frequencies match.

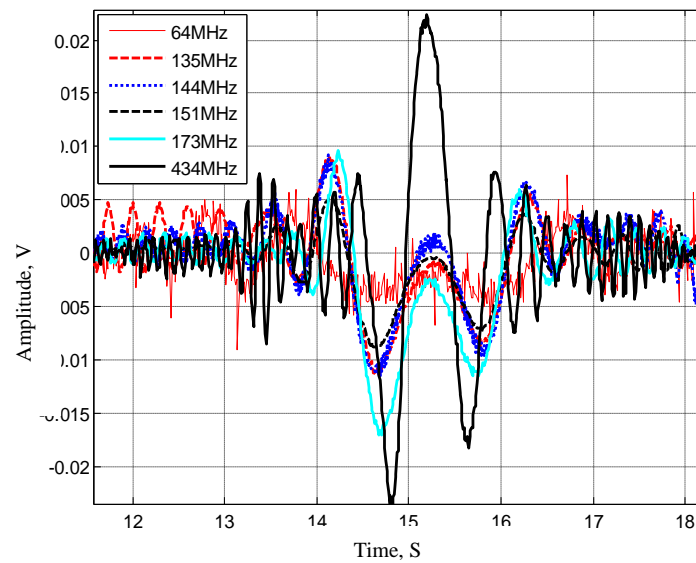


Figure 6.13 Comparison of signatures for all the frequency channels at Tilesford airfield

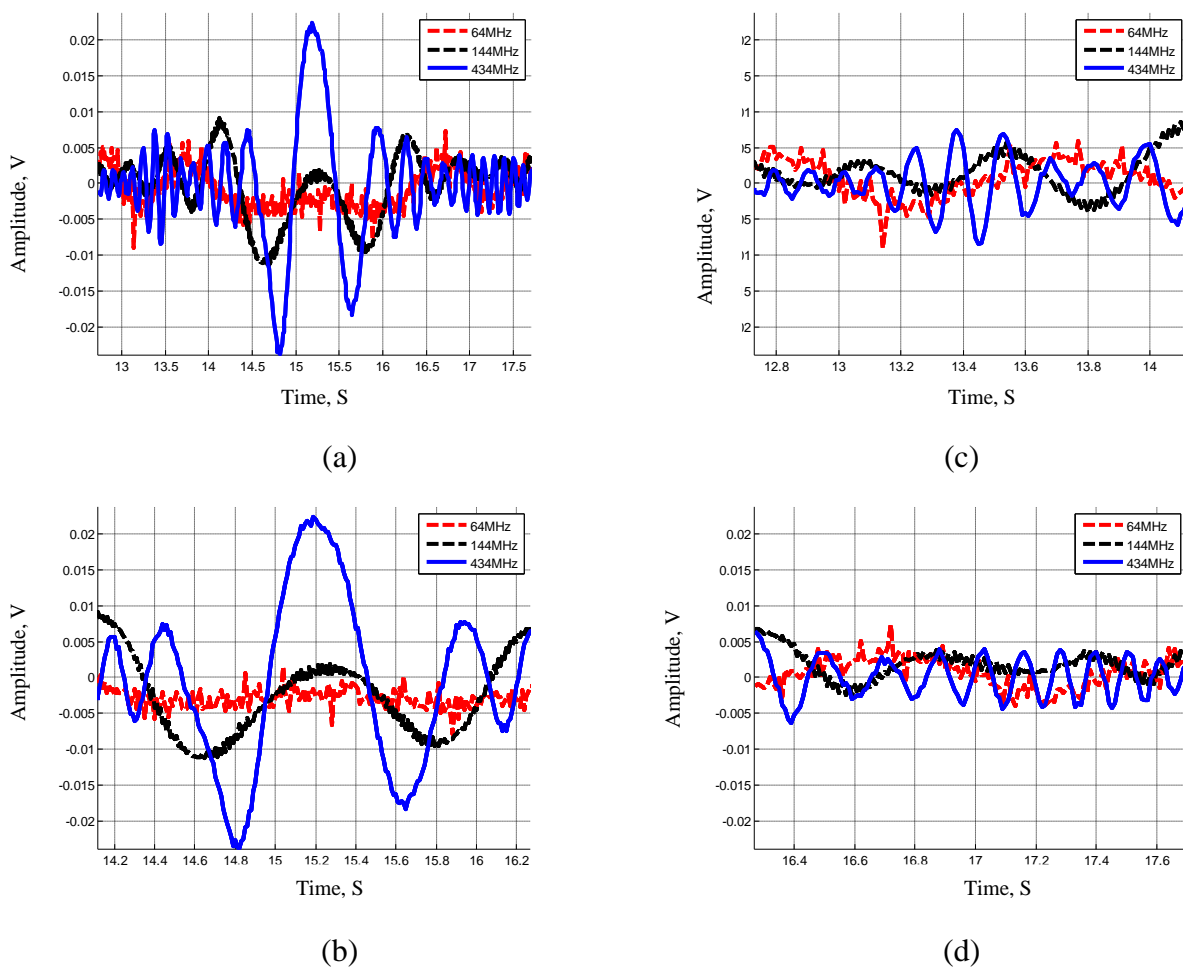


Figure 6.14 Time domain signal comparison of three frequencies

Chapter 6 Speed estimation for the ground vehicle target

- (a) Time domain signatures comparison of three channels
 (b) Back scattering zone time domain signatures (stage 2)
 (c) Radio reflection zone time domain signatures(stage 1)
 (d) Radio reflection zone time domain signatures(stage 3)

Table 6.4 Frequency ratio comparison

Stages	Stage 1	Stage 2	Stage 3
Number of Circles ratio	11:3	4:2	11:3
Frequency ratio	434MHz/144MHz=3		

The 90 degree phase shift reference functions are defined in the equation (6.7). As we can see, the reference function can be expanded to four 90 degree reference functions.

$$r_i(n) = \cos\left(\frac{2\pi f_{ch}}{c} \times (D_{TX} + D_{RX} + L_{TA} - L_{BL}) + \frac{\pi}{2} \times i\right) e^{-\frac{1}{2} \left(\frac{2.5 - n}{N/2}\right)^2} \quad (6.7)$$

Where $i = 1, 2, 3, 4$ the reference function $r_i(n)$ expands to the format -sine, -cosine, sine and cosine.

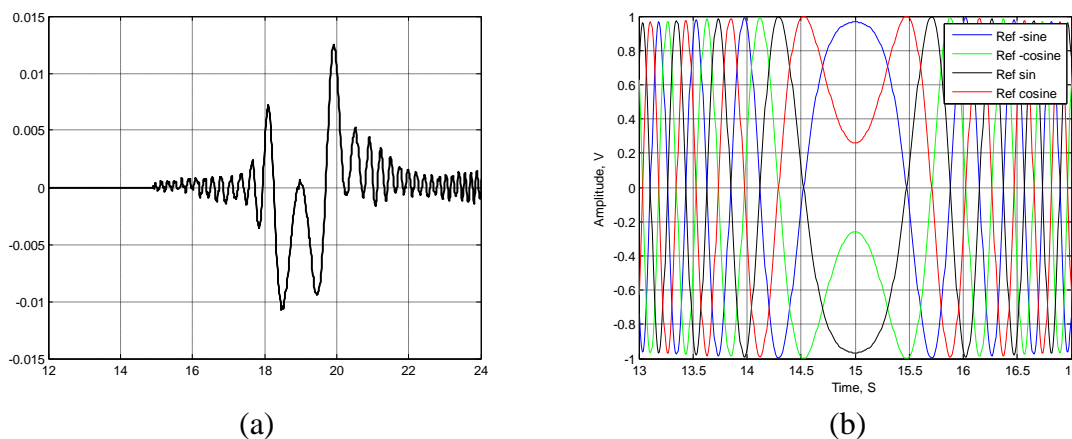


Figure 6.15 173MHz (a) recorded signature and (b) reference function

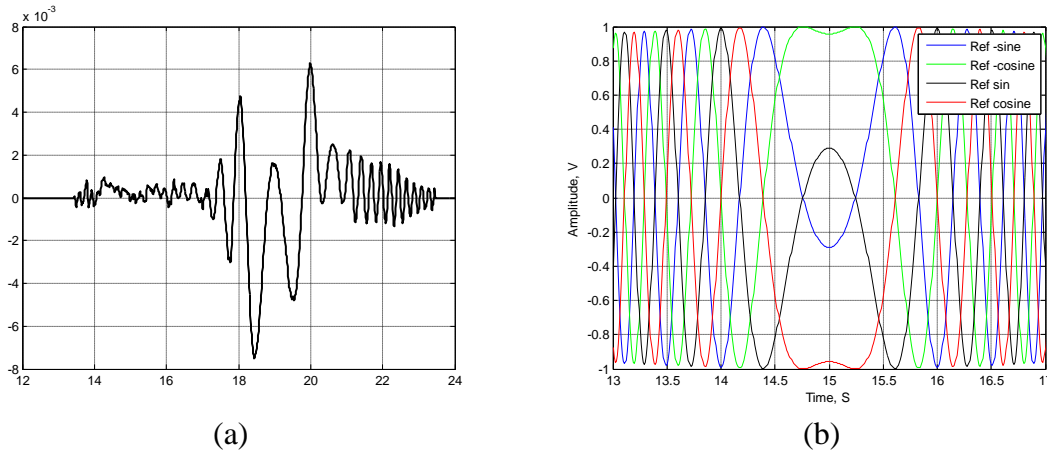


Figure 6.16 151MHz (a) recorded signature and (b) reference function

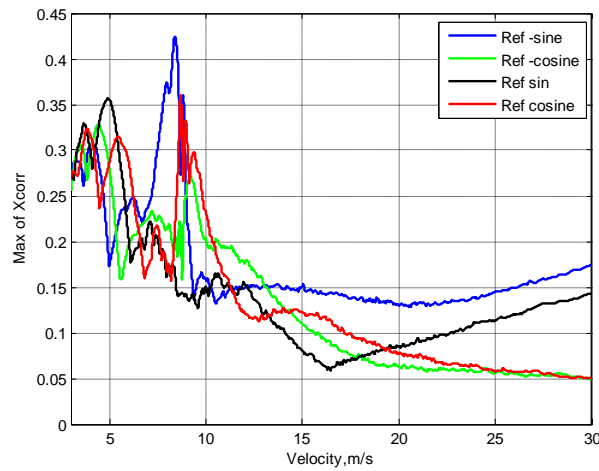


Figure 6.17 Max of Xcorr versus speed

Figure 6.18 shows the maximum of cross correlation versus the speed signature and the different color stand by varies reference functions, -sine in blue, -cosine in green, sine in black and cosine in red. We can find that the -sine waveform can acquire maximum cross correlation level and the speed of 8.4m/s is estimated by using this reference function.

6.5.2 Experimental evaluation of the improved SE algorithm

The 90 degree phase shift reference functions are introduced in this section and we applied the reference function to the same data base we acquired from the Tilsford airfield,

among the four reference functions, the maximum of cross correlation speed peak is selected as the result and the RMSE values stand for the accuracy of the estimation algorithm. We can find that the SE error can be reduced from more than 10% into less than 7% in higher frequency channels and these database is also suitable for SE procedure.

Table 6.5 Comparison of RMSE between using the single cosine and maximum multiple reference functions

Frequency	RMSE using max cosine ref	RMSE using max multi ref
64MHz	5.3%	5.3%
135MHz	47%	5.3%
144MHz	27%	6%
151MHz	40%	4%
173MHz	53%	6.1%
434MHz	4.9%	4.5%

. While the cosine waveform reference function has 84.9% match rate with the 434MHz database.

Table 6.6 shows the summary portion of runs corresponding to the optimum reference functions for all of database at Tilesford. It is suggested that some format of reference function can prevail the other reference functions within the same frequency channels. For instance, in 173MHz frequency channel, 90.9% of data has the -cosine waveform as the optimum reference function. While the cosine waveform reference function has 84.9% match rate with the 434MHz database.

Table 6.6 Optimum reference functions portions in each frequency channels based on the least RMSE result

Reference Functions	64MHz	135MHz	144MHz	151MHz	173MHz	434MHZ
-sine	2.7%	48.5%	27.3%	6.1%	0.0%	15.1%
-cosine	0.0%	33.3%	9.1%	0.0%	90.9%	0.0%
sine	24.3%	0.0%	0.0%	93.9%	9.1%	0.0%
cosine	73.0%	18.2%	63.6%	0.0%	0.0%	84.9%

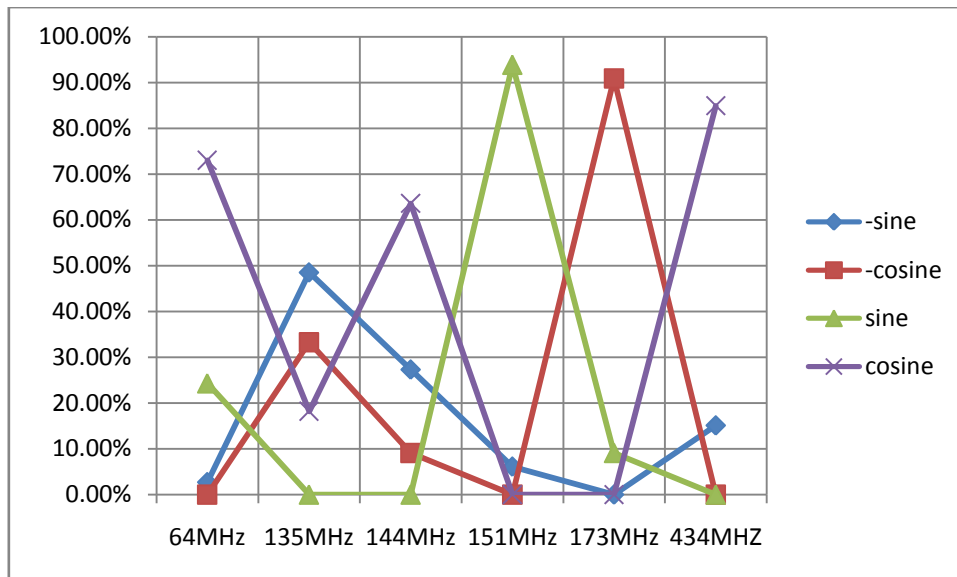


Figure 6.18 Least RMSE chart for varies frequencies

6.6 Empirical Improvement to the SE algorithm

6.6.1 Introduction to the slope algorithm

In the high accuracy FSR target classification processing, the speed estimation for the moving target is the most essential procedure for good classifier design. The previous sections only focused on the maximum of cross correlation amplitude of the XCORR. This subsection introduced the XCORR slope algorithm for the speed index identifier. Assume we have the simulated target signature using -sine reference function shown in Figure 6.19, named Ts. After applying the four phase shifted reference functions to the simulated target signal, we can get the Max of XCORR versus speed illustrated in Figure 6.20. The conclusion can be drawn that the target speed is estimated 10m/s by the maximum XCORR amplitude criterion. Comparing the XCORR curve with other XCORR product by the rest of reference functions, the slope of the -sine XCORR curve has the maximum value 9.2 in the Table 6.7.

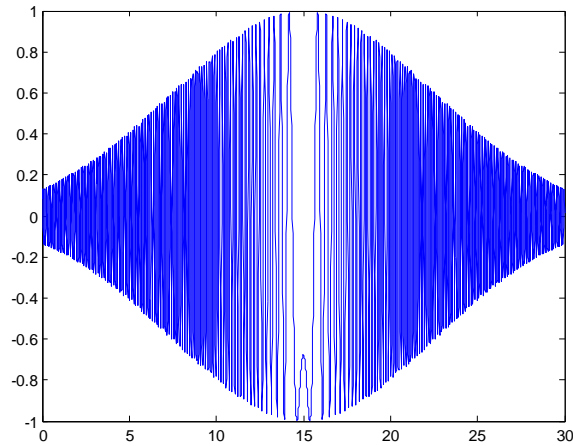


Figure 6.19 Simulated target signal using -sine function at 10m/s

Table 6.7 Maximum of XCORR and slope value for the simulation result

	Max of XCORR	Slope value
-sine	0.76	9.2
-cosine	0.38	1.6
Sine	0.28	2
cosine	0.27	1.4

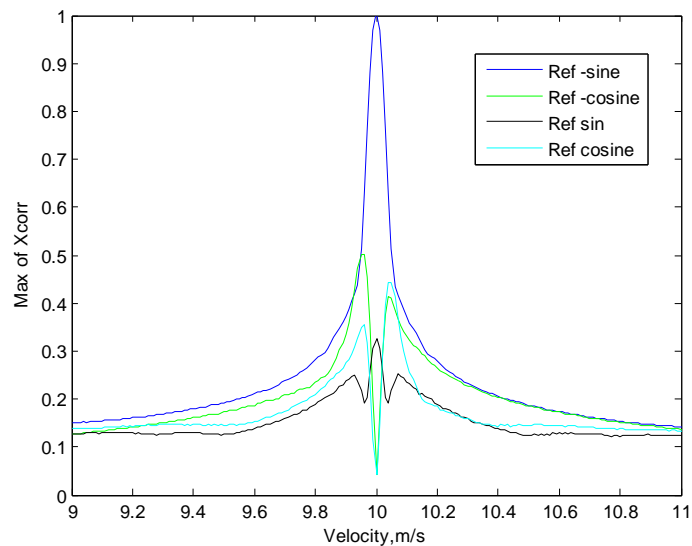


Figure 6.20 Max of XCORR versus speed for the four reference functions

Figure 6.21 shows the simulated target time domain signature with two different velocities combination and the XCORR versus speed. Figure 6.21(a) shows the time domain signature of the reference function –sine with 10m/s(red) and 11m/s(blue) in 50%:50%

combination. From Figure 6.21(b), the Maximum of XCORR versus the speed is plot for the estimation. It can be seen that the two peaks represent the two velocities at 10m/s and 11m/s. When we increase proportion for the 11m/s in the time domain (45%:55%), we can see from Figure 6.21(d) that the maximum of XCORR at the 11m/s is higher than the 10m/s. The result shows that when the target changes the speed when crossing the baseline, the speed estimation algorithm will detect the multiple peaks for the result.

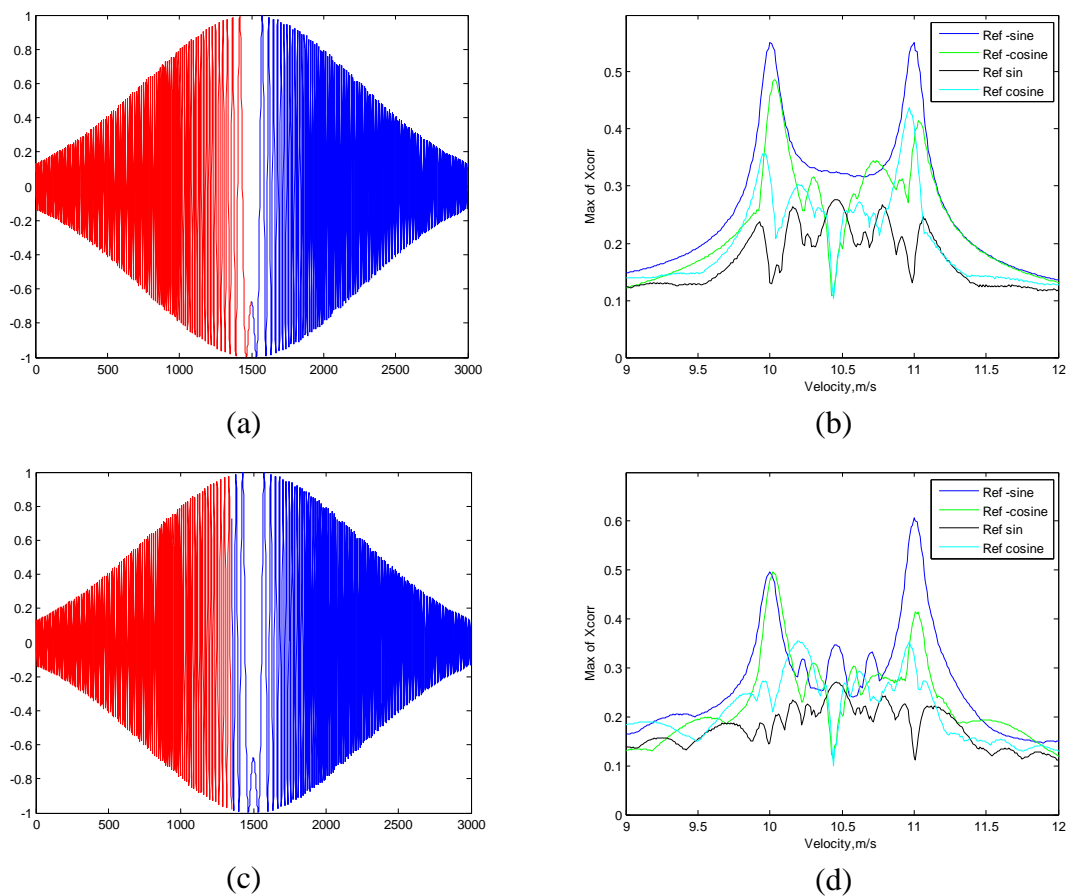


Figure 6.21 Simulated target signature and the Max of XCORR versus speed (a) Simulated target signal with 10m/s (red) and 11m/s (blue) in 50%:50% combination (b) XCORR versus speed of signature of (a) (c) Simulated target signal with 10m/s (red) and 11m/s (blue) in 45%:55% combination (d) XCORR versus speed

In reality, the target could not change the speed in a sharp step maneuver. Therefore, we simulate the target signature with the speed from 10m/s to 10.5m/s. The motion of the target keeping the speed constant at 10m/s at the first and end 10seconds. After 10 seconds,

the target accelerates with a step of 0.1m/s for 1 second. Then at 14 seconds, the target reaches the top speed 10.5m/s. Finally, the speed drops to 10m/s from 16 to 20seconds with the same step of 0.1m/s. The whole motion of the target is shown in Figure 6.22. The simulated time domain signature is shown in Figure 6.23.

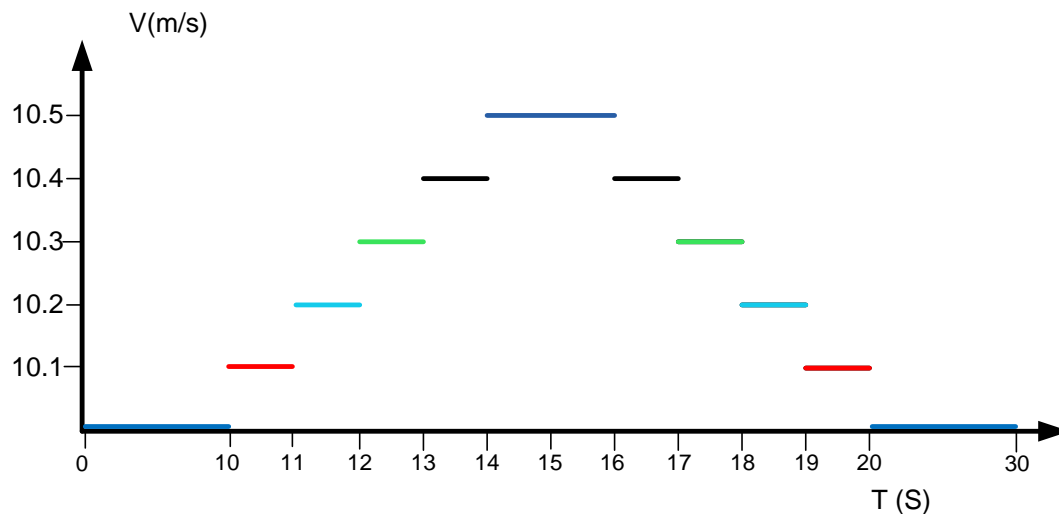


Figure 6.22 The speed versus the time scale in simulation

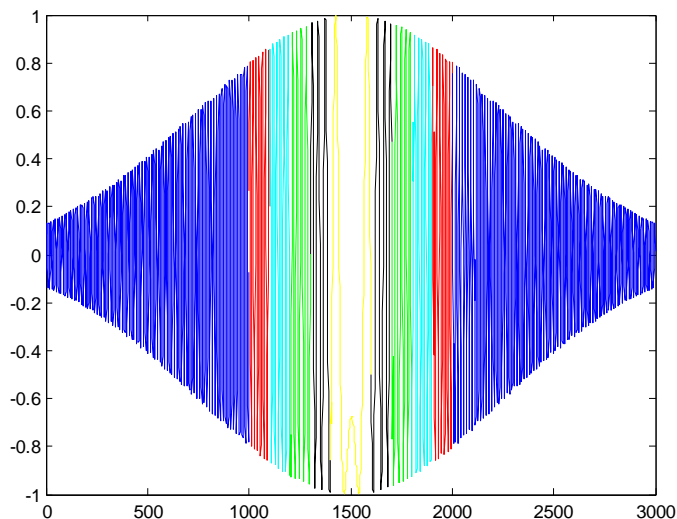


Figure 6.23 Time domain simulated signature

Figure 6.24 shows the Max of XCORR versus the velocity for the simulation signal. It is concluded that the $-\text{sine}$ reference function is the optimum reference function for the detection of the majority velocity 10m/s. However, the $-\text{cosine}$ reference function could be

used as the velocity estimation for the minor speed values 10.1m/s, 10.2m/s and so on.

Further investigation should be made for the improved speed estimation algorithm.

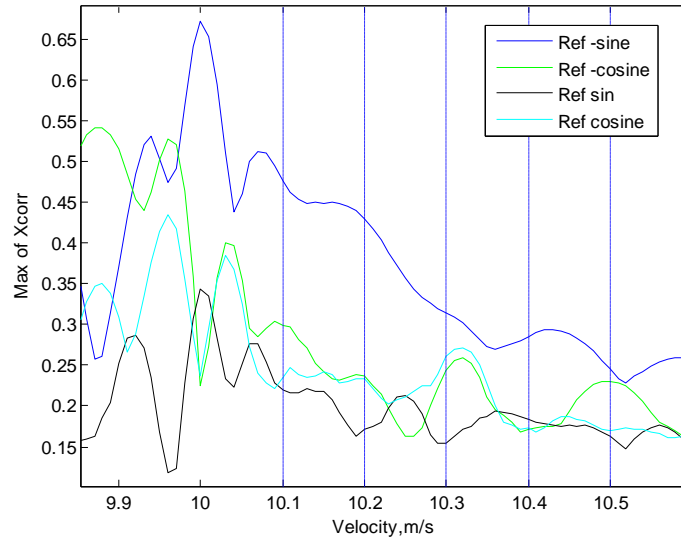


Figure 6.24 Max of XCORR versus speed

Next, the Automatic Slope calculation will be introduced and explained in detail. Figure 6.25 shows the algorithm implemented in the cross correlation and slope calculation procedure. The X-axis is the speed index range while the Y-axis is the Maximum Cross Correlation(MXC) values. We can find that the signature of the MXC versus speed has two main peaks: P1 and P2 which has two slopes upward and downward for each.

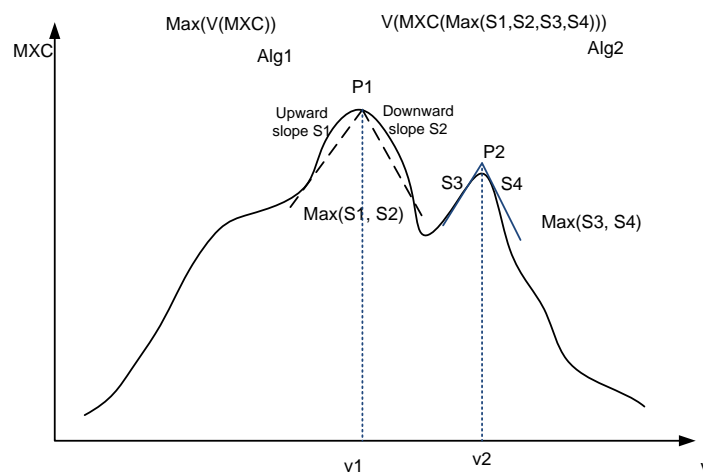


Figure 6.25 Algorithm for SE using max of cross correlation versus speed

From the comparison result of maximum of Peaks according to the algorithm 1, the V1 is chosen as the speed of the target. Assume slope S3 at P2 has the maximum value amount in the four slope values, the algorithm 2 will choose V2 as the speed of the target. Thirdly, if $S1 > S2$ in the P1, $S3 > S4$ in the P2, then first we find the maximum of slopes in each of the peaks and then compare the cross correlation values. V1 is the final target speed result at last.

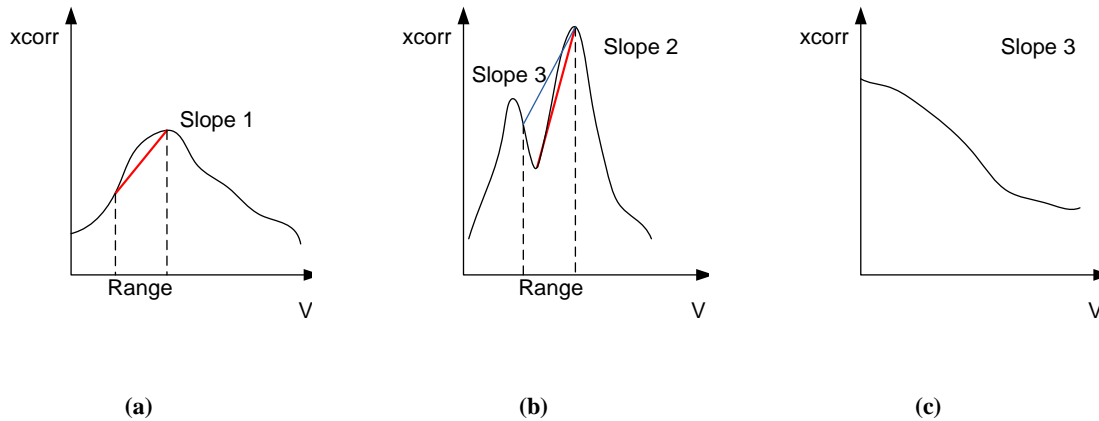


Figure 6.26 Upward slope calculation (a) Normal slope calculation (b) Upward region is less than the range (c) Without upward slope

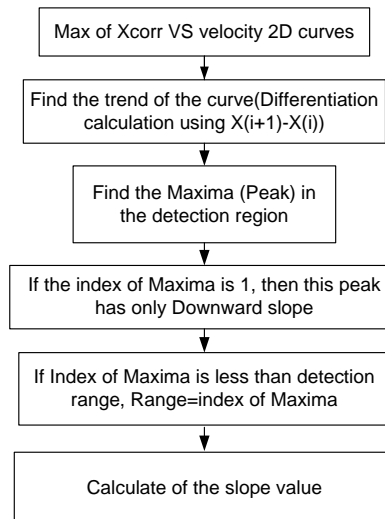


Figure 6.27 Slope calculation procedure

Many difficult conditions such as peak starting from signature beginning and lack of length of main peak lobe are also taken into consideration. This detection in most cases can adhere and coincide with the optimum reference function speed result, but in some cases, due to the slope calculation in the sophisticated trend of the signature, the peak main lobe is much

difficult to handle in the algorithm design and sometimes needs to be manually adjusted. Multi-peak detection is a possible solution to some miss estimated speed cases, such as in the peak vicinity and 8.9m/s is the expected speed of the target.

For the multi-peak detection, we pre-determined the peak detection level at the 20% off the maximum cross correlation values as the detection range. In detail, first of all, calculate the one run data and get the four reference function maximum of cross correlation versus the speed signature and get the peak value amount these four signatures, set the 20% off the peak value as the threshold and detect all the peaks above the threshold. The threshold level is set at the empirical value at the condition that the optimum speed index is within the vicinity of the peak values. However, the threshold can be set at other values from 10% to 30% and we want to investigate the effect of these parameters. These regions are automatic selected using the slope trend detection algorithm and will be applied to the large size database. Figure 6.28 shows one example of the SE threshold at the three levels. All the peaks in these peak regions and their max value between the upward and downward slope are properly detected and calculated. The threshold levels are chosen from 10% to 30% with step of 10% off the maximum of cross correlation result within the sine waveform reference functions.

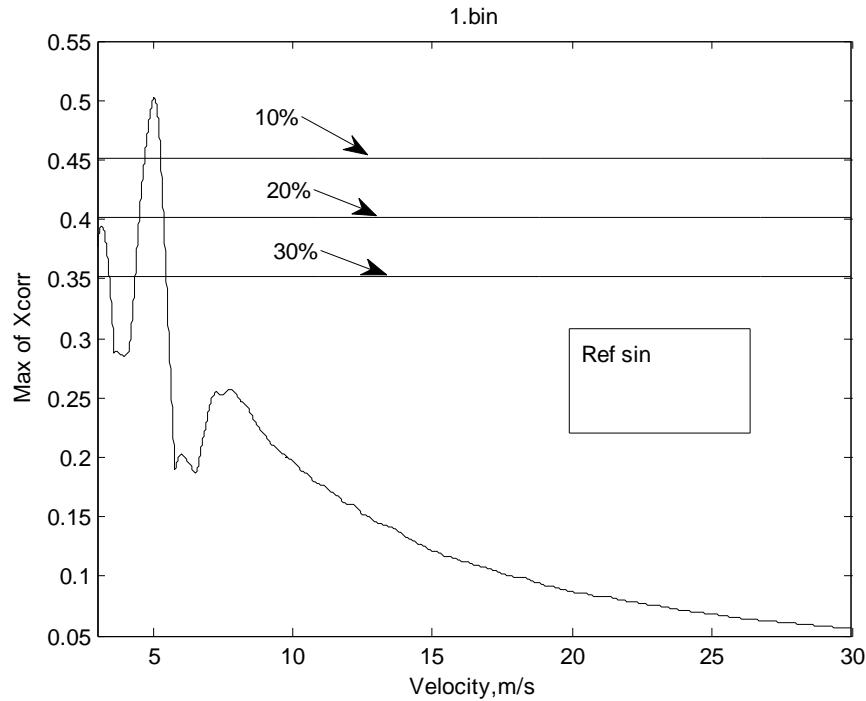


Figure 6.28 Multi peak detection levels

Table 6.8 shows all the RMSE values at the multiple peak detection using the database of Tilesford airfield and the RMSE values are indicating that the Multiple SE levels are having the same estimation errors, which means the speed are estimated as the same values in each reference function.

Table 6.8 64MHz RMSE values at multiple peak detection threshold

64MHz RMSE	Max of XCORR	Max of slope	Max of slope then XCORR
10%	17.7%	12.9%	17.7%
20%	17.7%	12.9%	17.7%
30%	17.7%	12.9%	17.7%

6.6.2 Fusion algorithm of slope and amplitude of cross correlation

Three main criteria is applied to the speed estimation, which are maximum of cross correlation named algorithm 1, maximum of slope values of peaks called algorithm 2, and

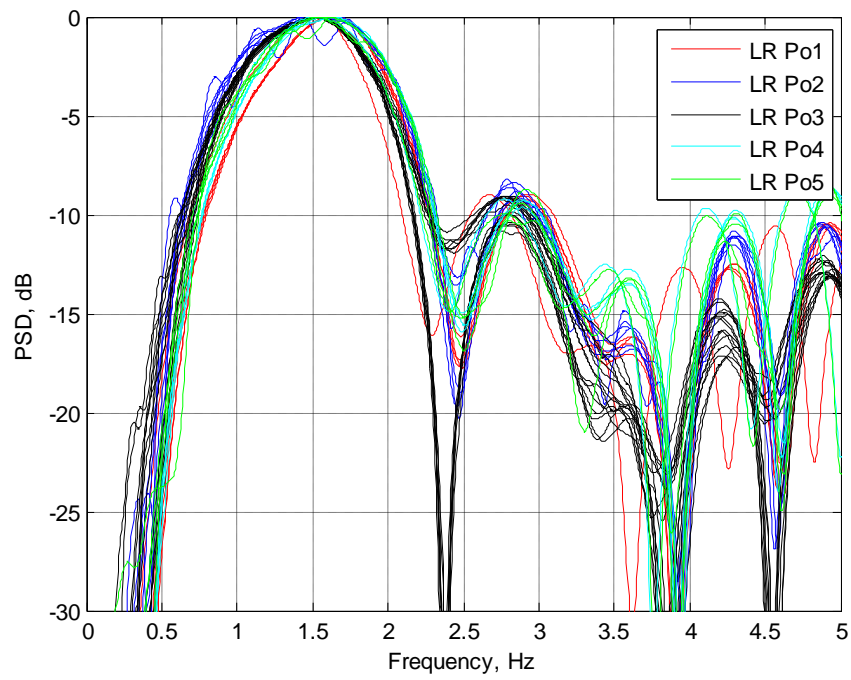
thirdly priority to detect the maximum of slope in each reference functions then compare the cross correlation values defined as algorithm 3.

Apply these three algorithms to the SE procedure in Tilesford airfield database, the speed accuracy is displayed in the Table 6.9 and the algorithm 2 and 3 can achieve lower RMSE values in some of the frequency channels.

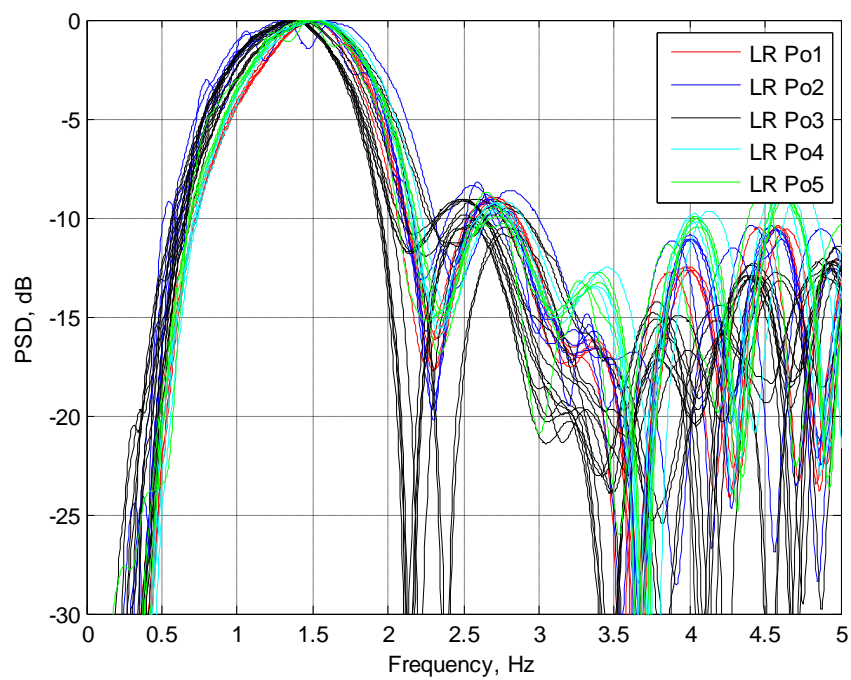
Table 6.9 SE RMSE values across the criteria and frequencies

Test site	Frequency	Max of cross correlation	Max of slope	1st max of slope and then cross correlation
Tilesford airfield	64MHz	5.3%	4%	4.6%
	135 MHz	5.3%	4.8%	5.1%
	144 MHz	6%	4%	5%
	151 MHz	4%	8%	7%
	173 MHz	6.1%	5%	4.2%
	434 MHz	8.4%	7%	6%

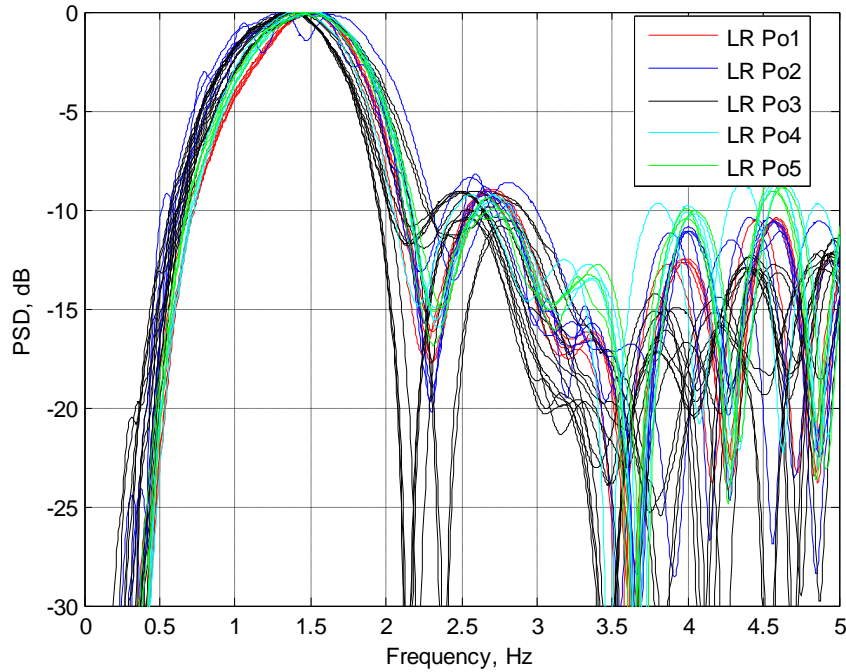
Figure 6.29 illustrates all the 434MHz speed normalization results in PSD frequency domain at Tilesford airfield. We can find that all of the frequency channels database have highly repeatable signatures in the PSD domain and it is proved to be a possible source for the target classification purpose.



(a)



(b)



(c)

Figure 6.29 PSD plot after speed normalization 434MHz channel (a) Max of cross correlation (b) Max of slope (c) Max of slope and then cross correlation

So far, we have obtained the improved SE algorithm considering only the maximum of cross correlation and slope value independently; the next step is to incorporate these two factors for further improvement of the algorithm. The criterion for SE algorithm is given by using the equation (6.8) and the normalization format shown in the equation (6.9).

$$\max[slope \times a + xcorr \times (1 - a)] \quad (6.8)$$

$$\max\left[\frac{slope \times a}{\max(slope)} + \frac{xcorr \times (1 - a)}{\max(xcorr)}\right] \quad (6.9)$$

where a is from 0 to 1, with step of 0.1. If $a=0$, it corresponds to the maximum of XCORR, else if $a=1$, it uses the maximum of slope as the criteria.

While both the XCORR and slope are non-normalized value. The Tilesford airfield results are listed in the Table 6.10. The RMSE value with star signs indicates the least SE error amount the factors.

Table 6.10 Tilesford airfield SE RMSE values

Factor \ Freq	0	0.1	0.2	0.3	0.4	0.5	0.6	0.7	0.8	0.9	1
64MHz	5.32%	5.32%	5.32%	5.29%	5.36%	5.01%	5.04%	4.93%	4.98%	4.79%	4.66%*
135MHz	7.19%	6.51%	5.50%	4.96%	4.61%*	4.94%	4.93%	4.96%	4.96%	4.96%	4.86%
144MHz	6.71%	5.40%	5.13%	4.77%	4.47%	4.35%	4.23%	4.14%	4.14%	4.10%	4.10%*
151MHz	5.00%	5.00%	5.10%	5.08%	4.84%	4.80%	4.64%	4.22%	4.22%	4.20%*	4.21%
173MHz	6.07%	6.07%	6.01%	5.91%	6.27%	6.11%	5.43%*	5.43%	5.58%	5.58%	5.63%
434MHz	7.30%	6.42%	5.12%	5.01%	4.68%	4.57%	4.59%	4.67%	4.66%	4.39%	4.39%*

There is very limited improvement by applying factors in the SE algorithm, minimum with 0.66% in 64MHz channel and maximum with 2.91% in the 434MHz channel. Therefore, we will only apply the maximum of XCORR and maximum of slope as the main criterion in the signal processing procedures.

6.6.3 Pritchatts car park database evaluation

The three SE algorithms are applied to the Pritchatts car par database and Table 6.11 shows all the SE normalization result in the PSD frequency domain. While the Table 6.12 provides the SE RMSE values for the three criteria. It is concluded that the low accuracy is presented higher than 10% and 20% in 64MHz and 135MHz while the lowest RMSE is acquired from the 434MHz frequency channel by using the maximum of slope criterion, which is less than 10%. The unacceptable RMSE value of 150% and 137% by using the algorithm 1 and 2 are not suitable for target recognition. The XCORR versus the speed charts can be seen in Appendix C.

Table 6.11 PSD speed normalization result for Pritchatts car park

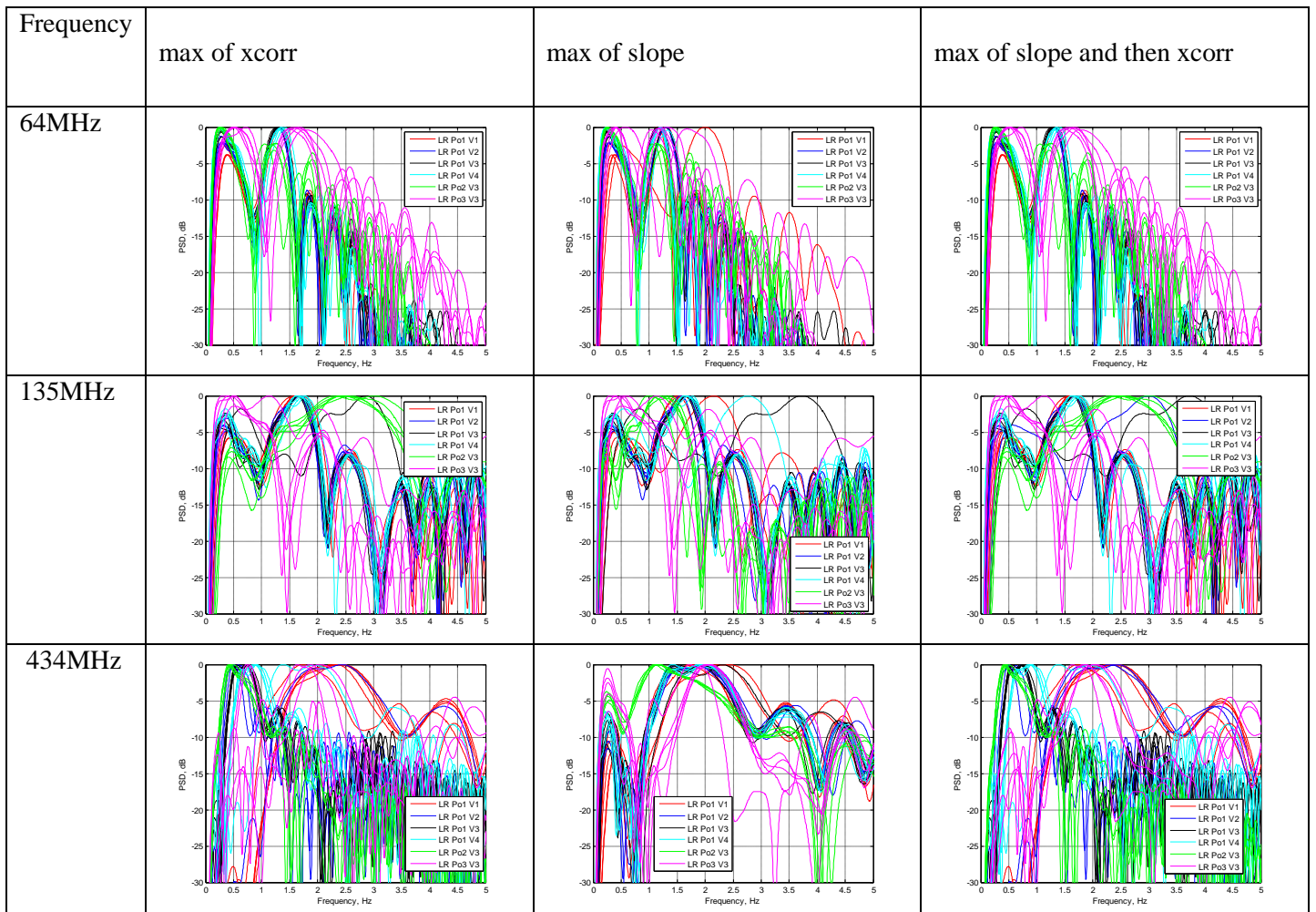


Table 6.12 SE RMSE values

Test site	Frequency	Max of cross correlation	Max of slope	Max of slope and then cross correlation
Pritchatts car park	64MHz	17.7%	12.9%	17.7%
	135MHz	27.7%	21.3%	29.8%
	434MHz	150%	7%	137%

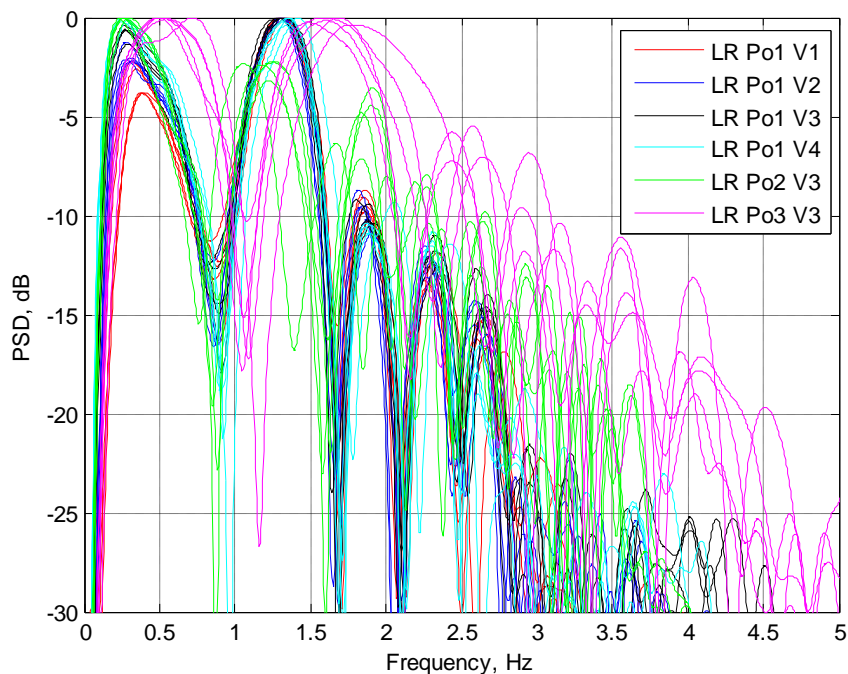
The fusion algorithm is also applied in the three frequency channels 64MHz, 135MHz, 434MHz and Table 6.13 shows the RMSE values for each frequency using the fusion factors from 0 to 1 with step of 0.1.

Table 6.13 Pritchatts car park SE RMSE values

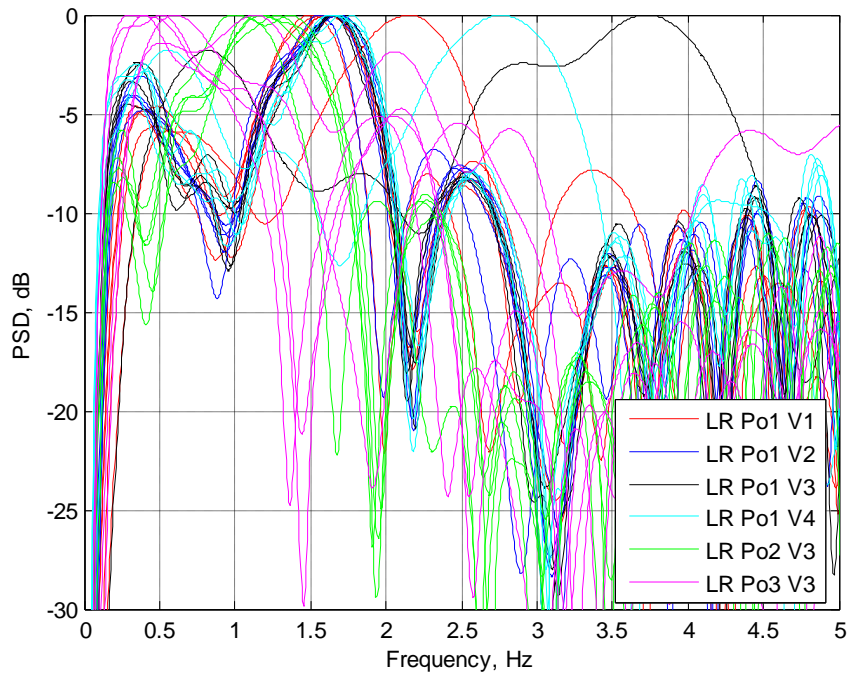
Factor \ Frequency	0	0.1	0.2	0.3	0.4	0.5	0.6	0.7	0.8	0.9	1
64MHz	17.70%	18.20%	15.19%	12.91%	11.64%	11.24%	11.01%*	13.08%	13.46%	13.09%	12.98%
135MHz	27.81%	26.54%	20.64%	15.24%	17.20%	17.17%	17.17%*	20.18%	20.86%	20.86%	21.35%
434MHz	150.70%	109.99%	83.87%	74.16%	65.92%	58.65%	7.13%*	7.30%	7.30%	7.22%	7.22%

From

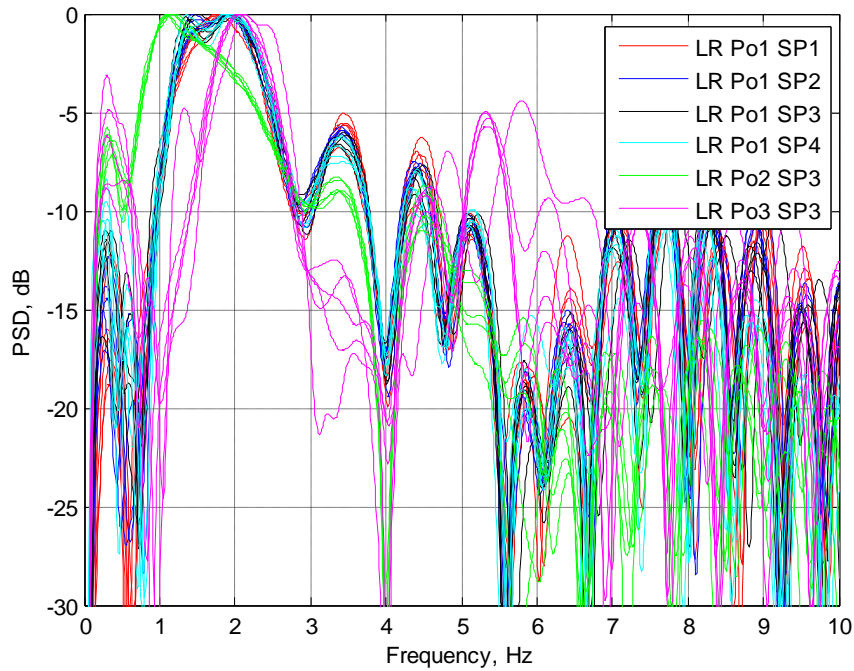
Table 6.13, it shows the optimum factor is 0.6 for all the three frequency channels, and the lowest RMSE value can be controlled below 10%. Then we applied the proportion factor to the speed normalization algorithm and get the PSD signatures for the three frequency channels shown in Figure 6.30.



(a)



(b)



(c)

Figure 6.30 The optimum speed normalization result using 0.6 factor (a) 64MHz (b) 135MHz (c) 434MHz

6.7 Conclusion

In this chapter, The Tilesford airfield and Pritchatts car park speed normalization result have been processed. From the PSD speed normalization of Tilesford airfield, it is shown that the PSD signatures are highly repeatable with each other after the speed normalization algorithm. In addition, the frequency channels used in the experiments can be processed by the sophisticated signal processing block diagram. The SE algorithm is also investigated using sophisticated slope calculation to improve the accuracy of result and the max slope within the interested zone is considered as an effective way to estimate the speed especially for the sophisticated test site higher frequency RSSI channel such at 434MHz. However, the new multiple 90 degree shift reference functions prevail in the SE algorithm.

Chapter 7 Summaries and future work

7.1 Summaries

In this thesis, the research on the automatic target detection and speed estimation program using FSR system has been performed. The modelling of the reception target signature, the RCS analysis utilizing the CST, the CW radar system is carefully evaluated by the experimental real recorded database.

The novelty of the thesis arises from the bistatic radar deployment; the major contribution of the work is to the finding of the half pi phase shift reference functions for universal frequency channels and the improved accuracy of speed estimation. Comparison of max of slope, max of XCORR and fusion of two criterion for ground target speed estimation in a coherent way is applied. The detection algorithm is the preprocessing for the further procedure in the target classification stage. The PSD signature analysis can be utilized at this stage.

The MonteCarlo simulation is applied in the target detection algorithm and so did the short-time wave form analysis. It effectively traces and locates the exact point when the target's trajectory joint point with the baseline, and the approximate time domain of the target motion is estimated.

In addition, it is also suggested that the more complex the surface ground, the more sophisticated the algorithm should design should be. The clutter from the ground vegetation or large obstacle within the scenario should be taken into consideration and the accuracy of the speed estimation and normalization will be affected.

The modified speed estimation algorithm is to automatically process the short time target signatures. It is post processing of the real time signal processing after the target fully crosses the baseline and fades completely out of the forward scatter region. Due to the dimension and shape of the large vehicle target, the side lobe and main lobe of the reception signals should be considered in three stages and each stage gives the major electromagnetic field change of the zone.

Experiments were carried out using the FSR system and the complexity of environments are classified as open airfield with little multipath effect and the more sophistic vegetation surroundings at Pritchatts car park.

7.2 Future work

After exploring the study on the target detection and speed estimation in the GFSR system, the main goal of this thesis has been achieved. For better target probability of detection and higher speed estimation accuracy result, much work has been done on these two directions. However, the word research is a combination of ‘re’ and ‘search’, which means the end of the research could be a new starting point. The future work could be developed with the following directions:

The feasibility of the multi FSR sensor network could be taken into investigation for the further development. It requires the interference isolation receiving technology and encoding algorithm to identify the transmitted signal in the real environment. Multistatic radar network is the next generation radar fusion technology.

The MIMO technology could be employed in the GFSR system to obtain the higher resolution target classification. The higher frequency band could be employed for the more detailed target resolution purpose.

Chapter 7 Summaries and future work

The multipath evaluation experiment should be carried out in more complex environments. Vegetation or the concrete walls could be surrounded to form this environment in future tests.

The target classification algorithm could be investigated to find a better classifier. The neural network or compress sense technology is fast growing in this decade and these are the potential tools for the GFSR systems.

Chapter 8 Reference

- [1] B. Edde, *Radar: Principles, Technology, and Applications*. Prentice Hall PTR, 1993.
- [2] A. J. Bogush, *Radar and the atmosphere*. Artech House, Incorporated, 1989.
- [3] M. I. Skolnik, "Radar Handbook." McGraw-Hill Professional, 1990.
- [4] M. Cherniakov, *Bistatic Radar: Principles and Practice*. Wiley, 2007.
- [5] N. J. Willis, *Bistatic Radar*. SciTech Publishing Inc, 2005.
- [6] L. Brown, "Technical and Military Imperatives: a Radar History of World War II." Taylor & Francis, 1999.
- [7] H. Griffiths and N. Willis, "Klein Heidelberg-The First Modern Bistatic Radar System," *Aerosp. Electron. Syst. IEEE Trans.*, vol. 46, no. 4, pp. 1571–1588, 2010.
- [8] "Air Scientific Intelligence Interim Report ELEFANT— German KH." 1945.
- [9] "Report on ELEFANT Radar on Romo, Denmark, with Additional Notes on Heidelberg," *TRE Rep. T1906 (AVIA 26/908)*, 1945.
- [10] E. A. SLOANE CANDIDUS, E.S., SALERNO, J., and SKOLNIK, and M., "A bistatic CW radar," MIT Lincoln Laboratory, 1955.
- [11] M. I. Skolnik, "Fifty years of radar," *Proc. IEEE*, vol. 73, no. 2, pp. 182–197, 1985.
- [12] F. R. N. and W. W. Ward, "Distant Early Warning Line Radars: The Quest for Automatic Signal Detection," *LINCOLN Lab. J.*, vol. 12, pp. 181–204, 2000.
- [13] M. D. H. Thorne, "The Mid Canada Line."
- [14] B. K. Shembe, "The origin of radiolocation in the USSR," *Sov. Radio, Moscow*, 1977.
- [15] A. PRICE, "The development of radar in Japan, to the end of World War II," *Hist. US Electron. Warf.*, pp. 289–293, 1984.
- [16] A. P. Whitewood, C. J. Baker, and H. D. Griffiths, "Bistatic radar using a spaceborne illuminator," in *Radar Systems, 2007 IET International Conference on*, 2007, pp. 1–5.
- [17] P. E. Howland, "Target tracking using television-based bistatic radar," *Radar, Sonar Navig. IEE Proc.* -, vol. 146, no. 3, pp. 166–174, 1999.

- [18] M. Kubica, V. Kubica, X. Neyt, J. Raout, S. Roques, and M. Acheroy, "Optimum target detection using illuminators of opportunity," in *Radar, 2006 IEEE Conference on*, 2006, p. 8 pp.
- [19] D. W. O'Hagan and C. J. Baker, "Passive Bistatic Radar (PBR) using FM radio illuminators of opportunity," in *New Trends for Environmental Monitoring Using Passive Systems, 2008*, 2008, pp. 1–6.
- [20] B. Sobhani, E. Paolini, A. Giorgetti, M. Mazzotti, and M. Chiani, "Target Tracking for UWB Multistatic Radar Sensor Networks," *Sel. Top. Signal Process. IEEE J.*, vol. 8, no. 1, pp. 125–136, 2014.
- [21] K. M. SIEGEL, "Bistatic radars and forward scattering," *Proceedings of Natl. Conf. Aeronaut. Electron.*, pp. 286–290, 1958.
- [22] D. M. Gould, R. S. Orton, and R. J. E. Pollard, "Forward scatter radar detection," in *RADAR 2002*, 2002, pp. 36–40.
- [23] H. D. Griffiths and C. J. Baker, "Passive coherent location radar systems.," *IEE Proceedings-Radar, Sonar Navig.*, vol. 152, pp. 153–159, 2005.
- [24] M. C. Jackson, "The geometry of bistatic radar systems," *Commun. Radar Signal Process. IEE Proc. F*, vol. 133, no. 7, pp. 604–612, 1986.
- [25] P. Y. Ufimtsev, "Comments on diffraction principles and limitations of RCS reduction techniques," *Proc. IEEE*, vol. 84, no. 12, pp. 1830–1851, 1996.
- [26] A. L. F. and K. D. Mease, "Mie forward scattering: improved semiempirical approximation with application to particle size distribution inversion," *Appl. Opt.*, vol. 20, no. 2, pp. 194–198, 1981.
- [27] S. E. A. PINNELL, "Stealth aircraft," *Aviat. Sp. Technol.*, 1981.
- [28] M. Cherniakov, M. Salous, V. Kostylev, and R. Abdullah, "Analysis of forward scattering radar for ground target detection," in *Radar Conference, 2005. EURAD 2005. European*, 2005, pp. 145–148.
- [29] V. Sizov, M. Cherniakov, and M. Antoniou, "Forward scattering radar power budget analysis for ground targets," *Radar, Sonar Navig. IET*, vol. 1, no. 6, pp. 437–446, 2007.
- [30] M. Antoniou, V. Sizov, H. Cheng, P. Jancovic, R. Abdullah, N. E. A. Rashid, and M. Cherniakov, "The concept of a forward scattering micro-sensors radar network for situational awareness," in *Radar, 2008 International Conference on*, 2008, pp. 171–176.
- [31] L. Daniel, M. Gashinova, and M. Cherniakov, "Maritime UWB forward scattering radar network: Initial study," in *Radar, 2008 International Conference on*, 2008, pp. 658–663.

- [32] L. Y. Daniel, E. G. Hoare, M. Gashinova, A. Svintsov, M. Cherniakov, and V. Sizov, "Ultra-wideband forward scatter radar fence for maritime surveillance - Initial experimental results," in *Radar Conference, 2010 IEEE*, 2010, pp. 526–531.
- [33] K. Kabakchiev, L. Y. Daniel, V. Sizov, E. Hoare, M. Gashinova, and M. Cherniakov, "Received signal characterization in forward scatter radar for maritime application," in *Radar Symposium (IRS), 2011 Proceedings International*, 2011, pp. 67–72.
- [34] C. Kabakchiev, I. Garvanov, V. Behar, A. Kabakchiev, and D. Kabakchieva, "Forward scatter radar detection and estimation of marine targets," in *Radar Symposium (IRS), 2012 13th International*, 2012, pp. 533–538.
- [35] C. Kabakchiev, I. Garvanov, V. Behar, and H. Rohling, "The experimental study of possibility for radar target detection in FSR using L1-based non-cooperative transmitter," in *Radar Symposium (IRS), 2013 14th International*, 2013, vol. 2, pp. 625–630.
- [36] C. Kabakchiev, I. Garvanov, M. Cherniakov, M. Gashinova, V. Behar, A. Kabakchiev, and V. Kiovtorov, "Bistatic UWB FSR CFAR for maritime target detection and estimation in the frequency domain," in *Radar Symposium (IRS), 2011 Proceedings International*, 2011, pp. 73–78.
- [37] H. Kabakchiev, D. Kabakchieva, M. Cherniakov, M. Gashinova, V. Behar, and I. Garvanov, "Maritime target detection, estimation and classification in Bistatic ultra wideband forward scattering radar," in *Radar Symposium (IRS), 2011 Proceedings International*, 2011, pp. 79–84.
- [38] K. Kabakchiev, L. Y. Daniel, E. G. Hoare, M. Gashinova, and M. Cherniakov, "Near zero grazing angle forward-scatter sea clutter measurement statistical properties," in *Radar Symposium (IRS), 2013 14th International*, 2013, vol. 2, pp. 620–624.
- [39] R. S. A. B. R. Abdullah, "Forward Scattering Radar for Vehicle Classification," University of Birmingham, Birmingham, 2005.
- [40] N. E. B. A. Rashid, "Automatic vehicle classification in a low frequency forward scatter micro-radar," University of Birmingham, Birmingham, 2011.
- [41] C. Xu, "Latest velocity estimation and normalization result of the ground forward scatter radar system," in *Radar Conference 2013, IET International*, 2013, pp. 1–4.
- [42] H. G. Booker, "Slot aerials and their relation to complementary wire aerials (Babinet's principle)," *J. Inst. Electr. Eng. - Part IIIA Radiolocation*, vol. 93, no. 4, p. 620, 1946.
- [43] S. Kingsley and S. Quegan, *Understanding Radar Systems*. Institution of Engineering and Technology, 1999.

- [44] T. Zeng, X. Li, C. Hu, and T. Long, "Investigation on accurate signal modelling and imaging of the moving target in ground-based forward scatter radar," *Radar, Sonar Navig. IET*, vol. 5, no. 8, pp. 862–870, 2011.
- [45] H. Cheng, V. Sizov, M. Antoniou, M. Gashinova, and M. Cherniakov, "Optimal Signal Processing in Ground-Based Forward Scatter Micro Radars," *Aerosp. Electron. Syst. IEEE Trans.*, vol. 48, no. 4, pp. 3006–3026, 2012.
- [46] V. Sizov, M. Cherniakov, and M. Antoniou, "Forward scattering radar power budget analysis for ground targets," *Radar, Sonar Navig. IET*, vol. 1, no. 6, pp. 437–446, 2007.
- [47] M. Sauter, *From GSM to LTE: An Introduction to Mobile Networks and Mobile Broadband*. 2010.
- [48] "<http://www.radiometrix.com/>."
- [49] S. Makarov, *Antenna and EM Modeling with Matlab*, no. v. 1. Wiley, 2002.
- [50] "434MHz YAGI Antenna Data Sheet," p. 709418, 2012.
- [51] "http://en.wikipedia.org/wiki/Probability_density_function."
- [52] Mathworks, "<http://uk.mathworks.com/help/stats/normpdf.html>."
- [53] J. V. W. L. R. DiFranco, *Radar Detection (Scitech Radar and Defense)*. 2004.
- [54] "http://en.wikipedia.org/wiki/False_alarm."
- [55] Mathworks, "<http://uk.mathworks.com/help/signal/ref/butter.html>."
- [56] MathWorks, "<http://uk.mathworks.com/help/signal/ref/hamming.html>."
- [57] A. R. Webb and K. D. Copsey, *Statistical Pattern Recognition*. Wiley, 2011.
- [58] L. Homogeneity, "History of Nonlinear Principal Component," pp. 1–14, 1949.
- [59] N. E. A. Rashid, M. Antoniou, P. Jancovic, V. Sizov, R. Abdullah, and M. Cherniakov, "Automatic target classification in a low frequency FSR network," in *Radar Conference, 2008. EuRAD 2008. European*, 2008, pp. 68–71.
- [60] S. Chi Hyung and J. T. Yen, "The effect of different cross-correlation methods on the dual apodization with cross-correlation algorithm," in *Ultrasonics Symposium, 2008. IUS 2008. IEEE*, 2008, pp. 978–981.

- [61] R. Daher and R. Adve, "A Notion of Diversity Order in Distributed Radar Networks," *Aerosp. Electron. Syst. IEEE Trans.*, vol. 46, no. 2, pp. 818–831, 2010.
- [62] J. I. Glaser, "Some results in the bistatic radar cross section (RCS) of complex objects," *Proc. IEEE*, vol. 77, no. 5, pp. 639–648, 1989.
- [63] Y. Liu and Q. Wan, "Sidelobe Suppression for Robust Capon Beamforming With Mainlobe-to-Sidelobe Power Ratio Maximization," *Antennas Wirel. Propag. Lett. IEEE*, vol. 11, pp. 1218–1221, 2012.
- [64] H. J. F. Moen, S. Kristoffersen, and T. Sparr, "Improved radar detection using evolutionary optimised filter," *Radar, Sonar Navig. IET*, vol. 6, no. 9, pp. 803–812, 2012.
- [65] C. H. Teng Long Cherniakov Mikhail, "Ground moving target signal model and power calculation in forward scattering micro radar," *Sci. China Ser. F Inf. Sci.*, vol. 52, no. 9, p. 11, 2009.
- [66] H. L. Van Trees, *Detection, Estimation, and Modulation Theory*. New York: Wiley, 1971.
- [67] A. K. Bhattacharyya and D. L. Sengupta, *Radar cross section analysis and control*. Artech House, 1991.

Chapter 9 Appendix

Appendix A RCS simulation result

RCS simulation result for the ground vehicle target Landrover

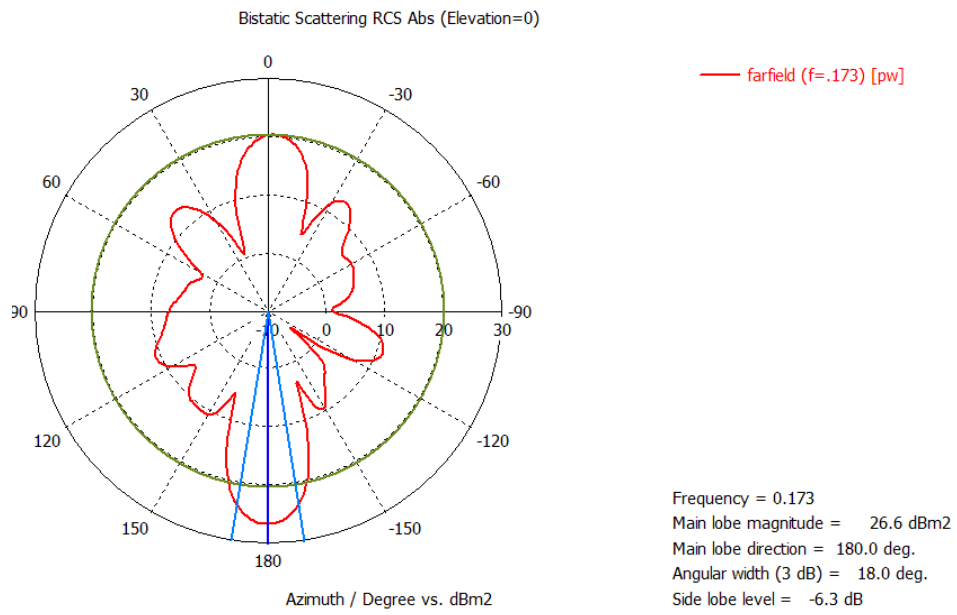


Figure 9.1 Bistatic scatter RCS in 173MHz

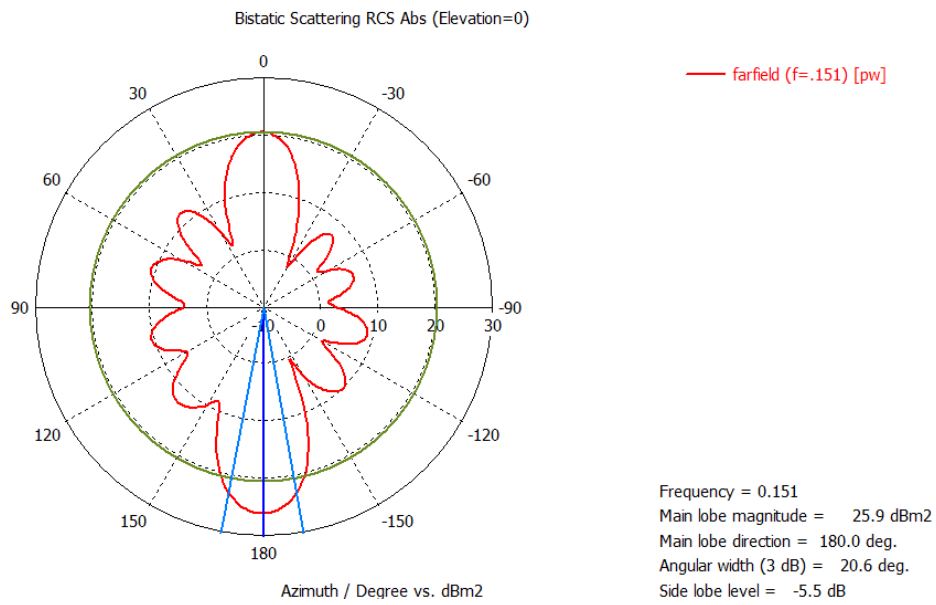


Figure 9.2 Bistatic scatter RCS in 151MHz

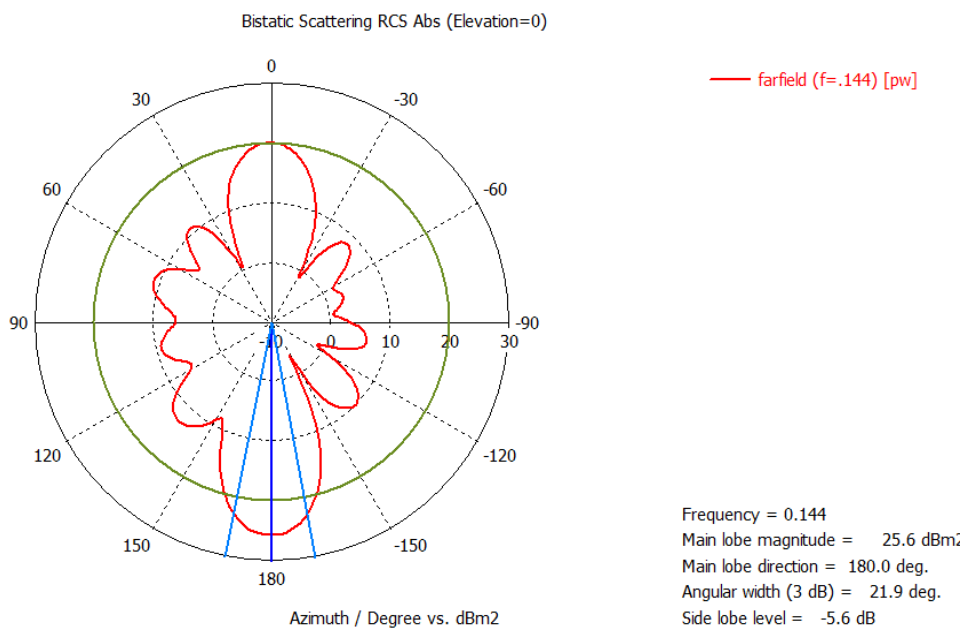


Figure 9.3 Bistatic scatter RCS in 144MHz

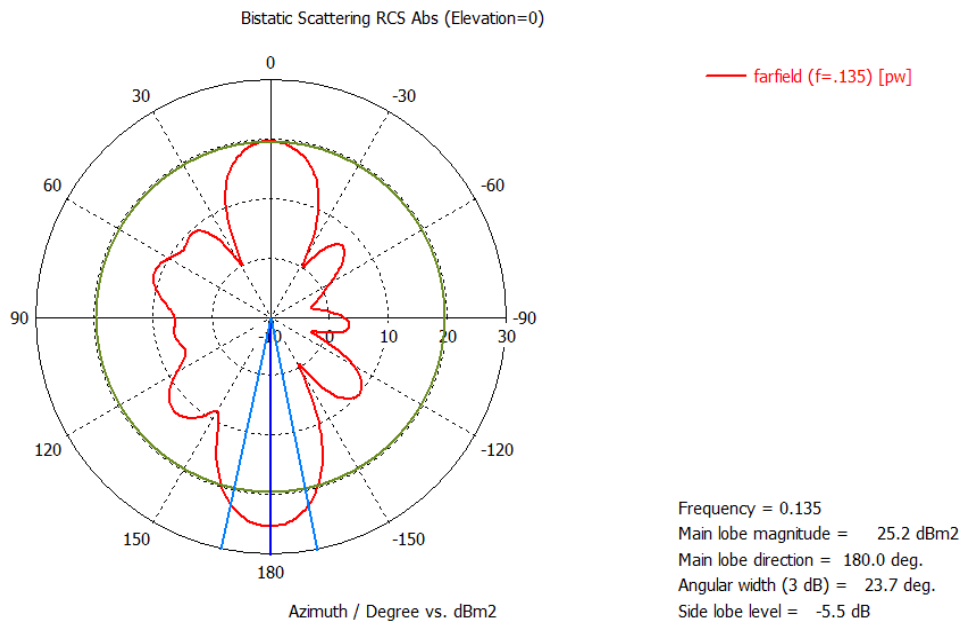


Figure 9.4 Bistatic scatter RCS in 135MHz

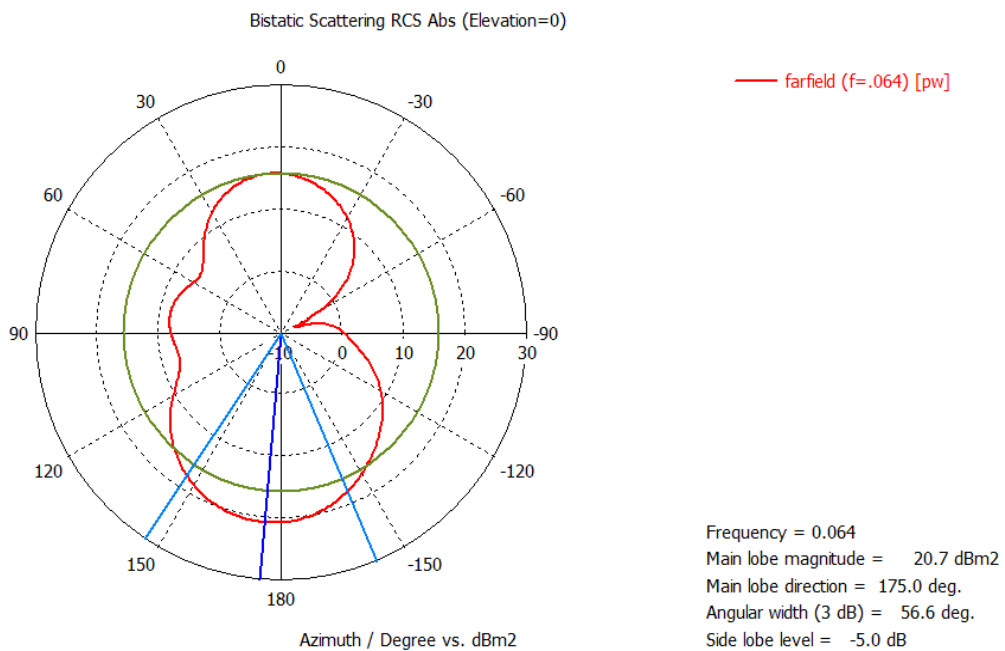


Figure 9.5 Bistatic scatter RCS in 64MHz

Appendix B Some result of STFT

Some of the typical STFT result with the time domain signal, 434MHz directional antenna Channel:

1

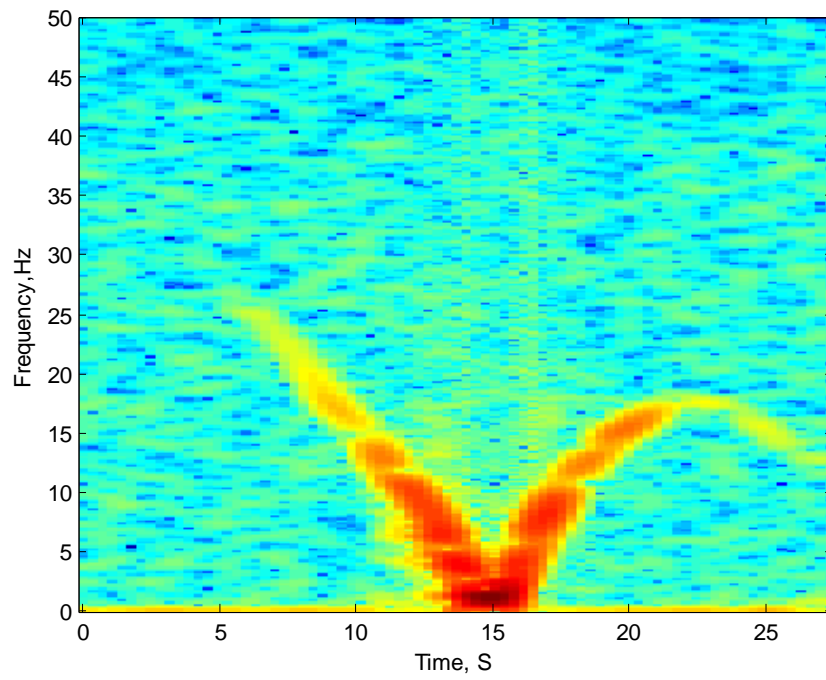


Figure 9.6 STFT signature 434MHz

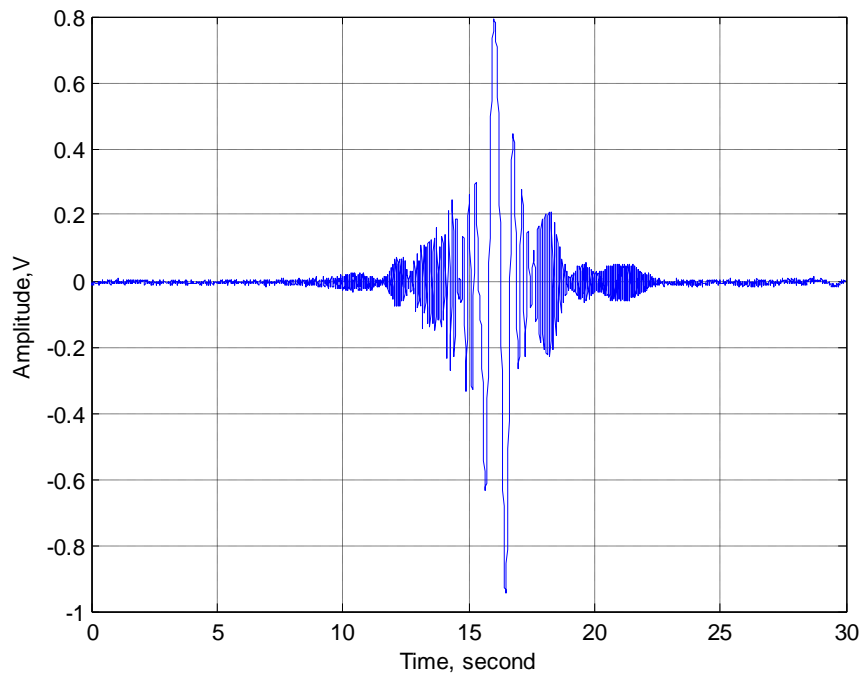


Figure 9.7 Time domain signature 434MHz

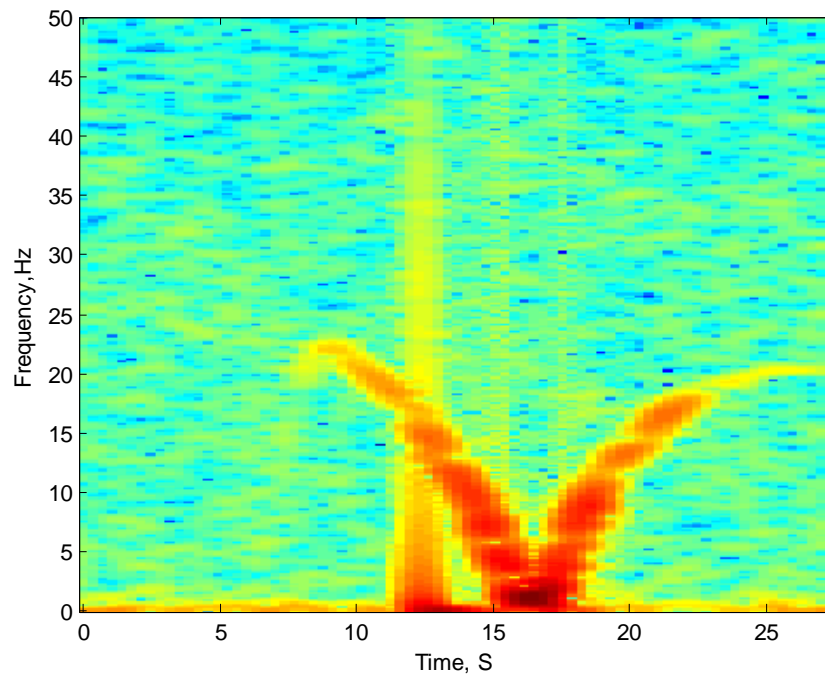


Figure 9.8 STFT signature 434MHz

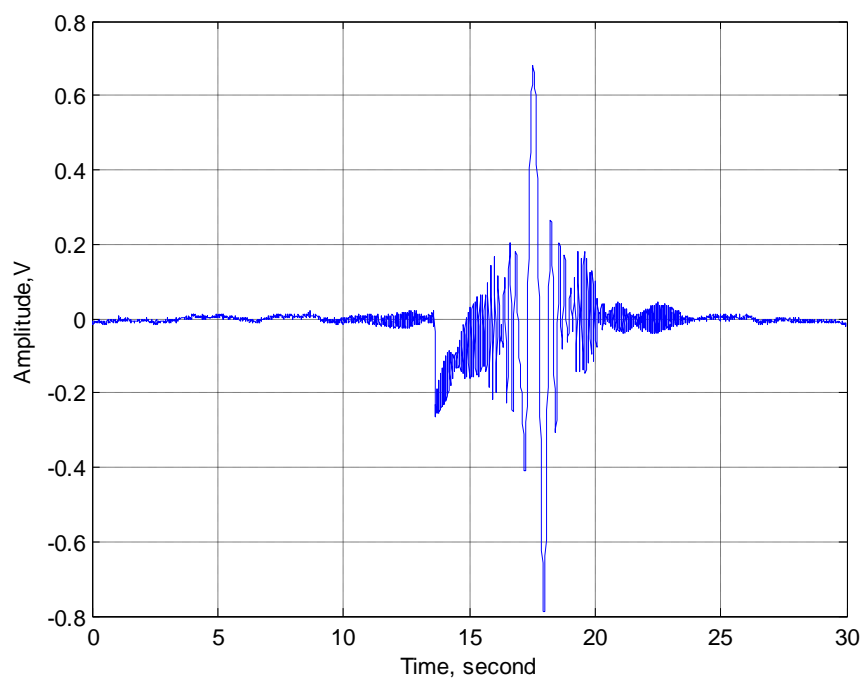


Figure 9.9 Time domain signature 434MHz

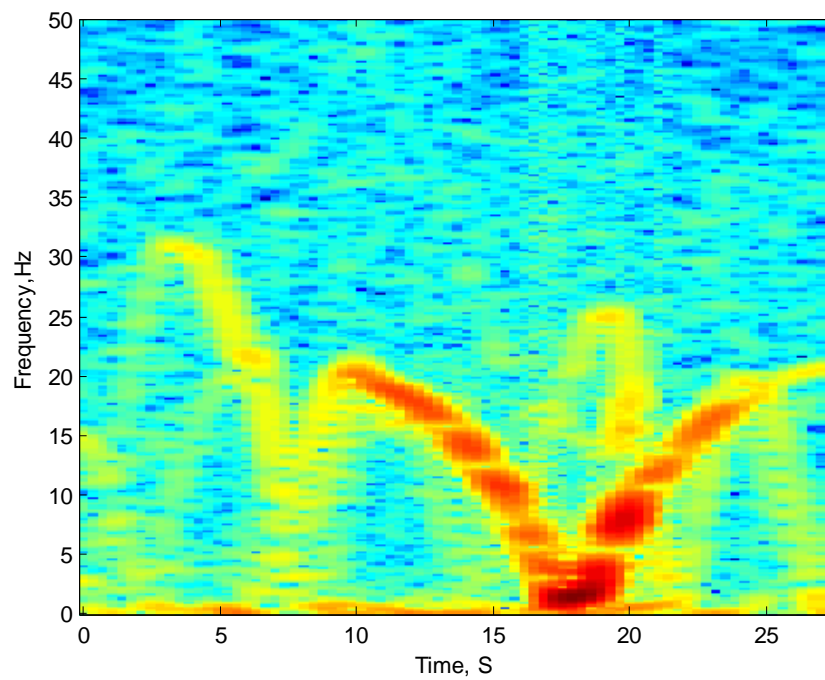


Figure 9.10 STFT signature 434MHz

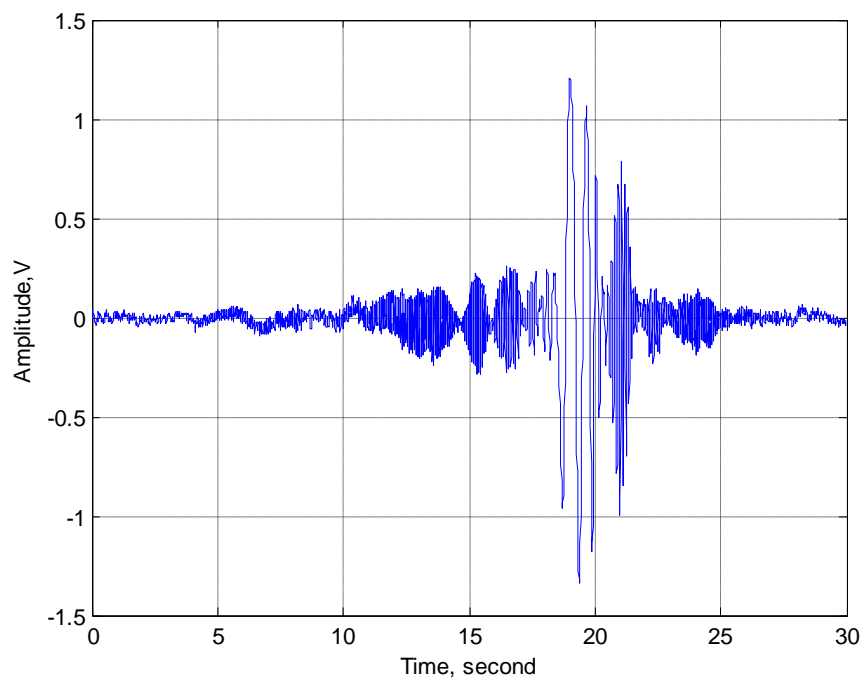
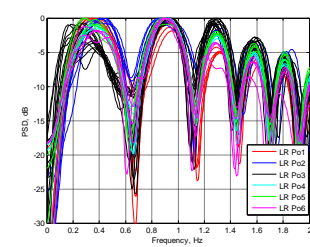
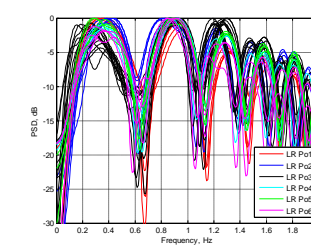
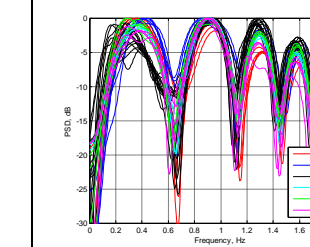
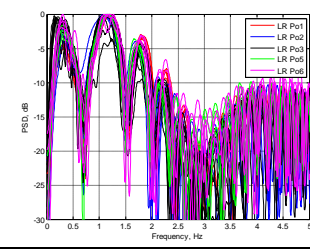
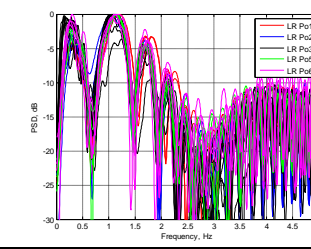
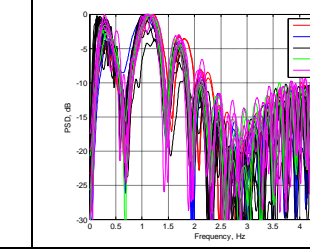
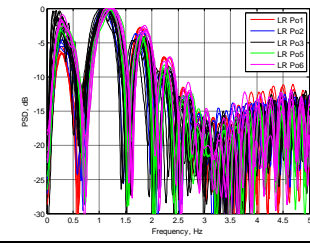
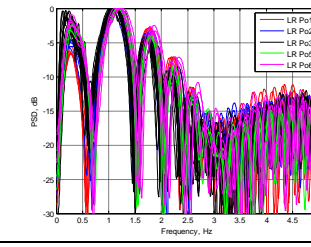
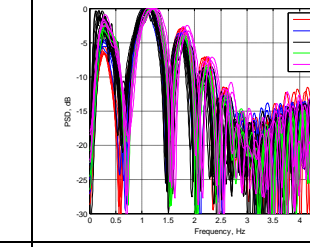
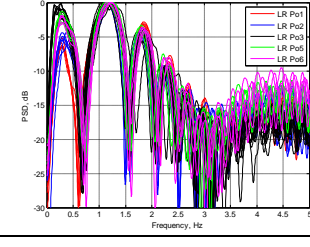
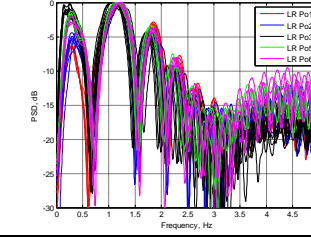
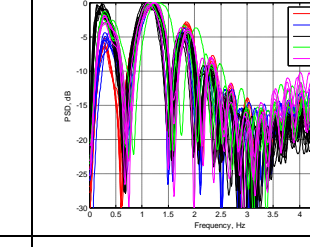
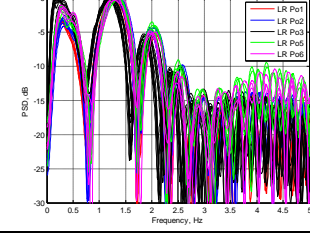
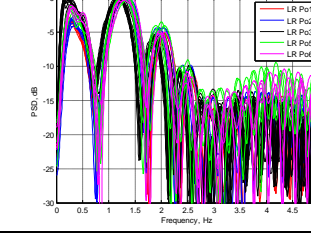
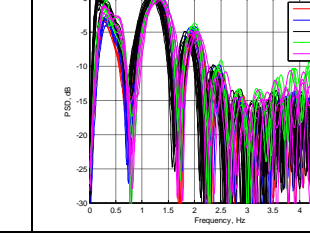


Figure 9.11 Time domain signature 434MHz

Appendix C Speed normalization result

Speed normalization result

Table 9.1 Comparison of speed normalization result in frequency domain for the Tilesford airfield

Channel	Max of cross correlation	Max of slope	Max of slope and then cross correlation
64MHz			
135MHz			
144MHz			
151MHz			
173MHz			

Chapter 9 Appendix

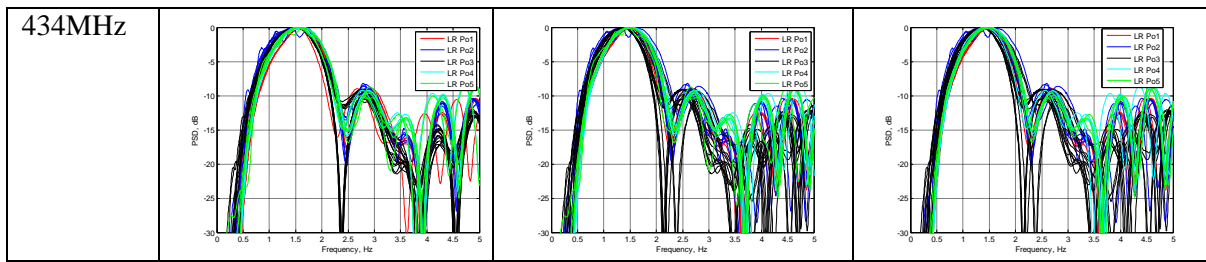
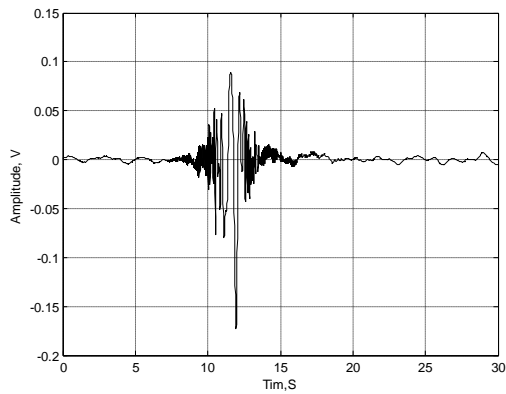
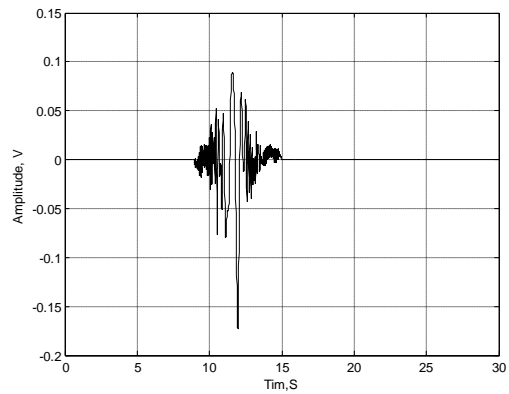


Table 9.2 Speed estimation for Pritchatts Pritchattspark 434MHz

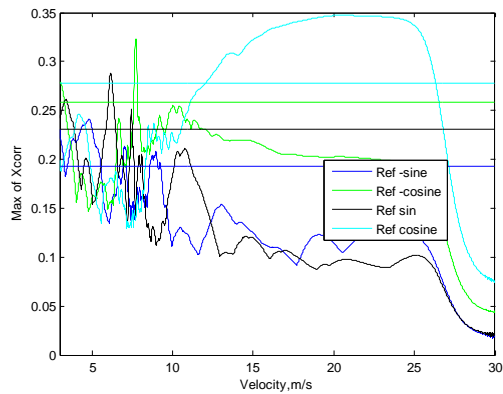
File	Real speed	Max of slope(V)	Max of XCORR(V)	Slope+XCORR(V)
4LT_1.bin	5.355556	5.85m/s	4.7	4.7
4LT_2.bin	4.490404	3.9	3.9	3.9
4LT_3.bin	4.952733	5.39	5.39	5.39
4LT_4.bin	4.32986	4.61	3.7	3.7
4LT_5.bin	4.084746	3.61	3.61	3.61
4LT_6.bin	5.738095	6.15	4.99	4.99
4LT_7.bin	5.878049	6.28	20.51	5.25
4LT_8.bin	6.025	6.46	23.56	23.56
4LT_9.bin	6.455934	6.62	18.73	18.73
4LT_10.bin	6.287503	6.73	20.14	20.14
4LT_11.bin	7.230723	7.71	20.59	20.59
4LT_12.bin	8.122683	8.65	23.56	23.56
4LT_13.bin	8.122683	8.42	23.04	23.04
4LT_14.bin	8.122683	8.46	21.55	21.55
4LT_15.bin	7.857842	6.97	21.63	21.63
4LT_16.bin	10.95455	11.84	24.39	24.39
4LT_17.bin	10.18166	10.64	10.96	10.96
4LT_18.bin	10.78782	11.2	24.24	24.24
4LT_19.bin	10.33005	10.72	24.39	24.39
4LT_20.bin	10.47826	10.88	24.54	24.54
4LT_42.bin	7.692308	8.64	20.29	20.29
4LT_43.bin	8.310345	8.58	23.72	23.72
4LT_44.bin	8.122683	8.96	23.64	23.64
4LT_45.bin	7.945928	8.19	23.57	23.57
4LT_46.bin	9.03976	9.73	23.87	23.87
4LT_47.bin	7.157707	6.7	6.7	6.7
4LT_48.bin	8.814923	8.67	24.02	8.67
4LT_49.bin	9.153057	8.98	24.02	10.13
4LT_50.bin	8.712943	8.89	9.92	9.92
4LT_51.bin	8.310345	9.07	9.54	9.54
RMSE		7%	150%	137%



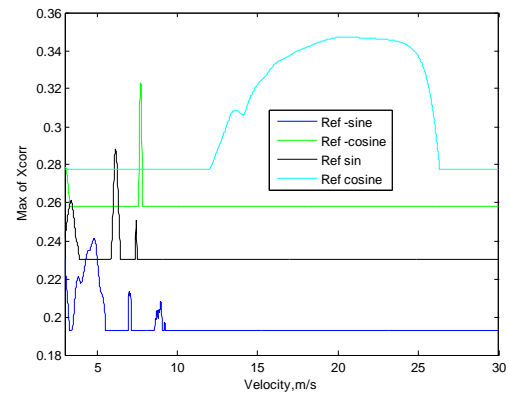
(a)



(b)

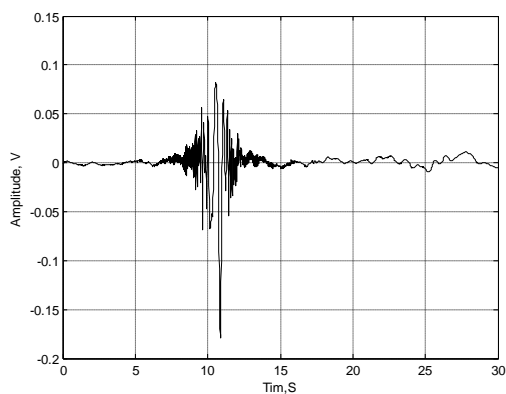


(c)

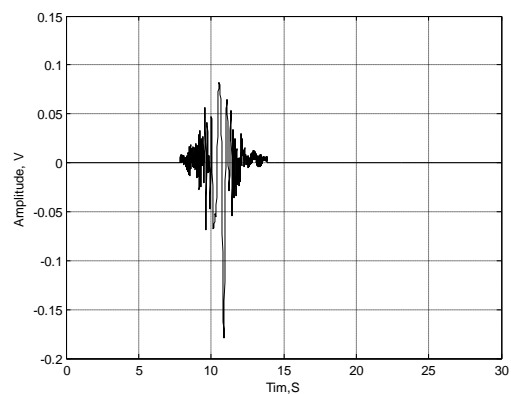


(d)

Figure 9.12 Signal processing for 11.bin 434MHz (a) Time domain signature (b) Truncated Time domain signal 11.bin 434MHz (c) Max of XCORR versus velocity (d) Max of XCORR versus velocity



(a)



(b)

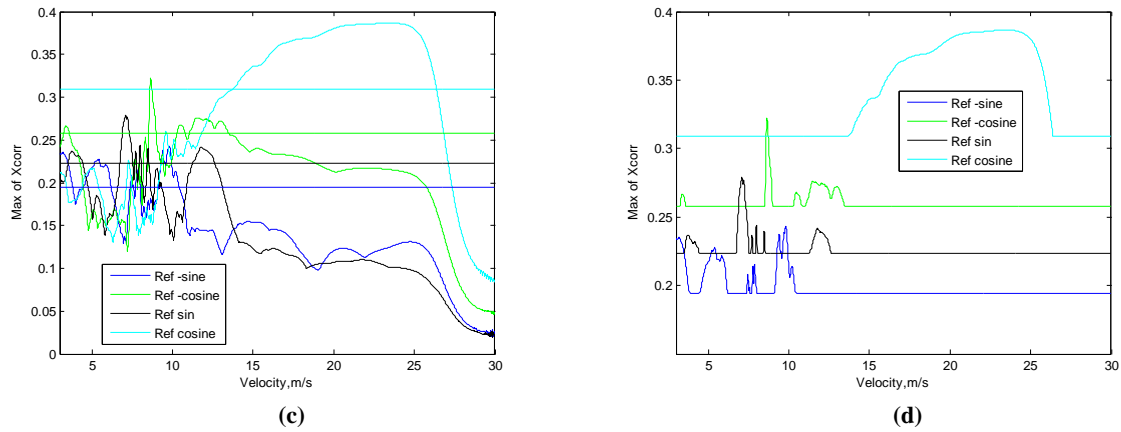


Figure 9.13 Signal processing for 12.bin (a) Time domain signature (b) Truncated Time domain signal (c)Max of XCORR versus velocity (d) Max of XCORR versus velocity

Table 9.3 Maximum of cross correlation result with the parameters factor A

A	0	0.1	0.2	0.3	0.4	0.5	0.6	0.7	0.8	0.9	1
4C_13.bin	0.29	0.29	0.29	0.28	0.27	0.26	0.29	0.34	0.37	0.39	0.41
4C_14.bin	0.34	0.33	0.33	0.32	0.30	0.28	0.30	0.33	0.35	0.36	0.36
4C_15.bin	0.28	0.28	0.27	0.27	0.26	0.28	0.30	0.32	0.36	0.38	0.40
4C_16.bin	0.28	0.28	0.27	0.26	0.25	0.25	0.26	0.28	0.30	0.31	0.31
4C_17.bin	0.28	0.28	0.28	0.27	0.28	0.29	0.29	0.30	0.31	0.32	0.34
4C_18.bin	0.32	0.32	0.31	0.29	0.27	0.27	0.28	0.31	0.33	0.35	0.37
4C_19.bin	0.23	0.22	0.22	0.21	0.21	0.23	0.26	0.27	0.29	0.29	0.30
4C_20.bin	0.27	0.27	0.27	0.26	0.26	0.25	0.26	0.28	0.29	0.30	0.31
4C_21.bin	0.23	0.24	0.25	0.25	0.26	0.26	0.26	0.27	0.28	0.30	0.31
4C_22.bin	0.24	0.24	0.24	0.24	0.23	0.23	0.24	0.25	0.26	0.27	0.28
4C_23.bin	0.24	0.24	0.25	0.25	0.26	0.26	0.25	0.25	0.24	0.26	0.26
4C_24.bin	0.24	0.24	0.24	0.24	0.23	0.23	0.23	0.24	0.26	0.27	0.27
4C_25.bin	0.17	0.17	0.18	0.18	0.19	0.19	0.19	0.19	0.19	0.19	0.20
4C_26.bin	0.14	0.15	0.15	0.16	0.17	0.17	0.17	0.16	0.16	0.16	0.17

Table 9.4 Speed estimation result with the parameters factor A

A	0	0.1	0.2	0.3	0.4	0.5	0.6	0.7	0.8	0.9	1
4C_13.bin	9.01	9.02	9.04	9.05	4.39	4.39	8.47	8.48	8.49	8.48	8.49
4C_14.bin	8.73	8.73	8.74	8.76	8.77	8.79	7.82	7.83	7.85	7.85	8.09
4C_15.bin	4.75	4.75	4.76	4.77	4.58	8.67	8.68	8.51	8.51	8.52	8.52
4C_16.bin	9.02	9.03	9.02	9.03	9.03	4.09	7.42	7.51	7.79	7.81	7.89
4C_17.bin	4.34	8.8	8.8	8.66	8.66	8.67	8.68	7.32	7.52	7.87	7.88
4C_18.bin	9.29	9.3	9.31	9.32	9.33	7.79	8.19	8.55	8.79	8.8	8.81
4C_19.bin	7.13	7.14	7.14	6.69	11.68	11.69	12.14	12.59	12.6	12.99	13.8

Chapter 9 Appendix

4C_20.bin	14.4	14.41	14.38	14.29	14.31	14.29	11.86	12.13	12.59	12.6	12.88
4C_21.bin	6.85	13.56	13.57	13.58	13.59	13.59	11.62	11.63	12.39	12.53	12.53
4C_22.bin	14.13	14.11	14.12	14.04	14.06	14.04	11.69	11.68	12.39	12.67	12.68
4C_23.bin	3.1	3.1	3.64	3.73	3.95	3.96	29.99	29.95	18.57	18.58	18.58
4C_24.bin	19.31	19.32	19.28	19.29	19.23	19.09	15.46	15.47	16.63	16.64	16.76
4C_25.bin	5.62	3.24	3.32	3.33	3.34	3.38	3.39	3.4	3.41	18.57	18.58
4C_26.bin	4.85	4.86	3.01	3.01	3.01	3.03	3.04	3.05	3.24	17.08	17.09

Table 9.5 Maximum of cross correlation result with the parameters factor B

B	0	0.1	0.2	0.3	0.4	0.5	0.6	0.7	0.8	0.9	1
4C_13.bin	0.26	0.26	0.27	0.29	0.30	0.31	0.31	0.32	0.32	0.32	0.32
4C_14.bin	0.26	0.25	0.25	0.26	0.27	0.28	0.29	0.30	0.30	0.31	0.31
4C_15.bin	0.26	0.26	0.27	0.28	0.29	0.30	0.31	0.31	0.31	0.31	0.31
4C_16.bin	0.25	0.26	0.27	0.28	0.29	0.29	0.30	0.30	0.30	0.29	0.29
4C_17.bin	0.27	0.26	0.27	0.29	0.30	0.31	0.32	0.32	0.33	0.33	0.33
4C_18.bin	0.24	0.24	0.24	0.25	0.26	0.27	0.27	0.28	0.28	0.29	0.29
4C_19.bin	0.23	0.23	0.24	0.25	0.26	0.27	0.28	0.28	0.29	0.29	0.29
4C_20.bin	0.21	0.21	0.22	0.23	0.24	0.25	0.26	0.26	0.27	0.27	0.27
4C_21.bin	0.22	0.23	0.25	0.26	0.27	0.28	0.29	0.29	0.29	0.30	0.30
4C_22.bin	0.20	0.20	0.21	0.22	0.23	0.24	0.25	0.25	0.25	0.24	0.24
4C_23.bin	0.23	0.24	0.25	0.26	0.26	0.27	0.27	0.26	0.26	0.25	0.25
4C_24.bin	0.20	0.21	0.21	0.22	0.23	0.24	0.25	0.26	0.26	0.26	0.26
4C_25.bin	0.17	0.17	0.18	0.19	0.20	0.20	0.19	0.19	0.19	0.19	0.19
4C_26.bin	0.14	0.14	0.14	0.14	0.15	0.15	0.16	0.16	0.16	0.15	0.15

Table 9.6 Speed estimation result with the parameters factor B

B	0	0.1	0.2	0.3	0.4	0.5	0.6	0.7	0.8	0.9	1
4C_13.bin	3.98	5.36	5.36	5.36	5.36	5.36	5.31	5.3	5.29	5.29	5.02
4C_14.bin	5.05	5.04	5.54	5.54	5.57	5.6	5.45	5.33	5.34	5.18	5.19
4C_15.bin	3.95	3.96	5.6	5.61	5.46	5.48	5.49	5.5	5.51	5.21	5.21
4C_16.bin	4.75	3.01	3.01	3.01	3.02	3.03	3.04	3.05	3.05	3.06	3.07
4C_17.bin	8.93	5.31	5.19	5.06	5.07	5.08	5.09	5.11	4.95	4.81	4.82
4C_18.bin	4.07	4.07	4.07	5.97	5.97	5.98	5.88	5.88	5.45	5.44	5.44
4C_19.bin	3.01	8.83	8.76	8.77	8.41	8.42	8.42	8.13	8.14	8.07	8.07
4C_20.bin	5.85	5.87	3.63	3.63	3.01	7.93	7.94	8.31	8.31	7.85	7.83
4C_21.bin	8.04	8.05	8.06	8.07	8.08	7.91	7.92	7.93	7.78	7.78	7.79
4C_22.bin	13.59	3.04	3.09	3.1	3.11	3.25	3.26	3.28	3.3	3.32	3.06
4C_23.bin	3.01	3.01	3.01	3.01	3.03	3.05	3.07	3.09	3.11	3.12	3.14
4C_24.bin	3.21	3.22	3.23	3.69	3.71	3.38	3.03	3.05	3.06	3.07	3.08

Chapter 9Appendix

4C_25.bin	3.6	3.31	3.31	3.32	3.32	3.33	3.33	3.69	3.68	3.68	3.07
4C_26.bin	3.53	3.54	4.45	4.45	4.46	4.47	4.49	4.5	4.51	4.51	3.22

Appendix DSample Matlab code

‘SpeedEsti.m’ will load and estimate the raw data and save the speed file into mat format.

```
%% Matlab version 7.11.10 (R2010b)
%% File name: SpeedEsti.m
%% Purpose: to estimate velocity of the target automatically
%% Created by: Chunyang Xu
close all;
clear all;
clc;
% call signal from 09_03_19_Tilesford airfield 4C channel
Dir_trial='f:\RadarPROVATC\xuchunyang11_7_2011PCA_SOLO\10_10_02_Pritchatt_CarPark\Landro
ver_Position1_speed1\';
filelist=dir([Dir_trial '*.bin']); % assign data to this file
freq='64';%64 135 173 434MHz
velocity_fileName=[velocityEst_' freq 'Om_Xcoeff_' date '.mat'];
velocityEst_FNmat = [Dir_trial velocity_fileName]; % .mat file directory to save estimated speed
% Parameters selection
frequency=str2num(freq);
Channel=0;% 0- RSSI Channel
% 1- Doppler Channel
Nfreq=4;% Number of frequencys device
% Nfreq=3;% Number of frequencys device
baseline=50; % baseline length in pritchatt park is 50metres
TargetLength=0; % dot is 0, landrover length is 4.8 width is 2.89
vlight =2.9979e+008;% velocity of light
sRate=100; % sampling rate , Hz
CrossPoint=0;% 0 means the mid point of Baseline
angleVector =[pi/2]; % The angle of target pass the baseline;
%% Velocity set up
minV =3; %Expected minimum absolute velocity of target in meter/second
maxV =30;%Expected maximum absolute velocity of target in meter/second
```


Chapter 9Appendix

```
dAV =0.01; %%Step in absolute velocity between target signatures
Velocity_range=[minV:dAV:maxV];
%% Create vectors of velocity components Vx and Vy determined by crossing angle of target
nAV = length(Velocity_range); %%Number of absolute velocities
nAngles = length(angleVector); %%Number of inputted angles
TotV = nAV*nAngles; %%Length of vectors to store Vx and Vy
xVel = zeros(1,TotV); %%Create vector to store Vx
yVel = zeros(1,TotV); %%Create vector to store Vy
if angleVector==pi/2;
    xVel=zeros(1,TotV);
    yVel=Velocity_range;
else
%%Start count of indicies of vectors for Vx and Vy
    count=1;
for iVel = 1:nAV %%Loop over absolute velocity
    absVel = minV + (iVel-1)*dAV; %%Calculate absolute velocity for this
iteration
for iAngle = 1:nAngles %%Loop over trajectory angles
    xVel(count) = 0; %%xVel is zero when the angele is 90 degree
    yVel(count) = absVel*sin(angleVector(iAngle)); %%Calculate Vy
    count = count + 1; %%Find a way to reduce this to not counting one
over
end
end
end
%% Filter design
% hardware filter in the device
f_LPF=20-0.1; %% LPF cut off frequency 19.9Hz
[z1, p1, k1] = butter(5,f_LPF*2/sRate,'low'); %% Hardware LPF of 5th order - filter coefficients
[SOS1, gain1] = zp2sos(z1, p1, k1); %% Convert coefficients to SOS form
lpf = dfilt.df2tsos(SOS1, gain1); %% Create filter object
f_HPF=0.2; %% HPF cut off frequency 0.2Hz
[z, p, k] = butter(1,f_HPF*2/sRate,'high'); %% Hardware HPF of 1 order - filter coefficients
[SOS, gain] = zp2sos(z, p, k); %% Convert coefficients to SOS form
hpf = dfilt.df2tsos(SOS, gain); %% Create filter object
%*****
dT = 1/sRate; %% Time step
tMulti=0; %% threshold multiplier (10.3)
winAv=1;
nFiles = size(filelista,1); %% Number of files
```

Chapter 9 Appendix

```
for n_file=1:nFiles ;
    handle_waitbar= waitbar(n_file/nFiles,'Progress...');
%test signal
    fileName = [Dir_trial filelista(n_file).name];
fileNameShort = fileName(max(findstr(fileName,'_')+1:end));
    [data] = readTargetSignalBin(fileName,2*Nfreq);
switch frequency
case 64;
    signal= data(1+Channel,:); %to choose RSSI Channel frequency: 64Mhz - 1,
    detect_range=500;
case 135;
    signal= data(3+Channel,:); %135Mhz-3,Omni directional
    detect_range=400;
case 173;
    signal= data(5+Channel,:); %173Mhz-5,Omni directional
    detect_range=400;
case 434;
    signal= data(7+Channel,:); %434Mhz-7,Directional
    detect_range=300;
end
%Normalize the amplitude of signal to get the test_signal which need to be estimated
    test_signal=signal-mean(signal);
    HPF_LPF_test_signal=filter(hpf,filter(lpf,test_signal));
    [max_abs_test, ind_max_abs_test]=max(abs(HPF_LPF_test_signal));
    detect_test_signal=[zeros(1,ind_max_abs_test-detect_range)
HPF_LPF_test_signal( ind_max_abs_test-detect_range: ind_max_abs_test+detect_range)
zeros(1,3000-ind_max_abs_test-detect_range-1)];
% reference signal generation
    nSamples=length(test_signal);
    time = dT*(1:nSamples); %Time at which sample will occur
    factor = time - nSamples/(2*sRate);
    %% Cross Correlations procedure, Loop over from reference functions
    color_set1={'B-';'G-';'k-';'C-'};
    max_peak_val=0;
    threshold_Mcor=0.9;% set up the threshold ratio
for n_ref=1:4%reference function index from 1 to 4
for iXYVel = 1:TotV %Loop over velocity pairs Vx and Vy
%Calculate position of target as it moves on it trajectory,for a given transit time and sample rate.
    xPos = CrossPoint + xVel(iXYVel)*factor; %Calculate x position
    yPos = yVel(iXYVel)*factor; %Calculate Y position
```

Chapter 9 Appendix

```
txRange =sqrt((xPos + baseline/2).^2 + yPos.^2);%Calculate range of target from Tx
rxRange =sqrt((xPos - baseline/2).^2 + yPos.^2);%Calculate range of target from Rx
refSig =cos((2*pi*frequency*10^6/vlight*(txRange+rxRange+TargetLength)-
baseline)+(pi/2)*n_ref);
refSig1=gausswin(nSamples,2)'.*refSig;
fRefSig(:,iXYVel,n_ref) = filter(hpf,filter(lpf, refSig1)); %Filter the signature - LPF then HPF
% corA_temp = xcorr(fRefSig(:,iXYVel,n_ref), detect_test_signal,'coeff');
corA_temp = smooth(xcorr(fRefSig(:,iXYVel,n_ref), detect_test_signal,'coeff'),10);
Max_cor(n_ref,iXYVel)=max(corA_temp);
end
[max_V(n_ref),ind_max_V(n_ref)]=max(Max_cor(n_ref,:));
Max_cor_tem=Max_cor(n_ref,:);
Max_cor_tem(Max_cor_tem<threshold_Mcor*max_V(n_ref))=threshold_Mcor*max_V(n_ref);
Max_cor_temp(n_ref,:)=Max_cor_tem;
threshold_line1(n_ref,:)=ones(1,length(Max_cor_tem))*0.9*max_V(n_ref);
threshold_line2(n_ref,:)=ones(1,length(Max_cor_tem))*0.8*max_V(n_ref);
threshold_line3(n_ref,:)=ones(1,length(Max_cor_tem))*0.7*max_V(n_ref);
end
const_range=25;% Define the leatest constant range value
peak_inds=zeros(1,100);
section_C=zeros(4,100);
color_set={'BO';'G*';'k+';'c.'};
color_Winset={'Bs';'Gs';'ks';'cs'};
for step_ref=1:4
%Identify different sections for peak slope calculation
none_threshold_Max_cor_temp=find(Max_cor_temp(step_ref,:)==threshold_Mcor*max_V(step_ref));
diff_none_threshold_Max_cor_temp=diff(none_threshold_Max_cor_temp);
none1_diff_none_threshold_Max_cor_temp=find((diff_none_threshold_Max_cor_temp)~=1);
if length(none1_diff_none_threshold_Max_cor_temp)==0
section_C(step_ref,1:2)=none_threshold_Max_cor_temp([1,end]);
else
section_A=none_threshold_Max_cor_temp([1,none1_diff_none_threshold_Max_cor_temp+1,end]);
section_B=diff_none_threshold_Max_cor_temp(none1_diff_none_threshold_Max_cor_temp);
section_B=section_A(2:length(section_B)+1)-section_B;
section_C(step_ref,1:length(section_A)+length(section_B))=add_arr(section_A,section_B);
end
none0_sectionC=find(section_C(step_ref,:)==0);
section_num(step_ref)=length(none0_sectionC)/2;
Wincounter=0;
```

Chapter 9 Appendix

```
for step_section=1:section_num(step_ref)
    peak_section=section_C(step_ref,2*(step_section-1)+1:2*(step_section-1)+2);
[peak_section_value(step_ref,step_section),peak_section_ind_temp(step_ref,step_section)]=max(Max_cor(step_ref,peak_section(1):peak_section(2)));
peak_section_ind(step_ref,step_section)=peak_section_ind_temp(step_ref,step_section)+peak_section(1)-1;
[upward_slope,downward_slope]=slope_cal_v1(Max_cor(step_ref,:),peak_section_value(step_ref,step_section),peak_section_ind(step_ref,step_section),const_range);
    max_slope_vector(step_ref,step_section)=max(abs(upward_slope),abs(downward_slope))*sRate;
end
    [max_ref_slope_val(step_ref),max_ref_slope_ind(step_ref)]=max(max_slope_vector(step_ref,:));
    [max_ref_xcorr(step_ref),max_ref_xcorr_ind(step_ref)]=max(peak_section_value(step_ref,:));
    peakValue_ref(step_ref)=peak_section_value(step_ref,max_ref_slope_ind(step_ref));
end

%-----%
% velocity estimation using slope critira
    [max_refslopeval,max_refslopeval_ind]=max(max_ref_slope_val);
    velocityEst(n_file).maxslope_val=max_refslopeval;%max slope value
    velocityEst(n_file).maxslope_ref=max_refslopeval_ind;%max slope reference index

velocityEst(n_file).maxslope_vel=peak_section_ind(max_refslopeval_ind,max_ref_slope_ind(max_ref_slopeval_ind))*dAV+minV;
%-----%

% velocity estimation using xcorr critira
    [max_xcorr_val,max_xcorr_ind]=max(max_V);
    velocityEst(n_file).max_xcorr_val=max_xcorr_val;%max xcorr value
    velocityEst(n_file).max_xcorr_ref=max_xcorr_ind;%max xcorr reference index
    velocityEst(n_file).max_xcorr_vel=ind_max_V(max_xcorr_ind)*dAV+minV;% velocity estimation
using max of xcorr

%-----%

%velocity estimation using max of xcorr of the sharpest slope
    [max_refXcorrslopeval,max_refXcorrslopeval_ind]=max(peakValue_ref);
    velocityEst(n_file).maxXcorrslope_val=max_refXcorrslopeval;% val=value
    velocityEst(n_file).maxXcorrslope_ref=max_refXcorrslopeval_ind;% ind=index
```

Chapter 9 Appendix

```
velocityEst(n_file).maxXcorr_slope_vel=peak_section_ind(max_refXcorr_slope_val_ind,max_ref_slope_in  
d(max_refXcorr_slope_val_ind))*dAV+minV;
```

```
%-----%
```

```
velocityEst(n_file).fileName=filelista(n_file).name;  
str_n_file=num2str(n_file+1);  
content_range=['A' str_n_file ':'G' str_n_file ];  
content_string=[{filelista(n_file).name} velocityEst(n_file).maxslope_vel  
velocityEst(n_file).max_xcorr_vel...  
velocityEst(n_file).maxXcorr_slope_vel ...  
max_refslope_val_ind max_xcorr_ind max_refXcorr_slope_val_ind ];  
xlswrite('X:\RadarPRO\ATC\temp.xls',content_string,content_range);
```

```
end
```

```
close(handle_waitbar);  
eval(['save ' velocityEst_FNmat ' velocityEst']);  
msgbox('FINISH');
```

'SpeedNorm.m' will normalize the time domain signals to the same speed and plot out the PSD signatures in the frequency domain

```
%% Matlab version 7.11.10 (R2010b)
```

```
%% File name: SpeedNorm.m
```

```
%% Purpose: To normalize the target speed automatically
```

```
%% Created by: Chunyang Xu
```

```
close all;
```

```
clear all;
```

```
clc;
```

```
Dir_trial='x:\RadarPRO\ATC\xuchunyang11_7_2011PCA_SOLO\10_10_02_Pritchatt_CarPark\Landro  
ver_Position3\';
```

```
filelista=dir([Dir_trial '* .bin']); % assign data to this file
```

```
freq='434';%64 135 173 434MHz
```

```
velocity_fileName=['velocityEst_' freq 'Om_Xcoeff_' date '.mat'];
```

```
velocityEst_FNmat = [Dir_trial velocity_fileName]; % .mat file directory to save estimated speed
```

```
% Parameters selection
```

```
frequency=str2num(freq);
```

Chapter 9 Appendix

```
Channel=0;% 0- RSSI Channel
% 1- Doppler Channel
Nfreq=4;% Number of frequencys device
% Nfreq=3;% Number of frequencys device
baseline=50; % baseline length in pritchatt park is 50metres
TargetLength=0; % dot is 0, landrover length is 4.8 width is 2.89
vlight =2.9979e+008;% velocity of light
sRate=100; % sampling rate , Hz
CrossPoint=0;% 0 means the mid point of Baseline
angleVector =[pi/2]; % The angle of target pass the baseline;

% *****
%% Velocity set up
minV =3; %Expected minimum absolute velocity of target in meter/second
maxV =30;%Expected maximum absolute velocity of target in meter/second
dAV =0.01; %Step in absolute velocity between target signatures
Velocity_range=[minV:dAV:maxV];
%% Create vectors of velocity components Vx and Vy determined by crossing angle of target
nAV = length(Velocity_range); %Number of absolute velocities
nAngles = length(angleVector); %Number of inputted angles
TotV = nAV*nAngles; %Length of vectors to store Vx and Vy
xVel = zeros(1,TotV); %Create vector to store Vx
yVel = zeros(1,TotV); %Create vector to store Vy
if angleVector==pi/2;
    xVel=zeros(1,TotV);
    yVel=Velocity_range;
else
%Start count of indicies of vectors for Vx and Vy
    count=1;
for iVel = 1:nAV %Loop over absolute velocity
    absVel = minV + (iVel-1)*dAV; %Calculate absolute velocity for this
iteration
for iAngle = 1:nAngles %Loop over trajectory angles
    xVel(count) = 0; %xVel is zero when the angele is 90 degree
    yVel(count) = absVel*sin(angleVector(iAngle)); %Calculate Vy
    count = count + 1; %Find a way to reduce this to not counting one
over
end
end
end
```

Chapter 9 Appendix

```
% *****

%% Filter design
% *****

% hardware filter in the device
f_LPF=20*0.1;          % LPF cut off frequency 19.9Hz
[z1, p1, k1] = butter(5,f_LPF*2/sRate,'low');% Hardware LPF of 5th order - filter coefficients
[SOS1, gain1] = zp2sos(z1, p1, k1);    % Convert coefficients to SOS form
lpf = dfilt.df2tsos(SOS1, gain1);      % Create filter object
f_HPF=0.2;             % HPF cut off frequency 0.2Hz
[z, p, k] = butter(1,f_HPF*2/sRate,'high'); % Hardware HPF of 1 order - filter coefficients
[SOS, gain] = zp2sos(z, p, k);        % Convert coefficients to SOS form
hpf = dfilt.df2tsos(SOS, gain);       % Create filter object

% *****

dT = 1/sRate;          % Time step
tMulti=0; % threshold multiplier (10.3)
winAv=1;
nFiles = size(filelista,1);% Number of files
% for n_file=1:nFiles ;
for n_file=1:1;
% %test signal
    fileName = [Dir_trial filelista(n_file).name];
    fileNameShort = fileName(max(findstr(fileName,'_')+1:end));
    [data] = readTargetSignalBin(fileName,2*Nfreq);
switch frequency
case 64;
    signal= data(1+Channel,:); %to choose RSSI Channel frequency: 64Mhz - 1,
    detect_range=500;
case 135;
    signal= data(3+Channel,:); %135Mhz-3,Omni directional
    detect_range=400;
case 173;
    signal= data(5+Channel,:); %173Mhz-5,Omni directional
    detect_range=400;
case 434;
    signal= data(7+Channel,:); %434Mhz-7,Directional
    detect_range=300;
end
%Normalize the amplitude of signal to get the test_signal which need to be estimated
```

Chapter 9 Appendix

```
test_signal=signal-mean(signal);
HPF_LPF_test_signal=filter(hpf,filter(lpf,test_signal));
[max_abs_test, ind_max_abs_test]=max(abs(HPF_LPF_test_signal));
detect_test_signal=[zeros(1,ind_max_abs_test-detect_range)
HPF_LPF_test_signal( ind_max_abs_test-detect_range: ind_max_abs_test+detect_range)
zeros(1,3000-ind_max_abs_test-detect_range-1)];
%*****
% reference signal generation
nSamples=length(test_signal);
time = dT*(1:nSamples); %Time at which sample will occur
Sample_frequency=sRate;
nfft_ref=4096;
Targetsignal=HPF_LPF_test_signal;
s1=fft(Targetsignal,nfft_ref);
s2=conj(fft(Targetsignal,nfft_ref));
PSD_s = s1.*s2/nfft_ref; %% power spectral density
normalised_PSD_s1=10*log10(abs(PSD_s)/max(PSD_s));
figure();
plot([0:Sample_frequency/length(normalised_PSD_s1):Sample_frequency-
Sample_frequency/length(normalised_PSD_s1)],normalised_PSD_s1,'r');
hold on;
Targetsignal=detect_test_signal;
s1=fft(Targetsignal,nfft_ref);
s2=conj(fft(Targetsignal,nfft_ref));
PSD_s = s1.*s2/nfft_ref; %% power spectral density
normalised_PSD_s1=10*log10(abs(PSD_s)/max(PSD_s));
plot([0:Sample_frequency/length(normalised_PSD_s1):Sample_frequency-
Sample_frequency/length(normalised_PSD_s1)],normalised_PSD_s1,'k');
hold on;
Targetsignal= [zeros(1,ind_max_abs_test-600) HPF_LPF_test_signal( ind_max_abs_test-600:
ind_max_abs_test+600) zeros(1,3000-ind_max_abs_test-601)];;
s1=fft(Targetsignal,nfft_ref);
s2=conj(fft(Targetsignal,nfft_ref));
PSD_s = s1.*s2/nfft_ref; %% power spectral density
normalised_PSD_s1=10*log10(abs(PSD_s)/max(PSD_s));
plot([0:Sample_frequency/length(normalised_PSD_s1):Sample_frequency-
Sample_frequency/length(normalised_PSD_s1)],normalised_PSD_s1,'b');
detect_range_text=['Target signal in ' num2str(detect_range*2/sRate) 's'];
legend('Signal in 30s',detect_range_text,'Target signal in 12s');
factor = time - nSamples/(2*sRate);
```


Chapter 9 Appendix

```
%% Cross Correlations procedure, Loop over from reference functions
color_set1={'B-';'G-';'k-';'C-'};
max_peak_val=0;
threshold_Mcor=0.8;% set up the threshold ratio
for n_ref=1:4%reference function index from 1 to 4
for iXYVel = 1:TotV %Loop over velocity pairs Vx and Vy
%Calculate position of target as it moves on it trajectory,for a given transit time and sample rate.
    xPos = CrossPoint + xVel(iXYVel)*factor; %Calculate x position
    yPos = yVel(iXYVel)*factor; %Calculate Y position
    txRange =sqrt((xPos + baseline/2).^2 + yPos.^2);%Calculate range of target from Tx
    rxRange =sqrt((xPos - baseline/2).^2 + yPos.^2);%Calculate range of target from Rx
    refSig =cos((2*pi*frequency*10^6/vlight*(txRange+rxRange+TargetLength)-
baseline)+(pi/2)*n_ref);
    refSig1=gausswin(nSamples,2)'.*refSig;
    fRefSig(:,iXYVel,n_ref) = filter(hpf,filter(lpf, refSig1)); %Filter the signature - LPF then HPF
    corA_temp = xcorr(fRefSig(:,iXYVel,n_ref), detect_test_signal,'coeff');
    Max_cor(n_ref,iXYVel)=max(corA_temp);
end
    [max_V(n_ref),ind_max_V(n_ref)]=max(Max_cor(n_ref,:));
    Max_cor_tem=Max_cor(n_ref,:);
    Max_cor_tem(Max_cor_tem<threshold_Mcor*max_V(n_ref))=threshold_Mcor*max_V(n_ref);
    Max_cor_temp(n_ref,:)=Max_cor_tem;
    threshold_line(n_ref,:)=ones(1,length(Max_cor_tem))*threshold_Mcor*max_V(n_ref);
end
    figure();
for plot_step=1:4
    plot(Velocity_range,Max_cor_temp(plot_step,:),color_set1{plot_step});
    hold on;
end
    xlim([minV maxV]);
    xlabel('Velocity,m/s');
    ylabel('Max of Xcorr');
    legend('Ref -sine','Ref -cosine','Ref sin','Ref cosine');
    title(fileNameShort );
    figure();
for plot_step=1:4
    plot(Velocity_range,Max_cor(plot_step,:),color_set1{plot_step});
    hold on;
end
for plot_step=1:4
```

Chapter 9 Appendix

```
plot(Velocity_range,threshold_line(plot_step,:),color_set1{plot_step});
hold on;
end
% Multipeak detection process
const_range=25;% Define the leatest constant range value
peak_inde=zeros(1,100);
section_C=zeros(4,100);
upward_slope_vector=zeros(4,100);
RMSE_Winvector=zeros(4,100);
color_set={'BO';'G*';'k+';'c.'};
for step_ref=1:4
%Identify different sections for peak slope calculation
none_threshold_Max_cor_temp=find(Max_cor_temp(step_ref,:)==threshold_Mcor*max_V(step_ref));
diff_none_threshold_Max_cor_temp=diff(none_threshold_Max_cor_temp);
none1_diff_none_threshold_Max_cor_temp=find((diff_none_threshold_Max_cor_temp)~=1);
if length(none1_diff_none_threshold_Max_cor_temp)==0
section_C(step_ref,1:2)=none_threshold_Max_cor_temp([1,end]);
else
section_A=none_threshold_Max_cor_temp([1,none1_diff_none_threshold_Max_cor_temp+1,end]);
section_B=diff_none_threshold_Max_cor_temp(none1_diff_none_threshold_Max_cor_temp);
section_B=section_A(2:length(section_B)+1)-section_B;
section_C(step_ref,1:length(section_A)+length(section_B))=add_array(section_A,section_B);
end
none0_sectionC=find(section_C(step_ref,:)==0);
section_num(step_ref)=length(none0_sectionC)/2;
Wincounter=0;
for step_section=1:section_num(step_ref)
peak_section=section_C(step_ref,2*(step_section-1)+1:2*(step_section-1)+2);

[peak_section_value(step_ref,step_section),peak_section_ind_temp(step_ref,step_section)]=max(Max_cor(step_ref,peak_section(1):peak_section(2)));

peak_section_ind(step_ref,step_section)=peak_section_ind_temp(step_ref,step_section)+peak_section(1)-1;

[upward_slope,downward_slope]=slope_cal_v1(Max_cor(step_ref,:),peak_section_value(step_ref,step_section),peak_section_ind(step_ref,step_section),const_range);

max_slope_vector(step_ref,step_section)=max(abs(upward_slope),abs(downward_slope))*sRate;
end
```

Chapter 9Appendix

```
[max_ref_slope_val(step_ref),max_ref_slope_ind(step_ref)]=max(max_slope_vector(step_ref,:));  
[max_ref_xcorr(step_ref),max_ref_xcorr_ind(step_ref)]=max(peak_section_value(step_ref,:));  
peakValue_ref(step_ref)=peak_section_value(step_ref,max_ref_slope_ind(step_ref));
```

end

```
%-----%
```

```
% velocity estimation using slope critira
```

```
[max_refslopeval,max_refslopeval_ind]=max(max_ref_slope_val);  
velocityEst(n_file).maxslope_val=max_refslopeval;%max slope value  
velocityEst(n_file).maxslope_ref=max_refslopeval_ind;%max slope reference index
```

```
velocityEst(n_file).maxslope_vel=peak_section_ind(max_refslopeval_ind,max_ref_slope_ind(max_ref  
slopeval_ind))*dAV+minV;
```

```
%-----%
```

```
% velocity estimation using xcorr critira
```

```
[max_xcorr_val,max_xcorr_ind]=max(max_V);  
velocityEst(n_file).max_xcorr_val=max_xcorr_val;%max xcorr value  
velocityEst(n_file).max_xcorr_ref=max_xcorr_ind;%max xcorr reference index  
velocityEst(n_file).max_xcorr_vel=ind_max_V(max_xcorr_ind)*dAV+minV;% velocity estimation
```

```
using max of xcorr
```

```
%-----%
```

```
%velocity estimation using max of xcorr of the sharpest slope
```

```
[max_refXcorrslopeval,max_refXcorrslopeval_ind]=max(peakValue_ref);  
velocityEst(n_file).maxXcorrslope_val=max_refXcorrslopeval;% val=value  
velocityEst(n_file).maxXcorrslope_ref=max_refXcorrslopeval_ind;% ind=index
```

```
velocityEst(n_file).maxXcorrslope_vel=peak_section_ind(max_refXcorrslopeval_ind,max_ref_slope_in  
d(max_refXcorrslopeval_ind))*dAV+minV;
```

```
%-----%
```

```
velocityEst(n_file).fileName=filelista(n_file).name;  
str_n_file=num2str(n_file+1);  
content_range=['A' str_n_file ':'G' str_n_file ];  
content_string=[{filelista(n_file).name} velocityEst(n_file).maxslope_vel  
velocityEst(n_file).max_xcorr_vel...  
velocityEst(n_file).maxXcorrslope_vel ...  
max_refslopeval_ind max_xcorr_ind max_refXcorrslopeval_ind ];
```

Chapter 9 Appendix

```
xlswrite('X:\RadarPRO\ATC\temp.xls',content_string,content_range);  
  
end  
% eval(['save ' velocityEst_FNmat ' velocityEst']);  
msgbox('FINISH');
```

Appendix E Publications

1. Xu Chunyang, "Latest velocity estimation and normalization result of the ground forward scatter radar system," *Radar Conference 2013, IET International* , vol., no., pp.1,4, 14-16 April 2013